2007

Design And Demonstration Of Meanderline Retarders At Infrared Frequencies

Jeffrey Scott Tharp
University of Central Florida

STARS Citation

Tharp, Jeffrey Scott, "Design And Demonstration Of Meanderline Retarders At Infrared Frequencies" (2007). *Electronic Theses and Dissertations, 2004-2019*. 3381.
https://stars.library.ucf.edu/etd/3381

DESIGN AND DEMONSTRATION OF MEANDERLINE RETARDERS AT INFRARED FREQUENCIES

by

JEFFREY SCOTT THARP
B.S. University of North Carolina at Asheville, 2002
M.S. University of North Carolina at Charlotte, 2004

A dissertation submitted in partial fulfillment of the requirements
for the degree of Doctor of Philosophy
in the College of Optics and Photonics: CREOL & FPCE
at the University of Central Florida
Orlando, Florida

Fall Term
2007

Major Professor: Glenn D. Boreman

ABSTRACT

Meanderline structures are widely used as engineered birefringent materials for waveplates and retarders at radiofrequencies, and have been previously demonstrated at frequencies up to 90 GHz in the millimeter-wave band. In this dissertation, we present results related to the modeling, fabrication, and experimental characterization of meanderlines across the range from 30 to 100 THz, in the long-wave and mid-wave infrared bands. Specific issues addressed in these new designs include spectral dispersion and angular dependence of the retardance, as well as axial ratio and throughput. The impact resulting from the infrared properties of the metals and dielectrics is explicitly included throughout. Several novel applications are identified, including integrated circular polarizers, reflective waveplates, and large-area polarization tags.

ACKNOWLEDGMENTS

I would like to acknowledge my advisor, Dr. Glenn Boreman, for his patience and guidance throughout my time here at UCF. His leadership style enabled me to accomplish this work in a fashion that has allowed me to grow both personally and professionally.

I would like to acknowledge DRS Optronics and Alan Rakes for the funding of this project.

I would like to acknowledge James, Dave, Pete, and the other IR group members for the everyday brainstorming sessions that helped progress the research to its present state. With this interaction, many obstacles were overcome and questions answered.

I would like to acknowledge Dr. Javier Alda of the University Complutense of Madrid. With his extensive knowledge and experience in the field of optics, I was challenged and pushed academically. Because of his never-ending enthusiasm and optimism, I made a good friend.

I would like to acknowledge Guy Zummo for his technical expertise in maintaining the lab equipment, and for his insight to experimental design. I would like to thank Dr. Ivan Divliansky for technical assistance and training with the Leica EBPG system.

I would like to acknowledge Dr. Ben Munk of The Ohio State University for taking his time to visit the lab and conversing with me to better help my understanding of frequency-selective surfaces.

My biggest acknowledgment goes to my beautiful wife, Christine, who has walked with me in this academic journey since my first months in college. Her love, perseverance, and encouragement has never wavered.

TABLE OF CONTENTS

LIST OF FIGURES

LIST OF ACRONYMS

AC	alternating current
AR	axial ratio
CP	circular polarizer
CVD	chemical vapor deposition
DC	direct current
EBL	electron-beam lithography
EBPG	Electron-Beam Pattern Generator
FOV	field-of-view
FSS	frequency selective surface
FTIR	Fourier-transform infrared
HFSS	high-frequency simulation software
IPA	isopropyl alcohol
IR	infrared
IR-VASE	IR variable-angle spectroscopic ellipsometry
LWIR	long-wavelength infrared
MWIR	mid-wavelength infrared
PEC	perfect electric conductor
PECVD	plasma enhanced chemical vapor deposition
PMM	periodic method of moments
PMMA	poly(methyl methacrylate)

PVD	physical vapor deposition
RF	radio frequency
RLC	resistor-inductor-capacitor
SEM	scanning-electron microscope or micrograph

CHAPTER I
INTRODUCTION

1.1 Motivation for Research

The motivation for the infrared (IR) meanderline retarder is to show that the retarding functionality that exists at radio frequencies (RF) [1-3] for this type of structure can also function in the infrared, extending present capabilities. The goals are to demonstrate an understanding of the physics involved with the interaction of an electromagnetic wave with the meanderline structure. Along with the physics, a model will be presented, based on previous works [4] that attempts to simplify the interpretation to an equivalent circuit model. Using these interpretations and an understanding of the variation of performance resulting from changing the free variables of geometry and material properties, models will be developed and run in a commercially available simulation software package, Ohio State's Periodic Method of Moments. With the modeling, designs are developed to have the meanderline function as a quarter-wave retarder for the mid-wave IR (MWIR) and the long-wave IR (LWIR). To accompany the modeled predictions, each of the various designs were fabricated and characterized to correlate the modeled and measured performance.

The meanderline retarders are expected to have advantages compared to current birefringent crystals and Fresnel rhombs [5]. Some of the advantages are ease of fabrication and flexibility in the band of operation via changing the geometrical parameters lithographically. The lithographic methods of fabrication lead to easy variations in the designs. Also, the meanderline retarder is expected to have a spectral dispersion of performance comparable to a true single-order crystal retarder. The single-order quarter-wave plate shows the best performance with respect to spectral dispersion of phase delay in commercially available retarders. The angular performance is also expected to be excellent in comparison to current retarding technologies [4]. In addition, the meanderline retarder is a planar device which will fit well into optical systems.

1.2 Polarization of Light

Light has four fundamental properties: frequency, intensity, coherence, and, polarization. The concept on which this work is centered is the polarization of the light. The polarization of light arises from its constituent components, the time-varying electric and magnetic fields. Light is frequently treated as a transverse electromagnetic wave that satisfies Maxwell's equations and therefore the wave equation.

The polarization of light is defined by the electric field vector in the plane that contains both **E**, the electric field vector, and **k**, the propagation vector. If the plane remains stationary as the wave propagates, the polarization is defined as linearly polarized. However, if another linearly polarized wave is propagating in the same region with its **E** field oriented perpendicular to the first, the polarization will depend upon the phase difference between the two electric fields. The electric fields can be mathematically represented as: [6]

$$\begin{aligned} \vec{E}_x(z,t) &= \vec{x}E_{0x}\cos(kz-\omega t+\delta) \\ \vec{E}_y(z,t) &= \vec{y}E_{0y}\cos(kz-\omega t) \end{aligned} \qquad \text{Equation 1}$$

The total optical field would be the vector sum

$$\vec{E}_{tot}(z,t) = \vec{x}E_{ox}\cos(kz - \omega t + \delta) + \vec{y}E_{oy}\cos(kz - \omega t) \qquad \text{Equation 2}$$

If the difference in phase between the two components is an even multiple of π radians then the two fields sum to a linearly polarized wave with an orientation angle determined by the magnitudes of the orthogonal amplitudes. When the phase difference is an odd multiple of π radians the wave will also be linearly polarized, but the plane of polarization is rotated to an angle equal to twice the angle of the initial orientation relative to the fast axis. If the phase difference is ± π/2 and the amplitudes are equal, a special state of polarization exists, circular polarization. Circular polarization differs from linear polarization in two special ways, the plane that contains **E** and **k** rotates by 2π radians for each wavelength of propagation in z and the orthogonal amplitudes are always equal in magnitude. This rotation has two possible states, left and right circular polarization pending the sign of the $\pi/2$ phase difference. The convention for defining the left and right circular polarization is that if the **E** field rotates clockwise, as observed from the receiver, it is defined as right circular polarization and if it rotates counter-clockwise it is left circular polarization. [6, 7]

Both linear polarization and circular polarization are limiting cases of the more general case of elliptical polarization. Elliptical polarization occurs when, using Equation 2, E_{0x}, E_{0y}, and δ are free variables that do not satisfy the conditions defined by linear or circular polarization. The general nature is that the **E** field varies in magnitude as it rotates rather than staying constant as for circular polarization. The mathematics of elliptical geometry is well covered in the literature

[6-8] and only the necessary relations for representing the present research will be shown. The polarization ellipse is shown in Figure 1.

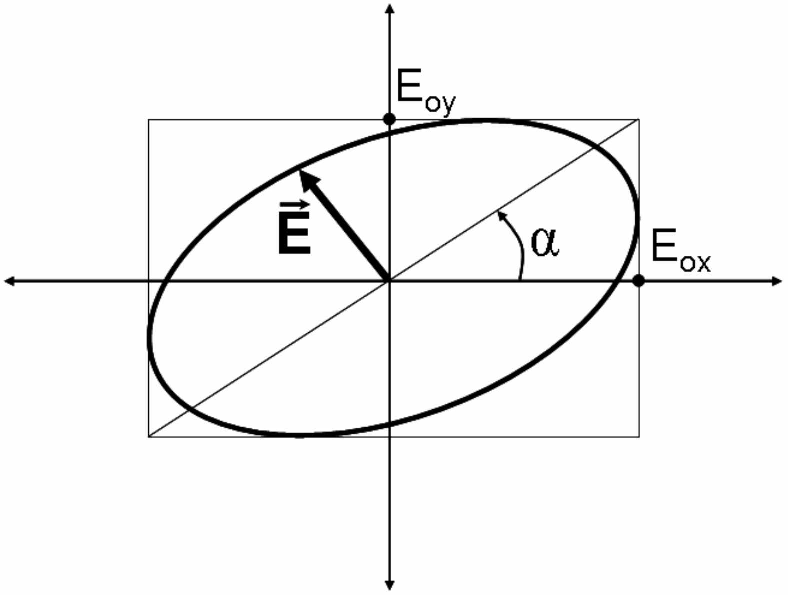

Figure 1 Polarization ellipse showing the sweep of the E field in one optical cycle

The parameters of interest are the maximum amplitudes for both orthogonal states, E_{0x} and E_{0y}, and the auxiliary angle, α. The auxiliary angle is the angle of a diagonal line that crosses a rectangle circumscribing the ellipse. It is mathematically defined in terms of the maximum field amplitudes: [6]

$$\tan\alpha = \frac{E_{0y}}{E_{0x}} \qquad \delta = \delta_x - \delta_y \qquad \text{Equation 3}$$

Using the auxiliary angle and the phase difference as defined in Equation 3 another property of the polarization ellipse can be defined. This parameter is the ratio of the major axis to the minor axis of the polarization ellipse and is defined as the axial ratio (AR) of the polarization ellipse. The AR is defined as [6]

$$AR = \frac{1}{\tan\left[\frac{1}{2}\sin^{-1}\left\{\sin(2\alpha)\sin(\delta)\right\}\right]} \qquad \text{Equation 4}$$

The AR ranges from a value of 1 corresponding to circular polarization to a value of infinity, corresponding to linear polarization.

1.3 Current Methods of Polarization Modification

1.3.1 Linear Polarizers

The ability to modify the polarization of light is the next aspect of interest. The simplest method to modify the polarization of randomly polarized light is to use a linear polarizer. The linear polarizer is a dichroic polarizer. A dichroic polarizer shows preferential absorption of a particular state of polarization, allowing the remaining light to be transmitted. The dichroic linear polarizers used for the infrared tend to be wiregrids [9] on a transparent substrate. The component of the light that lies along the absorption axis (parallel to the wires) is absorbed by the metal wires, and due to the long path of the wire, currents are induced. Energy is lost thermally through resistive heating causing the light transmitted in the forward direction to be linearly polarized perpendicular to the wire direction. [7]

1.3.2 Crystal Retarders

To make circular polarization, it is necessary to induce a temporal phase difference between the two orthogonal linear states. As light propagates in a material its velocity is determined by the material's refractive index. In free space light travels at 2.998×10^8 meters per second, however in matter the velocity is reduced by the refractive index of the material to

$$v = \frac{c}{n} \qquad \text{Equation 5}$$

The velocity of the light in matter, v, represented in Equation 5, is shown with c being the speed of light in a vacuum and n is the refractive index of the material. The aspect of this expression that is of value to producing circular polarization is that in some materials the refractive index depends upon the orientation of the linear polarization of the incident light. These materials are called birefringent materials and the primary source of these special materials are crystals that, due to their lattice geometry and component compounds, exhibit birefringence [7, 8]. This birefringence essentially means that their optical properties are not the same in all directions, and as such can be very useful for changing polarization [6].

Birefringent crystals are used as optical retarding elements in many optical systems due to their relatively small size as compared to other technologies such as Fresnel rhombs. As retarders, one linear polarization component will travel faster through the crystal than the other orthogonal component. After exiting the crystal, the light will propagate with a phase difference between the linear polarization states that depends upon several characteristics of the crystal. The important parameters include the thickness of the crystal and the difference between the refractive indices for the respective polarization components. The phase delay induced is

$$\delta = k(n_s - n_f)d \qquad \text{Equation 6}$$

The retardance, δ in radians, is shown in Equation 6 where k is the wavenumber of the incident radiation, n_s and n_f are the slow refractive index and fast refractive index, respectively, of the crystal, and d is the physical thickness of the crystal. Equation 6 assumes the light is perpendicular to the optical axis of the crystal as shown in Figure 2.

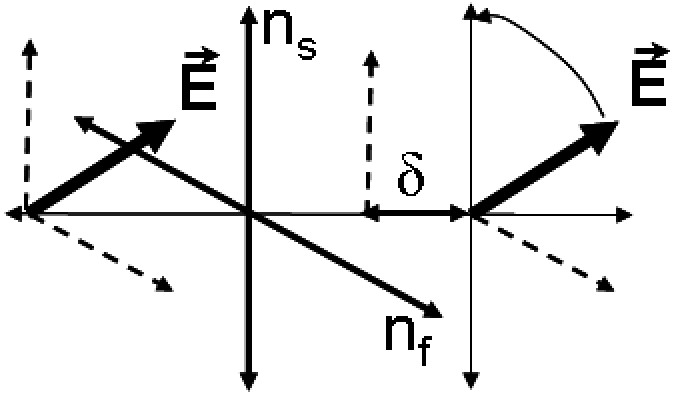

Figure 2 Effect of birefringence on incident linear polarized field

Also as shown in Figure 2, the electric field vector will rotate when a phase difference exists between the two orthogonal components of the incident linear polarized field. Since the slow axis has the larger refractive index, the electric field will sweep in a direction that is toward the slow axis upon initial propagation within the crystal. To create circular polarization, the incident linearly polarized field is oriented at an angle of 45° with respect to the slow axis, and the thickness is chosen so that the retardation is $\pi/2$ radians. The handedness of the circular polarization can be modified by merely having the linear polarized light oriented to ±45° with respect to the slow axis. Right circularly polarized light will emerge if, in the setup shown in Figure 2, the entering linear polarization is oriented at 45° with respect to the slow axis (left circularly polarized light if at -45°), assuming that the length of the crystal corresponds to a phase delay of $\pi/2$ radians [6-8].

Birefringent crystal retarders work very well to apply a desired phase delay, however there exist some constraints in the manufacture the retarders. In a birefringent crystal, the phase differential can be $\pi/2$ plus any even multiple of π, for a given handedness of circular polarization. However some adverse effects occur for phase delays greater that $\pi/2$. Therefore crystal retarders are classified into three catagories [7]: true-zero order, compound-zero-order, and multiple-order retarders. True-zero-order retarders have a thickness that corresponds to exactly $\pi/2$ phase delay at a given wavelength, therefore they are very thin and difficult to fabricate. As an example, a quarter-wave retarder made of quartz will need to be ~15 μm thick to achieve a zero-order retardance at a wavelength of 550 nm. A compound-zero-order retarder will have two identical crystals back to back with their fast axes rotated 90° from each other. This is to induce a large delay in the first crystal, and then to switch the axes to reverse the phase delay until the desired zero order delay is achieved. A multiple-order retarder is fabricated to be a length larger than the minimum length, to simplify fabrication process.

True zero-order retarders have the best performance of the three different kinds of birefringent crystals. The performance issues of concern are wavelength dependence and angular dependence of the phase delay. The spectral dependence of crystal retarders is determined simply by taking the derivative of Equation 6 with respect to the wavelength [10]. The spectral dispersion of the phase delay for a true-zero-order retarder and a multiple-order retarder is given in Equation 7.

$$\frac{\partial \delta}{\partial \lambda} = \delta \left(\frac{1}{(n_s - n_f)} \frac{\partial (n_s - n_f)}{\partial \lambda} - \frac{1}{\lambda} \right) \qquad \text{Equation 7}$$

The spectral dispersion is observed in Equation 7 to be proportional to the total retardance of the crystal. Therefore, multiple-order retarders will exhibit very high deviations in retardance with respect to wavelength compared to a single-order retarder. It is also observed in Equation 7 that the best spectral phase delay that is possible using birefringent crystals has a $1/\lambda$ dependence even for a true-single-order retarder. The spectral dependence is also seen to be dependent on the material dispersion of the crystal itself; however this contribution is much less than the explicit phase delay and $1/\lambda$ dependence [10]. The spectral dispersion of the phase delay for a compound-single-order retarder is given in Equation 8 in terms of the phase delay induced by the first crystal, δ_1, and the phase delay added back by the second crystal, δ_2.

$$\frac{\partial \delta}{\partial \lambda} = (\delta_1 - \delta_2)\left(\frac{1}{(n_s - n_f)} \frac{\partial (n_s - n_f)}{\partial \lambda} - \frac{1}{\lambda} \right) \qquad \text{Equation 8}$$

For compound-zero-order retarders made of the same crystal, the spectral dispersion of the phase delay can be minimized if tight tolerances are used for the two crystal thicknesses, so that the difference in the phase delays, $\delta_1 - \delta_2$, will be the equivalent to the retardance of a true-single-order retarder.

The angular performance of a birefringent crystal is a little more complicated. As the incident propagation direction deviates from being perpendicular to the optic axis, the effective indices of each component will vary as a function of the angle, changing the retardance of a crystal of given length. The other angular performance constraint is more obvious and it is a result of the effective lengthening of the propagation distance in the crystal as the incidence angle is increased. This lengthening is proportional to the secant of the incidence angle. [11]

Examples of crystal quarter-wave retarder performance are shown in Figure 3 [10] in terms of variation in retardance in units of waves. The top figure shows the change in retardance as a function of the percent of center wavelength for both a single-order retarder and a multiple-order retarder. An AR = 1.6 at the short wavelength end and an AR = 1.2 at the long wavelength end is observed for a zero-order retarder. The multi-order retarder of the top figure shows very large variations in retardance as the wavelength is varied by even small increments. The bottom figure shows the variance of the retardance as a function of angle of incidence, for polarization parallel and perpendicular to the optic axis, for the three types of crystal retarders. It is observed that the compound-zero-order and multiple-order retarders show large sensitivity to the incidence angle. At an angle of 8° and 11°, the AR was increased to 1.3 for the compound-zero-order and multi-order retarder, respectively. These high angular sensitivities are seen because of the generally large thicknesses of these types of retarders, which cause even small angles of deviation to correspond to large differences in optical path length. The zero-order retarder will be limited primarily by the effective distance of propagation in the crystal, and for example will have an AR = 2.0 at an incidence angle of 45°. However, after 45° the performance will degrade severely and the AR quickly approaches infinity (linear polarization) at an incidence angle of 60°. This is because the optical path length in the crystal at 60° has doubled compared to the on-axis case – therefore the crystal is acting as a half-wave plate for an incidence angle of 60°. For a more detailed discussion of the spectral and angular effects on the retardance in a birefringent crystal, the reader is referred to [10, 11].

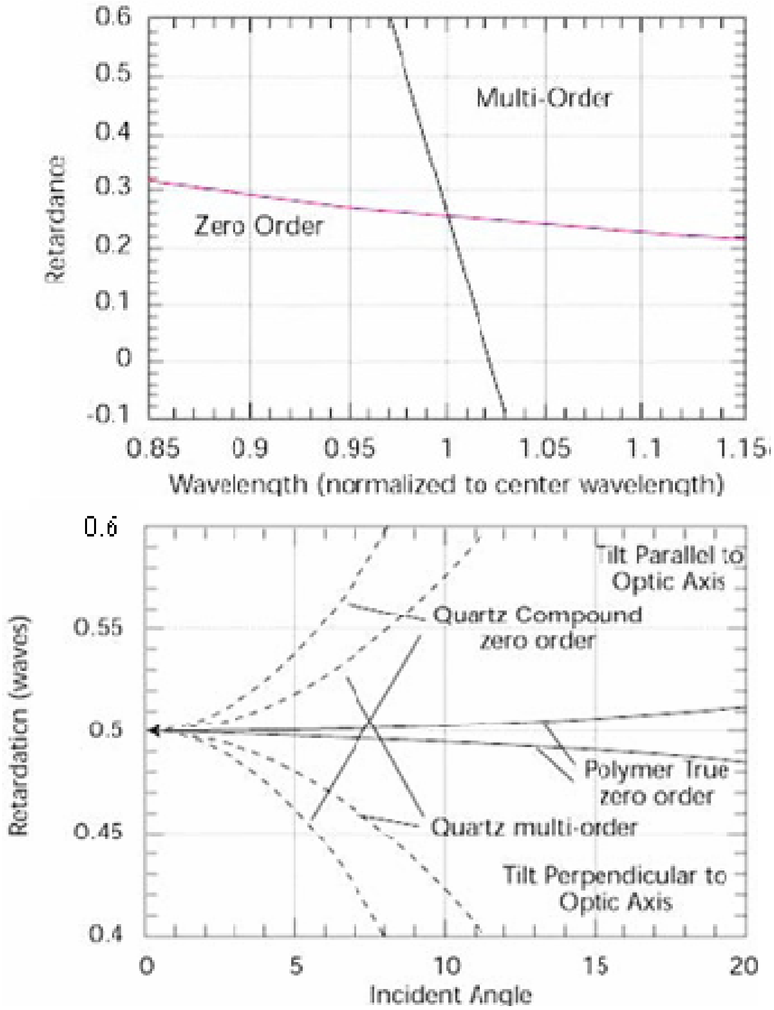

Figure 3 Plots representing typical variations in the retardance as a function of wavelength (top) and incidence angle (bottom) for each of the three types of birefringent crystal retarders [10]. Note in the top, the true-zero order and compound-zero order retarders have the same spectral performance as was shown in Equation 7.

1.4 Meanderline Introduction

The meanderline retarder first appears in the literature in 1973, for a frequency range of 8 – 12 GHz [1]. The meanderline, an example of which is shown in Figure 4, was qualitatively described as an equivalent circuit with each polarization experiencing a different electrical environment at the meanderline boundary. Meanderline wave plates have been traditionally used in the radio frequency (RF) portion of the spectrum to convert linearly polarized radiation into circularly polarized radiation [1-4, 12]. Before the present investigations, the highest frequency range previously found in the literature is 60 – 90 GHz [3]. The meanderline structure acts as a phase retarder for the two orthogonal wave components that are polarized along and perpendicular to the meander axis, shown in Figure 5. The meanderline acts primarily as an inductive element along the meander axis and as a capacitive element perpendicular to the meander axis, creating the relative phase delay for the orthogonal polarization components [1]. Use of electron-beam lithography has made fabrication of such structures feasible at much higher frequencies, up into the infrared (IR) portion of the spectrum. The ease of fabrication, low fabrication costs, and compact construction may provide a potentially important alternative to birefringent crystals in the IR. An especially attractive characteristic of meanderline waveplates is the ability to define designs for specific frequencies and phase delays by simple changes in the lithography. This flexibility offers a benefit as compared to birefringent crystals. This is because the wavelength of operation for a birefringent crystal quarter-wave plate is determined by the thickness of a given material and its optical properties [7, 8, 13]. The current wavelength bands common for commercial crystal retarders are from visible to ~2.1 μm, although they can be found at 10.6 μm using ZnSe. In the range of our interest (3 – 5 μm and 8 – 12 μm) there are few other alternatives, as it is difficult to find materials in this range that have both birefringence and transparency. In the THz, there are essentially no alternatives as yet, since birefringent material characterization in the THz spectral region is much less developed compared to the long-wave IR (LWIR) and visible. Therefore, meanderlines could be of utility across the IR and THz range, since they are broadband and the center wavelength can be tuned simply by changing the geometry. Good performance is expected in the areas of spectral and angular bandwidth as well [1, 4, 14], compared to traditional birefringent crystal waveplates.

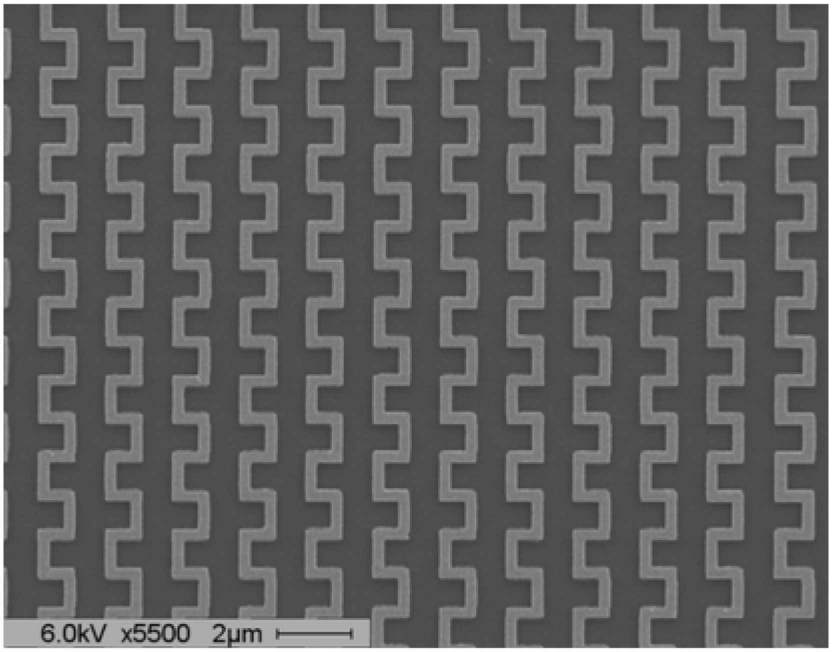

Figure 4 Meanderline structure

1.4.1 Equivalent Circuit Model

As an electromagnetic wave propagates in a medium or transmission line it experiences an impedance to its propagation that is given by the characteristic impedance of the medium. The characteristic impedance is [15]

$$Z = \sqrt{\frac{\mu_0 \mu_r}{\varepsilon_0 \varepsilon_r}} \qquad \text{Equation 9}$$

The characteristic impedance is the ratio of the electric field amplitude to the magnetic field amplitude in the material in which the wave is propagating. This quantity is important to the description of light when it interacts with a boundary between different materials. To satisfy the wave equation and the electromagnetic boundary conditions, there are three possible solutions for waves at an interface: incident, transmitted, and reflected. The ratio of the impedances determines the distribution of power at the interface.

When a meanderline is fabricated onto a substrate, the impedance between the propagating medium and the substrate will change [1, 4, 16]. This change will take place because the radiation is incident upon the meanderline at the boundary, and the oscillating electric field will induce current oscillations along the conductive paths of the meanderline. These induced currents will change the electrical environment at the boundary and thus the meanderline will change the impedance mismatch. The decomposition of the field onto the meanderline is shown in Figure 5. The electric field is decomposed into the component along the meander axis, E_v, and the component orthogonal to it, E_h. To obtain initial design insight, an equivalent circuit model can be used.

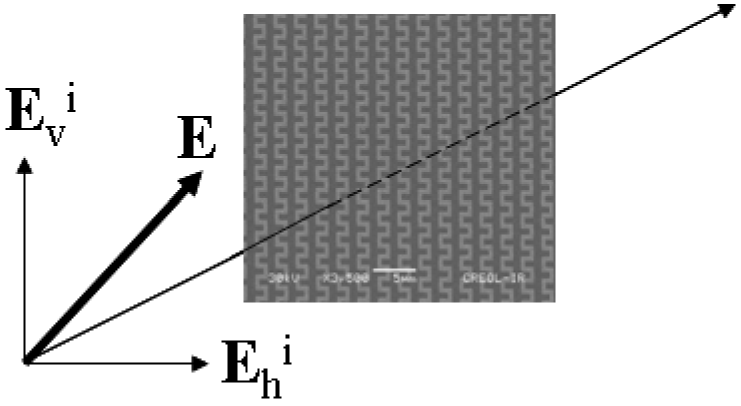

Figure 5 Diagram showing the incident E field decomposed onto the meanderline with the meanderline axis lying along E_v^i.

The meanderline behaves like a separate *RLC* circuit to each component of the driving field. The impedance of an *RLC* circuit is represented in Equation 10 with *R*, the resistive term, and *X*, the reactive term.

$$Z = R + iX \qquad \text{Equation 10}$$

The impedance contribution due to an inductive reactance is

$$\mathrm{X}_L = i\omega L \qquad \text{Equation 11}$$

The impedance contribution due to a capacitive reactance is

$$\mathrm{X}_C = \frac{1}{i\omega C} = \frac{-i}{\omega C} \qquad \text{Equation 12}$$

Since the current flow along the meanderline axis is continuous, the effective *RLC* circuit for radiation polarized along the meander axis is inductively dominated [1, 4]. The component perpendicular to the meanderline axis experiences an effective *RLC* circuit that is capacitively dominated [1, 4]. Since the component along the meanderline axis is inductively dominated, the transmitted field will have an induced phase advance while the orthogonal component will have an induced phase delay as per Equation 11 and Equation 12. The schematic for the equivalent circuit model is shown in Figure 6 for a single layer meanderline in free space [1, 4]. The equivalent schematic also represents the resistive nature of the metals at IR frequencies as series resistors.

For a single meanderline immersed in a given medium, the transmission coefficients will be complex since the impedance of the meanderline structure is also complex for each component. The impedance mismatch between the meanderline and the surrounding medium determines the reflected and transmitted field quantities [17]. The reflected field due to an impedance mismatch is represented as:

$$\Gamma = \frac{Z_L - Z_0}{Z_L + Z_0} = |\Gamma| e^{i\theta_r} \qquad \tau = 1 + \Gamma \qquad \text{Equation 13}$$

The complex reflection and transmission coefficients, Γ and τ, are determined as shown in Equation 13, in terms of the characteristic impedance of the medium, Z_0, and the equivalent load impedance of the meanderline, Z_L. Dividing by the characteristic impedance, Z_0, the reflection coefficient is represented using a normalized load impedance. All values that have been normalized to the characteristic impedance of the medium will be written as lower case variables [17].

$$z_L = \frac{Z_L}{Z_0} = r_L + ix_L \qquad \Gamma = \frac{z_L - 1}{z_L + 1} \qquad \text{Equation 14}$$

Using this circuit analogue, it is seen that each polarization will experience different impedances due to the meanderline structure, and that each will be transmitted with different phases and amplitudes. If the impedances are tuned correctly, the desired difference in the phase between the two transmitted field components can be obtained for the purpose of polarization modification.

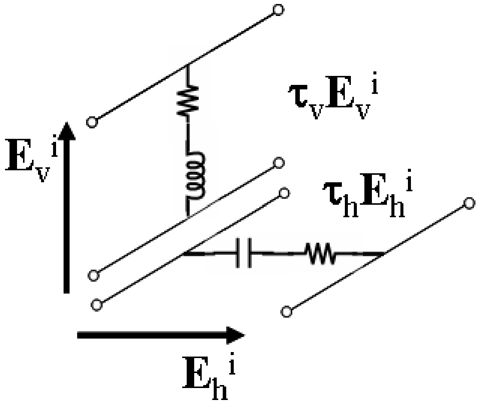

Figure 6 Equivalent circuit model for describing the meanderline retarder in free space.

When there exist multiple layers (of different wave impedance) with finite spacing between them, the field amplitudes can be functions of position [17], because in each medium the incident and the reflected waves will superimpose and their resultant sum will be a standing wave in each layer. Thus the impedance will be a function of the impedance mismatch, the separation distance between the layers, and the measurement point. This is known as the transmission line input impedance at any given location in the structure, and is given in Equation 15 [17].

$$z_{in} = \frac{z_L + i\tan(\beta l)}{1 + iz_L \tan(\beta l)} \qquad \text{Equation 15}$$

Equation 15 for the input impedance, z_{in}, is given in terms of the normalized load impedance, z_L, the effective wavenumber, β, and the transmission line length, *l*. The development of the equivalent circuit model is shown in Figure 7 for the field component perpendicular to the meanderline axis. The development for the orthogonal field component is similar. In Figure 7 A) two connected transmission lines are represented schematically, which can represent a dielectric boundary for a propagating optical wave. The reflection and transmission for this case can be determined using Equation 13. In Figure 7 B), a capacitor and resistor in series with each other represent the impedance, Z_m, of the meanderline at the boundary of the dielectric. Under the assumption that waves reflected from the back of the substrate can be neglected (*l* goes to infinity) and that the substrate is lossles, we can model the situation as shown in Figure 7 C). In Figure 7 C), the impedance of the substrate is in parallel to that of the meanderline.

Since the resulting circuit model represents the meanderline impedance in parallel with the impedance of the substrate, it is more convenient to represent the reflection and transmission coefficients in terms of admittance rather than impedance, since two admittances in parallel with one another in a circuit will add in series. Admittance is defined as the inverse of impedance or

$$Y = \frac{1}{Z} \qquad \text{Equation 16}$$

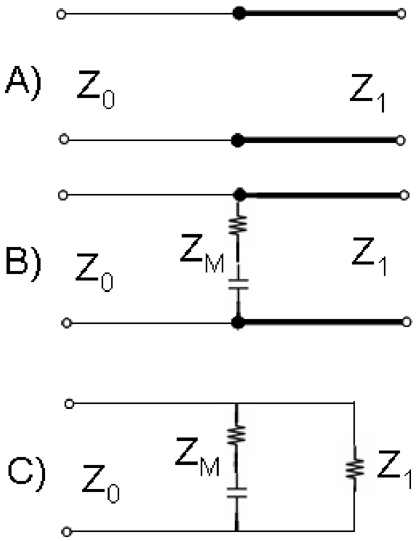

Figure 7 Schematic development of the meanderline equivalent circuit model

To find the admittance expression for this field component, the impedance must first be defined as a lossy capacitive component. This impedance of the meanderline is defined in Equation 17 in terms of the meanderline loss, R_m, and the reactive meanderline impedance, X_m.

$$Z_m = R_m + i\mathrm{X}_m \qquad \text{Equation 17}$$

The dielectric substrate is assumed to be lossless, and with impedance Z_2. The equivalent admittance of the circuit representing the meanderline on the substrate is given in Equation 18.

$$Y_{tot} = \frac{1}{Z_{tot}} = \frac{1}{Z_2} + \frac{1}{R_m + i\mathrm{X}_m} = \left(\frac{1}{Z_2} + \frac{R_m}{{R_m}^2 + {\mathrm{X}_m}^2}\right) - i\left(\frac{\mathrm{X}_m}{{R_m}^2 + {\mathrm{X}_m}^2}\right) \qquad \text{Equation 18}$$

The maximum transmission efficiency of a single-layer meanderline designed to transmit circularly polarized radiation will now be derived. The determination of the maximum ideal transmission is the desired goal, and approximations will be made to represent an ideal meanderline retarder structure. An additional assumption is that there is no loss term in the meanderline impedance, $R_m = 0$. Thus, the real part of the admittance represents the admittance of the dielectric medium, and the imaginary part represents the reactive contribution of the meanderline retarder.

The admittance in Equation 18 can be normalized to the characteristic admittance of the incident medium, Y_0, to simplify the future calculation of the transmission and reflection coefficients. The normalized admittance, y_L, is

$$y_L = \frac{Y_{tot}}{Y_0} = \chi - i\gamma$$ Equation 19

Now Equation 14 for the reflection coefficient can be modified to accommodate the normalized admittance. The reflection coefficient as a function of normalized admittance is shown in Equation 20.

$$\Gamma = \frac{1 - y_L}{1 + y_L} = \frac{1 - \chi + i\gamma}{1 + \chi - i\gamma}$$ Equation 20

Using Equation 13 and Equation 20, the reflection and transmission coefficients can be represented in polar form to gain insight into the properties of the meanderline retarder. These reflection and transmission coefficients are shown in Equation 21 and Equation 22.

$$\tau = \sqrt{\left[\frac{2(1+\chi)}{(1+\chi)^2+\gamma^2}\right]^2 + \left[\frac{2\gamma}{(1+\chi)^2+\gamma^2}\right]^2}\, e^{i\arctan\left[\frac{\gamma}{1+\chi}\right]} \qquad \text{Equation 21}$$

$$\Gamma = \sqrt{\left[\frac{1-\chi^2-\gamma^2}{(1+\chi)^2+\gamma^2}\right]^2 + \left[\frac{2\gamma}{(1+\chi)^2+\gamma^2}\right]^2}\, e^{i\arctan\left[\frac{2\gamma}{1-\chi^2-\gamma^2}\right]} \qquad \text{Equation 22}$$

To determine some properties of the meanderline retarder as a single layer structure it is necessary to apply constraints on the values of the orthogonal transmission coefficients since circular polarization is desired. For circular polarization, it is necessary that the two transmission coefficients, $|\tau_h|$ and $|\tau_v|$, have equal magnitudes and that their phase differential is 90°. Since the meanderline is lossless, χ is just the admittance of the substrate as determined from Equation 18 and Equation 19. If $|\tau_h| = |\tau_v|$, it is required from Equation 21 that $|\gamma_h| = |\gamma_v|$ since χ is equal for both components. To obtain a phase differential of 90°, it is required by Equation 21 that Equation 23 is true.

$$\left| \arctan\left[\frac{\gamma_h}{1+\chi}\right] - \arctan\left[\frac{\gamma_v}{1+\chi}\right] \right| = 90^\circ \qquad \text{Equation 23}$$

The combination of the lossless meanderline assumption, the circular polarization requirement that $|\gamma_h| = |\gamma_v|$, and the relation shown in Equation 23 requires that

$$\left|\gamma_{h,v}\right| = 1 + \chi \qquad \text{Equation 24}$$

When Equation 24 is substituted into Equation 21, it simplifies to

$$\left|\tau_{h,v}\right| = \sqrt{\frac{2}{(1+\chi)^2}} \qquad \text{Equation 25}$$

When Equation 24 is substituted into Equation 22, it simplifies to

$$\left|\Gamma_{h,v}\right| = \sqrt{\frac{(\chi-1)}{(\chi+1)} + \frac{2}{(1+\chi)^2}} \qquad \text{Equation 26}$$

Equation 25 and Equation 26 show the relationship between the magnitudes of the transmission coefficient and the reflection coefficient for a single-layer meanderline on a dielectric substrate. It is seen with the first term under the radical in Equation 26 that the dielectric mismatch of the substrate increases the reflections. To determine the maximum transmission of a single-layer meanderline retarder transmitting circularly polarized radiation, the single layer meanderline is placed either in free space alone or immersed in a material. Therefore another assumption is made that there is no dielectric boundary at the location of the meanderline structure. In this case $\chi = 1$ according to Equation 18 and Equation 19.

With $\chi = 1$, it is seen via substitution into Equation 25 and Equation 26 that the magnitudes of the transmission and reflection coefficients are equal, , $|\tau_h| = |\Gamma_h| = |\tau_v| = |\Gamma_v|$. Therefore their corresponding power coefficients are equal as well. The maximum power transmission for a single-layer-meanderline retarder operating as a quarter-wave retarder is then 50%. This can only occur for a meanderline surrounded by a single medium. When a dielectric boundary is included, the magnitude of the reflection coefficient will increase according to Equation 26, and thus the transmitted power will decrease.

Though Equations 18, 21, and 22 are valid in general terms to define the transmission and reflection coefficients, the difficult aspect of the equivalent circuit model is to quantitatively determine the impedance of the meanderline structure, Z_m. It is necessary to numerically determine the impedance of the meanderline structure.

In order to increase the transmittance of the meanderline in the desired polarization state above the 50% just seen, multiple layers are used to give a lower reflection at each layer while also applying the desired phase delays [2-4, 18]. The transformed impedances of the multiple layers will add in parallel, once the propagation distances are included. The circuit for a multilayer meanderline suspended in free space is shown in Figure 8 for the component perpendicular the meanderline axis [4].

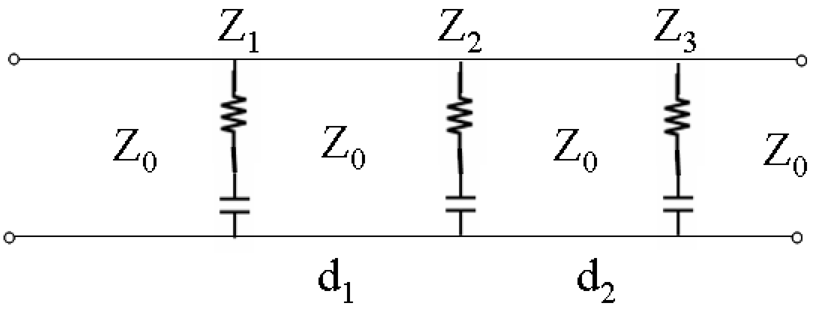

Figure 8 Equivalent impedance circuit schematic for a multilayered meanderline for the field component perpendicular to the meanderline axis.

The equivalent impedance of the circuit in Figure 8, as a function of the relevant variables, is best visualized graphically using the Smith chart [17, 19, 20].

1.4.2 Smith Chart Conceptualization

One of the classic methods of impedance matching is to incorporate the Smith chart, an example of which is shown in Figure 9 [21]. The Smith chart is used as a graphical tool for RF conjugate matching of circuits, but since the interaction of light with the meanderline retarder can be represented in an equivalent impedance circuit, the Smith chart is ideal to qualitatively introduce the conceptual functionality of the meanderline and the multilayer meanderline stacks [4].

The Smith chart is a polar plot of the complex reflection coefficient, Γ, as a function of the normalized impedance, z_L. The magnitude of the reflection coefficient, $|\Gamma|$, is plotted from the center of the chart and is bounded to $|\Gamma| \leq 1$. The phase angle of the reflection coefficient, θ, is bounded from -180° to 180° and starts at the right hand side of the chart and rotates counter-clockwise with increasing angles. The center of the chart is a special point since at this point $|\Gamma|$

= 0, and therefore there are no reflections and $Z_L/Z_0 = 1$. The aspect of the Smith chart that gives it the true utility for conjugate matching applications is that it can be used to convert a given reflection coefficient to a normalized complex load impedance and vice versa. This transformation between the reflection coefficient and normalized load impedance means that any value of resistance, r_L, and reactance, x_L, can be realized within a circle of unit radius. [17, 19, 20, 22]

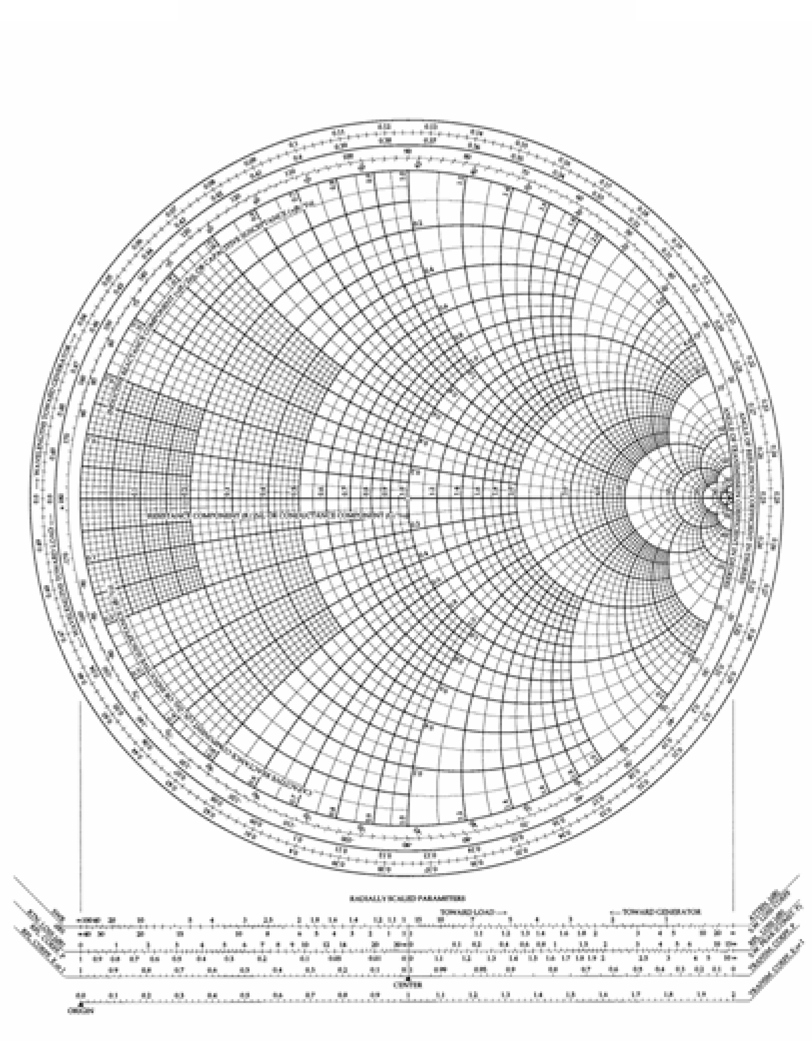

Figure 9 Example of a Smith chart showing both the impedance circles

1.4.2.1 Mathematical Foundation of Smith Chart

Upon normalizing and rearranging Equation 14 a form is found that defines the normalized impedance in terms of the complex reflection coefficient.

$$z_L = r_L + ix_L = \frac{1+\Gamma_r + i\Gamma_i}{1-\Gamma_r - i\Gamma_i} \qquad \text{Equation 27}$$

Equating the real and imaginary components of Equation 27, the real and imaginary part of the impedance, r_L and x_L respectively, become functions of the real and imaginary part of the reflection coefficient, Γ_r and Γ_i respectively. This relationship explicitly shows the transformation from reflection coefficients to impedance, and the net result is shown in Equation 28.

$$r_L = \frac{1-\Gamma_r^{\,2} - \Gamma_i^{\,2}}{(1-\Gamma_r)^2 + \Gamma_i^{\,2}} \qquad x_L = \frac{2\Gamma_i}{(1-\Gamma_r)^2 + \Gamma_i^{\,2}} \qquad \text{Equation 28}$$

From Equation 28, it is observed that the real and imaginary reflection variables, Γ_r and Γ_i, occur at most in the second order. Therefore a rearrangement can be made to put the equations in their conic form.

$$\left(\Gamma_r - \frac{r_L}{r_L+1}\right)^2 + (\Gamma_i - 0)^2 = \left(\frac{1}{r_L+1}\right)^2 \qquad \text{Equation 29}$$

$$\left(\Gamma_r - 1\right)^2 + \left(\Gamma_i - \frac{1}{x_L}\right)^2 = \left(\frac{1}{x_L}\right)^2 \qquad \text{Equation 30}$$

In Equations 29 and 30, the rearranged forms now trace circles in the complex Γ plane. The resistance traces circles of radius $1/(r_L+1)$, centered at $[r_L/(r_L+1), 0]$ as shown in Figure 10 A). It is also of note that the circle that includes the center point has a resistance that is perfectly matched to the characteristic resistance of the medium. The largest resistance circle on the Smith chart has a resistance of zero, which corresponds to an equivalent electrical short. The smallest circle corresponds to a resistance of infinity which is equivalent to an electrical open. The reactance traces circles of radius $1/x_L$, centered at $[1, 1/x_L]$. The circles whose centers lie above the line $\Gamma_i = 0$ correspond to positive reactances and are therefore inductive, while the circles that lie beneath the line correspond to negative reactances and are therefore capacitive. These are schematically shown in Figure 10 B).

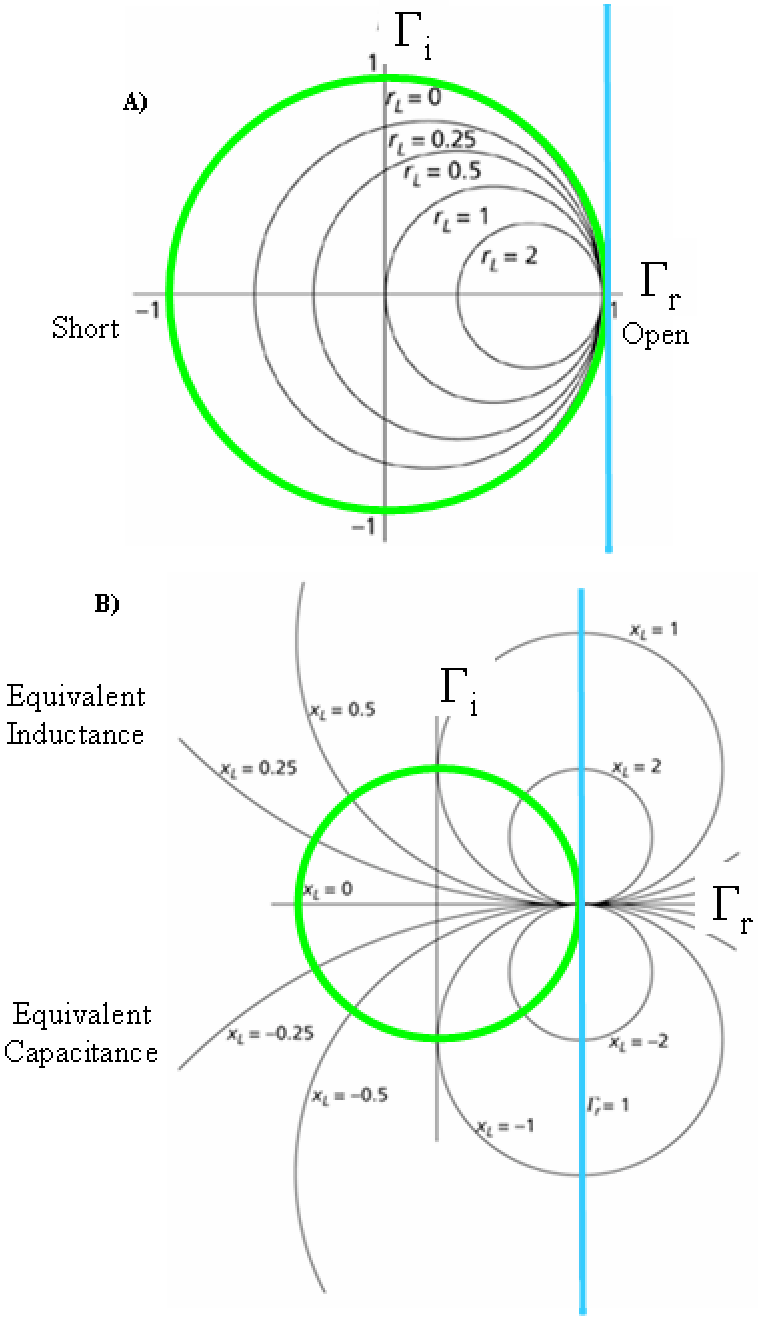

Figure 10 Diagrams showing A) the circles of resistance and B) the circles of reactance on the Smith chart

Another important aspect that is very useful for multilayered structures is that the input impedance is easily determined if the effective path length of the layer is known. This is accomplished by starting at the impedance point representing the load, and rotating clockwise around the circle with constant radius (corresponding to constant reflection magnitude). One full revolution around the circle is equal to a path length of one half the effective wavelength.

A final note concerning the use of the Smith chart for optical layers is that since the impedances of the layers add in parallel, it is generally easier to use the admittance Smith chart [4, 17, 19]. Admittance is simply the reciprocal of the impedance and is easier to use for analysis of parallel circuits, *i.e.* meanderline retarders, since the admittances will add in series. It is of note that since the impedance and admittance are inversely proportional to one another, an impedance on the Smith chart can be converted to an admittance by simply rotating the impedance point by 180° around the center of the Smith chart. After rotation, the inductive admittances lie beneath the line $\Gamma_i = 0$ while the capacitive admittances lie above the line. Also, when using the Smith chart, it is important to always work *toward* the source in a given circuit. An example would be in the case of illumination of a silicon half space from air. Using the Smith chart, the characteristic impedance, Z_0, would be the impedance of the silicon, not the impedance of air. This will be of importance when conceptualizing the design of meanderline retarders.

1.4.2.2 Smith Chart Representation of Meanderline Retarders

The circuit model that has been introduced is intended to offer insight and a starting point for designing meanderline structures. This model will allow for a conceptual approach to understanding the meanderline before going to the more complex numerical modeling methods that include the details of material properties. The Smith chart can be used as an extension to the qualitative approach to beginning a meanderline design and understanding the relationship between the meanderline impedance and polarization properties of the transmitted radiation.

To introduce the qualitative model of the functionality of the meanderline retarder, some approximations will be made. The first approximation used to simplify the circuit model is that the meanderline is composed of a perfect electrical conductor (PEC) and therefore has no ohmic loss components. The second approximation is that the dielectric layers used are in a given medium, *i.e.* there are no dielectric boundaries, only meanderlines. This approximation is to reduce the complexity by having all impedance mismatches deriving from the meanderlines alone and independent of any dielectric boundary effects. These approximations are valid for development of an initial design starting point because at the frequencies of interest, materials where chosen to optimize the metal conductivity and minimize the dielectric loss [23], and numerical methods easily calculate the dielectric boundary effects for dielectrics other than freespace. The primary dielectric boundary effect is the effective index. The effective index determines the effective wavelength at the boundary that the RF designs must be scaled to function at IR. It is represented as the geometric average of the refractive indices of the two boundaries, n_1 and n_2. The effective index is given in Equation 31 [20].

$$n_{eff} = \frac{1}{\sqrt{2}}\sqrt{n_1^{\;2} + n_2^{\;2}} \qquad \text{Equation 31}$$

All plots will be only representative of a single wavelength at normal incidence. The PEC approximation will allow the resistance of the meanderline to match the characteristic impedance of the substrate, $r_L/r_0 = 1$, while the mismatch will derive from the inductive and capacitive components of the structure [4].

The reactance of the equivalent inductance is equal to iX_v/Z_0 and the equivalent capacitance is $-iX_h/Z_0$. After plotting the reactance at the intersection of the circle of resistance equal to 1 and the circle of reactance equal to iX, the reflection coefficient is immediately known. As shown in Figure 11, both polarizations will have different complex transmittances. For a single-layer meanderline operating as a quarter-wave retarder, the desired difference in phase is 90°. In Figure 11, the magnitudes and phases of the transmitted field components are determined geometrically as $|\tau|$ and θ [4, 22]. The difference between θ_v and θ_h is the relative phase delay of the transmitted field. Therefore it is observed that to have circular polarization for a PEC single-layer meanderline, we need to obtain $\theta_v = 45°$ and $\theta_h = -45°$. With these phase values the transmission amplitudes are equal, therefore the reflected fields have the same amplitude as the transmitted fields. The transmission of a single layer meanderline retarder immersed in a medium will have a maximum transmission of 50% [4]. This is the same result as was derived earlier using the transmission line equations. This ideal transmission is also rarely achieved because of the loss in the metal and the dielectric reflection losses at the substrate interfaces that increase the impedance mismatch beyond the effect of the meanderline retarder itself.

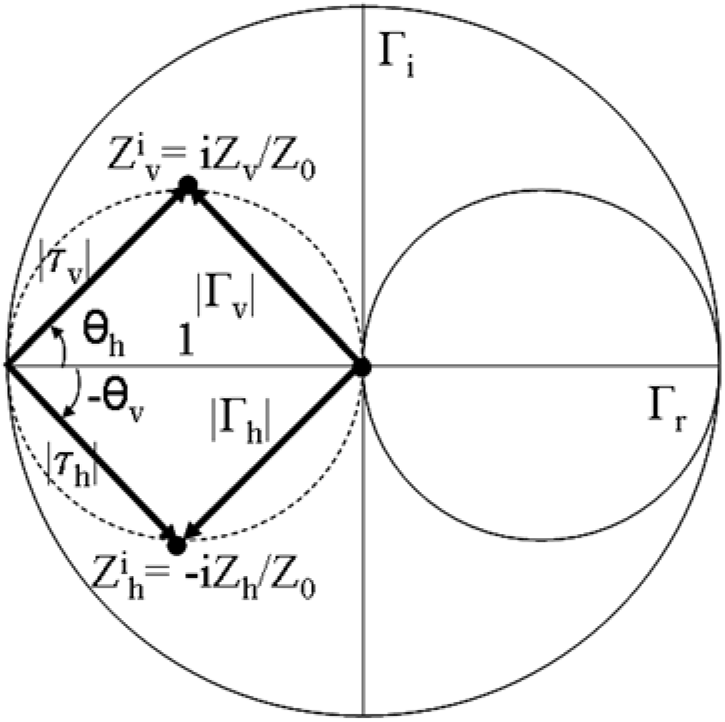

Figure 11 Simplified Smith chart showing the impedance experienced by the inductive and capacitive components (vertical and horizontal components respectively)

When the substrate impedance is included, the circle of constant resistance will no longer intersect with the center of the Smith chart. In Figure 12, the intersection of the circle of constant resistance, the solid line circle, with the Γ_r axis will be moved to the left as demonstrated in for light incident from free-space. For the angle of the transmission coefficient to remain unchanged, the impedance of the meanderline must decrease on a dielectric substrate. The magnitude of the reflection coefficient then increases, reducing the transmitted power. It is also observed that the angle of the reflection coefficient has also changed. This change in the reflection-coefficient angle and magnitude will mean that the reflected radiation will, in general, be elliptically polarized even when the transmitted radiation is circularly polarized.

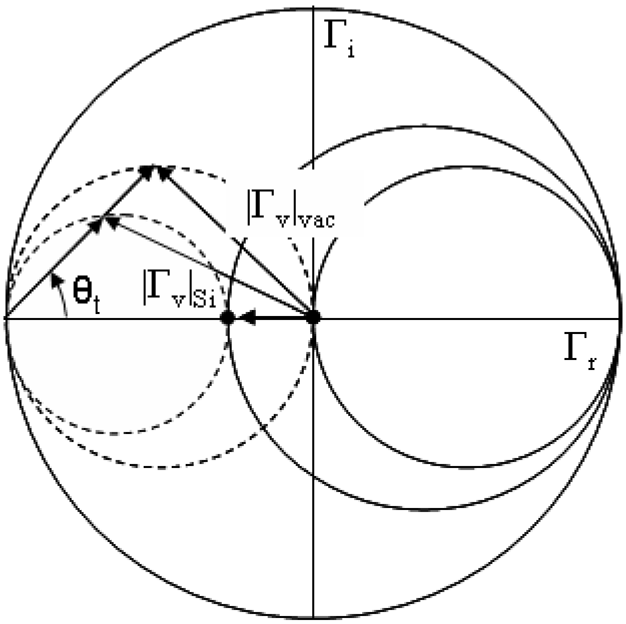

Figure 12 Smith chart plot showing the effect of having a substrate with a larger impedance than the characteristic medium. Note that the magnitude of the reflection has increased and its angle has also increased from the ideal 135°

By looking at the Smith chart it is realized that multiple layer meanderlines offer an opportunity to increase the power throughput of the meanderline while still retaining the desired state of polarization. By using multiple layers, new degrees of freedom are available to decrease the impedance mismatch of the overall structure. The thickness of a standoff layer will move the impedance point around the Smith chart on a circle of constant radius (equal to the magnitude of the reflection coefficient). If now another impedance layer can be placed to move the new rotated impedance point to the center of the Smith chart the meanderline will be a conjugate matched structure (ideally no reflections).

For an ideal double-layer meanderline, the total phase delay is split equally between the two layers for each polarization component. Therefore for a total phase advance of 45° for the inductive component, the phase advance induced by each layer should be 22.5°. The advantage of this is that if the multilayer meanderline is immersed in an isotropic material, the geometries will be identical. This translation about the Smith chart is shown in Figure 13 with position 1) being the impedance mismatch due to the first meanderline layer. Position 2) represents the input impedance including the effective propagation length of the standoff layer and position 3) shows the addition of the impedance of the second layer which is identical to the first. The final position is back to the center of the Smith chart which represents zero reflections. The concept can be extended to three layers conceptually by having $\theta_2 = 2\theta_1 = \theta_3$, with the end position also in the center of the Smith chart [4].

The Smith chart shows well the conceptual functionality of the meanderline retarder and how the different impedances experienced by the different linear polarization components affect the final state of polarization. The limit of the Smith chart becomes apparent when considering lossy materials. To handle the actual properties of the materials involved, a more comprehensive computational electromagnetics approach is necessary.

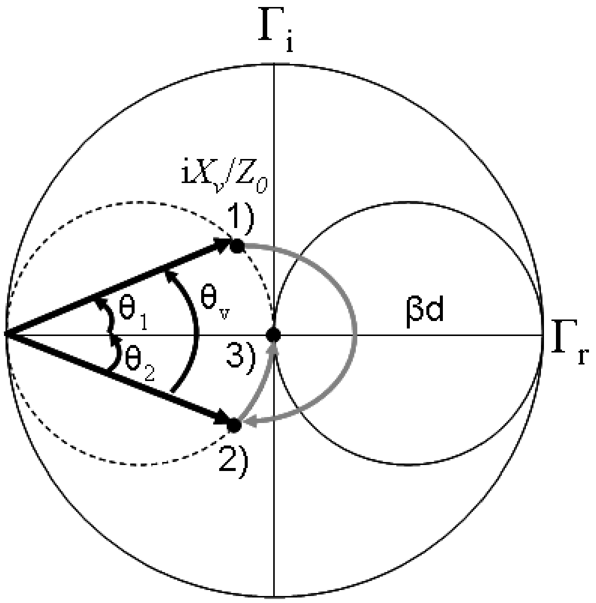

Figure 13 Smith chart showing the vertical component of an ideal two layer meanderline with 1) initial impedance of first layer, 2) change in input impedance due to propagation in standoff layer, and 3) the added impedance due to the second layer to a matched position for zero reflection at the center.

1.4.3 Off-Angles of Incidence

All discussion of the meanderline performance to this point has been concerned only with radiation at a normal angle of incidence. The performance of the meanderline for other angles is important as this property will determine its feasibility in a number of applications. To begin a discussion of nonzero angles of incidence and the corresponding meanderline performance, it is necessary to qualitatively look at the meanderline and its symmetry. The meanderline structure has bilateral symmetry rather than rotational symmetry, and therefore it is not expected that the performance of the meanderline will be the same for angles of incidence along both orientations.

The coordinate system set up for analysis of off-angle meanderline performance is depicted in Figure 14.

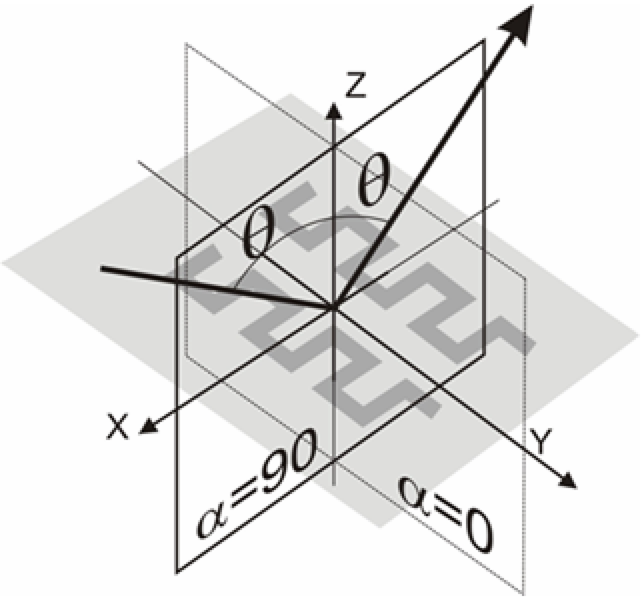

Figure 14 Schematic of the coordinates used in nonzero angles of incidence including the two planes of incidence used along α=0° and 90°.

As observed in Figure 14, the variable α determines the angle that the plane of incidence makes with respect to the meanderline axis. For α = 0°, the plane of incidence lies parallel to the meanderline axis and the angles of incidence, θ, lie in this plane. The other plane of incidence that will be characterized will be for α = 90°, having the plane of incidence perpendicular to the meanderline axis. With this system of coordinates, some conceptual observations can be made with respect to variation in performance as a function of angle of incidence.

Reference [14] demonstrates that the axial ratio of an ideal, non diffracting meanderline, as a function of incidence angle, will follow Equation 32 for the plane of incidence parallel to the meanderline axis.

$$AR(\theta) = \frac{AR(\theta = 0^\circ)}{\cos(\theta)} \qquad \text{Equation 32}$$

With this trend, the AR at the design frequency will degrade from an ideal AR of 1 to an AR of 2 at an angle of incidence of 60°. In this development TE is designated as the component of the incident polarization that is perpendicular to the plane of incidence, and TM is designated as the component of the incident polarization that is parallel to the plane of incidence. At normal incidence the ratio of the two incident orthogonal fields, TE and TM, are equal, however, as the incidence angle increases, the effective ratio decreases. This decrease occurs as the projection of the component parallel to the plane of incidence, TM, decreases in magnitude as the incidence angle increases. The component of the TM that is parallel to the direction of propagation cannot interact with the meanderline. Therefore, the only components that can interact with the meanderline are the TE and effective TM, TM_{eff}, which is the TM component decreased by the cosine of the incidence angle. This is demonstrated schematically in Figure 15.

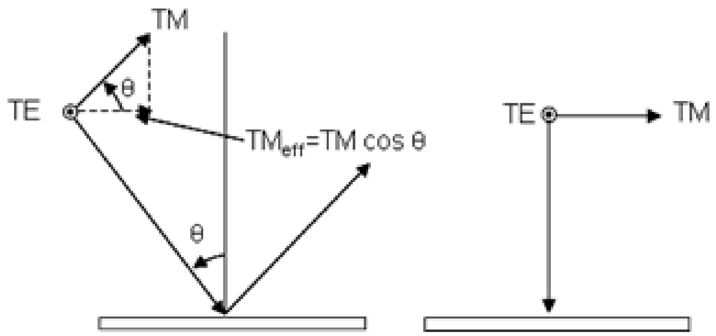

Figure 15 Schematic of how the projection of the initial transmission amplitudes along the TE and TM direction will change as a function of incidence angle. Note plane of incidence is the plane of the page.

Since the meanderline structure is periodic, it will be expected that there will be conditions in which diffractive effects will be observed [4, 20]. Specifically, the onset of diffraction effects as a function of incidence angle will be observable when the plane of incidence is along $\alpha = 90°$. The condition that a diffracted order will appear is given in Equation 33 in terms of the angle of incidence, θ_0, the angle of the diffracted lobe, θ_g, the diffractive order, s, the effective wavelength, λ_{eff}, and the period, dx. [24]

$$\left(\frac{dx}{\lambda_{eff}}\right) = \frac{s}{\sin\theta_0 - \sin\theta_g} \qquad s = 1,2,3... \qquad \text{Equation 33}$$

Therefore, an angle of incidence can be predicted in which diffractive effects will occur for a given periodicity in the meanderline structure. A plot of Equation 33 is shown in Figure 16. It shows the ratio of the period to the wavelength at which grating lobes occur for increasing angles of incidence. Note that no grating lobes occur for a period-to-wavelength ratio less than 0.5 and the first grating lobes that are visible are for grating lobe angles of -90° which is parallel to the interface. An added complication to the onset of diffracted orders is that their far field angular pattern is polarization sensitive for arrays that exhibit two-dimensional of periodicity, such as meanderline retarders. The effect of non-normal angles of incidence will be modeled and measured for each fabricated structure that operates as a quarter-wave retarder.

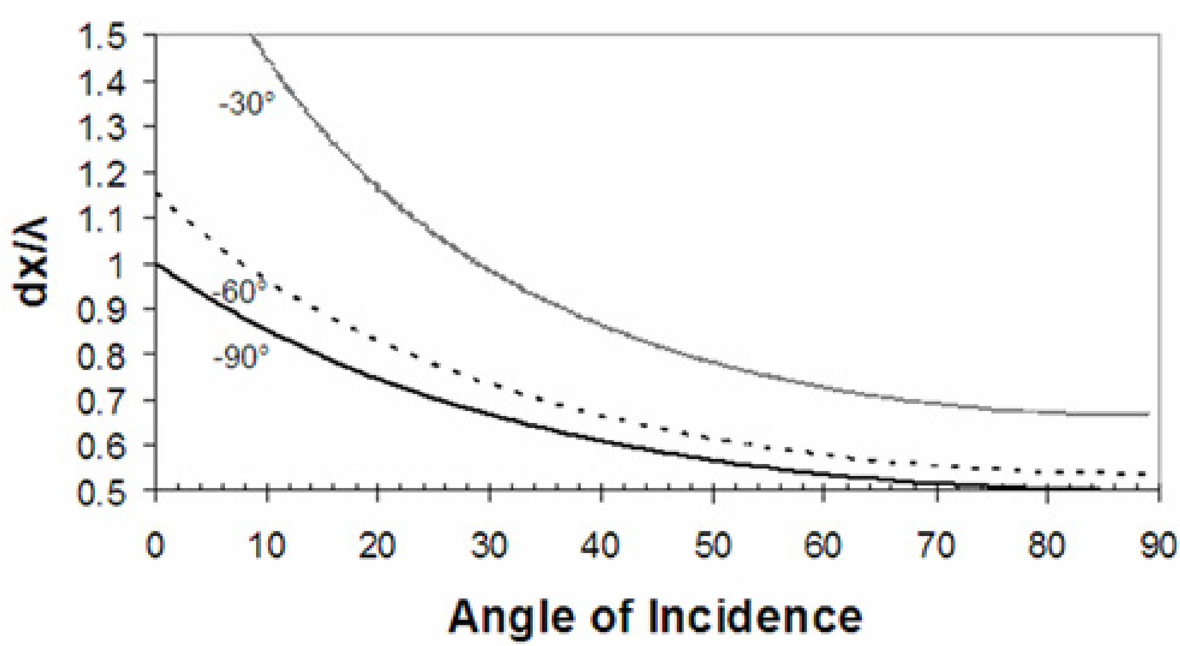

Figure 16 Plot of Equation 33 that shows the angle of incidence at which grating lobes at -90°, -60°, and -30° occur for a given ratio of element period to the wavelength.

1.4.4 Power Budget Analysis

Another important aspect of the meanderlines is the power budget. The power budget is used to determine the total percentage of power that is transmitted as compared to the total power incident onto the meanderline. The mechanisms for the reduction of transmission in a meanderline design come from reflections, caused by both the impedance mismatches of the meanderlines and dielectrics, the material attenuations in both the substrate and standoff layer, and the thermal loss due to the ohmic attenuation in the metal. The total transmission for a general meanderline with multiple layers can be represented as shown in Equation 34.

$$T = \left(1 - A_{\text{sub}}\right)\left(1 - R_{\text{meander}}\right)\left(1 - R_{\text{sub}}\right)\left(1 - A_{\text{standoff}}\right)^{p}\left(1 - A_{\text{metal}}\right)^{q} \qquad \text{Equation 34}$$

Equation 34 shows the transmission, T, as a function of the total absorption of the substrate, A_{sub}, the total reflection of the meanderlines, R_{meander}, the double interface reflection of the substrate, R_{sub}, the total absorption of the standoff layers, A_{standoff}, and the total ohmic loss of metal, A_{metal}. The variables p and q represent the number of standoff layers and metal layers, respectively. With the power budget analysis and the polarimetric analysis, the meanderline retarders can be compared to existing IR retarding technologies.

The organization of the dissertation from this point forward includes numerical modeling and incorporation of measured material optical properties. This approach will allow for the numerical computation of the impedance of the meanderline structure to predict the magnitude and phase difference between the transmission coefficients. The fabricated structures will be tested in reflection and transmission using an ellipsometer. These measured values will allow for an optimization loop to improve the agreement of predictions to the measured results. Wavelength-dependent trends in the phase delays and axial ratios will be determined using numerical modeling of the meanderline geometry. Once these trends are identified for a given design, a path forward for optimizing the phase delay and axial ratio can be chosen.

CHAPTER II
COMPUTATIONAL ELECTROMAGNETIC MODELING

Computational methods for electromagnetic modeling are well developed and allow for a comprehensive analysis of the meanderline [12, 16, 25-27]. The computational methods allow for a more complex model of the structure and inclusion of real optical properties of the materials. The inclusion of the optical properties allow for the minimization of assumptions, as long as the spectral dependence of the optical properties are known. The main reason for use of computational electromagnetics is that there are no analytic solutions available to determine the actual impedance, Z_m, induced by the meanderline geometry [1, 12, 16, 20, 25-27]. There have been attempts that define equations used to determine the impedance, however these equations are only valid over a specified spectral region and are empirical in nature [14, 18].

2.1 Modeling Methods

The modeling methods used for this research included a method-of-moments solver package, Periodic Method of Moments (PMM), designed by The Ohio State University for frequency-selective surfaces [4, 16, 20] and a finite-element method solver software package commercially available as Ansoft's HFSS. PMM was used to model the meanderline retarders and HFSS was used to model the wiregrid polarizer performance (described in Section 6.2). HFSS was attempted for modeling the meanderline structures, however it was limited by the increase in time due to the meshing and the limits on the approach for modeling non-normal angles of incidence. HFSS has two ways to model frequency selective surfaces, such as meanderlines: as a single unit cell inside a perfectly conducting waveguide and as a unit cell inside boundaries that enforce periodicity. The first approach can determine the amplitude and phase of both transmitted and reflected fields only for normal incidence via the S-parameters of a two-port waveguide. It is understood by the author that higher order modes can be excited within the waveguide to approximate non-normal angles of incidence, however the method to accomplish this was not found to be fruitful. The second approach in HFSS used a plane wave excitation and master/slave boundaries to enforce a periodic boundary condition. This approach does not work for the meanderline modeling since this setup only determines the amplitude of the reflection and transmission coefficients. There is no phase information, and therefore no polarimetric properties could be determined.

Meanderline retarders are frequency-selective surfaces (FSS), and share many of the attributes of electromagnetic interaction with the typical spectral filter FSS. The effect of the meanderlines are strongly determined by the coupling of nearby meanderlines, and rather than specifically altering the frequency response, the primary effect of this coupling is the anisotropic impedance that each polarization component experiences.

2.1.1 Periodic Method of Moments

The PMM solver was thus the choice to analyze the meanderlines. PMM allows for the definition of a reference cell that is used to determine the reflected and transmitted fields caused by a plane-wave excitation. Generally, antennas are used to receive an electric signal and transfer it to an analyzing circuit [15]. However, for FSSs, including meanderline retarders, the structures are arrayed and passive. They are not connected to a receiving circuit and the purpose is to modify the far fields of the incident radiation whether that modification is spectral filtering or polarization response. Also, FSS structures are generally spaced at small enough intervals so that electromagnetic coupling exists between the elements, thus determining the equivalent impedance of the structure requires a knowledge of both the self impedance of a reference element, and also the electromagnetic effects of the other elements on the reference element, called an array mutual impedance. [4, 20] PMM numerically determines the equivalent impedance of the meanderline structure both along and perpendicular to the meanderline axis using the mutual-impedance approach along with the simplification of a plane wave excitation. With the numerically determined impedance values, the complex transmission and reflection coefficients are able to be computed for both polarization components.

2.1.1.1 Impedance Properties of Periodically Arrayed Structures: Mutual Impedance Approach

To describe the concept of mutual impedance, an example will be developed involving two antenna structures [20]. Let antenna A be driven with a voltage, V_A. The fields radiated by antenna A will couple into antenna B and induce a current, I_B. Due to this current, antenna B will radiate and the radiated fields will interact with the currents in antenna A. The interaction will be an induced voltage according to Lenz's law and therefore the induced voltage will be opposite in sign to attempt to cancel the incident voltage. The voltage induced on antenna A by antenna B is equal to $-Z_{A,B} I_B$, where $Z_{A,B}$ is the impedance experienced by antenna A due to the interaction of antenna B also called the element mutual impedance. Using this example, the total voltage experienced by antenna A will be the sum of the driving voltage, V_A, and the induced voltage caused by antenna B. However, antenna A will experience a self impedance, $Z_{A,A}$, as well as its own load impedance, Z_A. The total voltage for antenna A will be the sum of the self and load impedance multiplied by the current of antenna A, I_A. Equating the two definitions of the total voltage on antenna A discussed above leads to Equation 35. The left hand side of the Equation 35 represents the total voltage on antenna A including the driving voltage and the contribution due to the mutual-element interaction. The right hand side shows the contribution due to Ohms law for the total voltage as a function of the self and load impedance.

$$V_A - Z_{A,B} I_B = (Z_{A,A} + Z_A) I_A \qquad \text{Equation 35}$$

Upon rearrangement and inclusion of the effects of antenna A on antenna B, Equation 35 can be shown in a form more conducive to matrix manipulation.

$$\begin{aligned} V_A &= (Z_{A,A} + Z_A) I_A + Z_{A,B} I_B \\ V_B &= Z_{B,A} I_A + (Z_{B,B} + Z_B) I_B \end{aligned} \qquad \text{Equation 36}$$

Equation 36 can be arranged into matrix formulation shown in Equation 37.

$$\begin{bmatrix} V_A \\ V_B \end{bmatrix} = \begin{bmatrix} (Z_{A,A} + Z_A) & Z_{A,B} \\ Z_{B,A} & (Z_{B,B} + Z_B) \end{bmatrix} \begin{bmatrix} I_A \\ I_B \end{bmatrix} \qquad \text{Equation 37}$$

Equation 37 shows the total equivalent impedance experienced by antennas A and B, which includes each element's self impedance summed with the mutual coupling effects of the other antenna. This concept can be extended to an infinite number of antenna elements and will retain a similar mathematical form. When modeling FSS structures, this formulation is the beginning of a method to determine the impedance matrix. The actual determination of the impedance of the meanderline using this method with no simplifications is time consuming. An assumption that can be made for simplification is plane wave excitation of the structures, as seen in the next section.

2.1.1.2 Impedance Properties of Periodically Arrayed Structures: Plane Wave Expansion Approach

The actual problem of solving for the array mutual impedance, which includes the total sum of the element mutual impedances, is difficult [20]. To simplify the computation, approximations are made that the source of excitation is a plane wave and that the array extends to infinity. The driving voltages are thus considered to be excited by a plane wave and the currents are constrained to being composed of a set of known basis function, *i.e.* piecewise sines and cosines, with an unknown amplitude. These simplifications reduce the computation time necessary to determine the equivalent impedance of the meanderline structure.

With these approximations, some simplifications then alleviate the difficulty of determining the array mutual impedance. The incident plane wave is propagating along the direction of the Poynting vector.

$$\hat{s} = s_x \hat{x} + s_y \hat{y} + s_z \hat{z} \qquad \text{Equation 38}$$

This plane wave will induce currents on all of the elements with the same amplitude as a reference element in the array. The element currents will also have a phase relation that is determined from their displacement from the reference element in the periodic array. This phase difference is due to the different optical paths that the plane wave must undergo to reach each of the elements as it propagates, particularly for non-normal angles of incidence.

With these simplifications, the computational determination of the mutual impedance matrix, and the far fields, both transmitted and reflected, can be made. These two concepts are introduced here for a qualitative perspective of the numerical approach for determining the equivalent impedances of the meanderline structure via PMM [20].

2.1.1.3 Using Frequency Dependent Permittivity in PMM

PMM in its default form is designed to include the use of the material electrical and magnetic properties in its computation for the transmitted and reflected fields [28]. However, since the program was designed to be used for the RF, it was not equipped to handle a frequency dependent permittivity or permeability. In the RF regime, the imaginary part of the permittivity tends toward zero and the real part of the permittivity tends toward a constant. Therefore, in the RF, a spectrally static value for the permittivity is an accurate approximation. However, in the IR there exist many molecular vibrational modes and phonon-photon interactions that lead to spectral attenuation [29, 30]. These attenuations are perturbations in the imaginary part of the permittivity which then mean that a corresponding perturbation in the real part must take place, according to the Kramers-Krönig relations [29, 30]. These changes in the optical properties must be taken into account in the modeling to improve the correlation between modeled and measured results. The method by which this inclusion of the frequency-dependent optical properties was accomplished in PMM is discussed thoroughly in Reference [23].

The frequency dependent PMM code as written can accept frequency dependent values for both dielectrics and metals [23]. In the RF, the conductivity is primarily defined by the imaginary part of the complex conductivity since the real part is much smaller than the imaginary part at these frequencies [29, 30]. However, in this research, the IR properties of the metals used in this research were measured on the ellipsometer and the *n* and *k* values were then interpreted into frequency dependent conductivities using the Drude model oscillators in the ellipsometry analysis, discussed in Section 4.2.1. The permittivity in a free-charge-dominated system, like metals, is given by

$$\varepsilon_r = 1 + \frac{i}{\varepsilon_0 \omega}\left[\sigma_r + i\sigma_i\right] = 1 - \frac{\sigma_i}{\varepsilon_0 \omega} + i\frac{\sigma_r}{\varepsilon_0 \omega} \qquad \text{Equation 39}$$

In Equation 39, ε_r is the relative permittivity of the metal, ε_0 is the permittivity of free space, ω is the angular frequency of the radiation, and σ_r and σ_i are the real and imaginary parts of the conductivity. Since the loss contribution in the relative permittivity is determined by its imaginary part, the real part of the conductivity contributes to ohmic loss. The functional relationship between the complex conductivity and the measured complex IR constants is

$$\sigma_r(\omega) = 2nk\varepsilon_0\omega \qquad \sigma_i(\omega) = (1 + k^2 - n^2)\varepsilon_0\omega \qquad \text{Equation 40}$$

In Equation 40, n is the refractive index, k is the extinction coefficient, and ω is the angular frequency. The conductivities as measured were complex and the real and imaginary parts of the conductivity were similar in magnitude and no approximations could be made, especially for the MWIR region. The problem with the inclusion of the complex conductivities into the PMM code is that PMM uses a sheet resistance value to determine the conductive nature of the metal. The inputted sheet resistance can only be a real value in PMM and therefore the measured complex conductivity cannot be included explicitly into the model. This is somewhat more accurate in the LWIR where the imaginary part is still larger than the real part of the conductivity.

The method used to determine an acceptable approximation to the sheet resistances at these frequencies was developed that allowed for reasonable agreement between measured and modeled results. The method to do this was to fabricate a meanderline and measure the geometric parameters using a scanning electron microscope (SEM). The measured geometric parameters would then be input into PMM and the meanderline thickness measured using a Veeco Dektak 3 mechanical stylus profilometer on a witness sample after metal deposition. The fabricated meanderline would then be measured on the ellipsometer. Using the known response of the meanderline and the measured geometric parameters, PMM would be run and a sheet resistance would be determined that best fit the measured results. The best fit sheet resistance value will be given for each meanderline design.

The limitation of this method is that the measured conductivity can not be incorporated in the modeling of the meanderlines. However, it was determined that the modeled results had much more correlation to the measured results using this empirically determined equivalent sheet resistance than the approach of using just the imaginary conductivity as measured on the ellipsometer. It is also important to note that the real part of the conductivity, which cannot be incorporated into PMM, contributes to added phase delay without extra power loss. This is seen in the relation given in Equation 39 since the real part of the conductivity corresponds to the imaginary part of the permittivity. This contribution to the imaginary part of the permittivity will increase the impedance mismatch and change the transmitted and reflected field magnitudes.

Therefore, when the real part of the conductivity is important to the total conductive response, the only option that is available to fit the data is to increase the assumed sheet resistance. Increasing the sheet resistance does indeed increase the phase delay, but since it is increasing the value of the imaginary part of the conductivity to do so, the loss is also increased. This increase in loss will offer reliability when predicting the polarimetric parameters of interest, but in general it will cause the modeled transmission coefficients to be lower than those measured. The ratio of the transmitted coefficients will be unaffected by the extra loss but the absolute transmission coefficients may vary from measured transmissions. The exception to this will occur when the imaginary part of the conductivity is considerably larger than the real part in which the metal will behave similarly to the RF regime.

2.2 Meanderline Functional Tolerance Study for Geometrical Parameters

The tolerance study for the geometric parameters of the meanderline retarder was performed using PMM to determine the trends in performance of a specifically designed meanderline to variations in the different geometrical parameters. Knowing the sensitivity and change in performance of the meanderline for geometric variations allowed for a more efficient method of optimizing performance. This characterization is necessary to give the designer an idea of how each of the geometrical parameters affects the polarimetric properties of the transmitted radiation, since there is no analytical representation for the meanderline impedance as a function of the geometric variables. The geometrical parameters of the meanderline are: pulse width (*pw*), pulse height (*ph*), width (*w*), and period (*dx*). As long as the thickness is at least six skin depths, the variation in the thickness of the metals will not vary the performance of the meanderline structure as the currents will reside primarily at the surface of the metals. The geometric parameters are schematically shown in Figure 17.

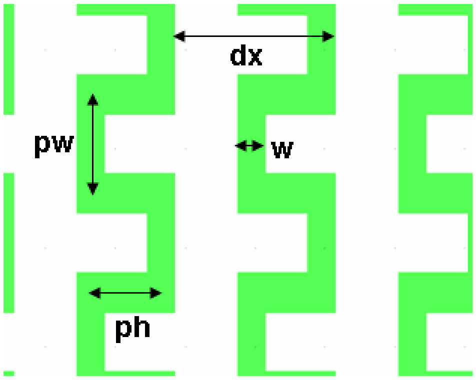

Figure 17 Schematic of meanderline structure showing the geometric parameters

The *pw* and *ph* are both referenced from the center of the strip and *dx* is the distance from a given point on the meanderline to the same point on the neighboring meanderline. The advantage of using these variables is that they are all independent of the width of the strip, *w*.

The model investigated for the tolerance study was the single layer meanderline quarter-wave retarder on the Si substrate. Using the single layer design a single parameter can be changed and the results quickly determined. From Section 5.1.2, the dimensions for the optimized single layer meanderline were: pw = 0.9 µm, ph = 0.8 µm, dx = 1.45 µm, and w = 0.6 µm. The performance is shown in terms of the axial ratio and phase delay. This study was done to identify the general trends in the phase delay and axial ratio as various geometric parameters were varied. The trends that are found in the tolerance study will be used in the design process to optimize the polarimetric properties of the designs studied.

The first investigation was to observe the effect of changing the width, *w*, of a meanderline layer. Conceptually one would expect the impedance of the component along the meanderline axis to become larger as *w* increased. This would lead to a larger phase delay due to the increased inductive impedance that would be expected as the width increased [4]. However, along with increasing the phase delay, there will be a larger mismatch in impedance leading to more reflected power. This would lead to an expectation that the total transmitted power would also be decreased. The modeled analysis shown in Figure 18 shows the variation of the width in the single layer meanderline as it increases from 0.2 µm to 0.6 µm in increments of 0.2 µm. The modeled results show a distinct change in the phase delay as the width is increased. The phase delay at a wavelength of 10 µm increases from 58° to 94° as the width increased from 0.2 µm to 0.6 µm. The AR shows a minimum at a wavelength of 11 µm with a width of 0.2 µm. This minimum location shifts to 10.5 µm as the width increases to 0.6 µm. This spectral shift in the AR is small and demonstrates that the width of a meanderline structure can be increased as nearly a free variable to increase the phase delay. The increase in phase delay is gained without a large shift in the minimum location of the AR as the width is increased with all other parameters held constant.

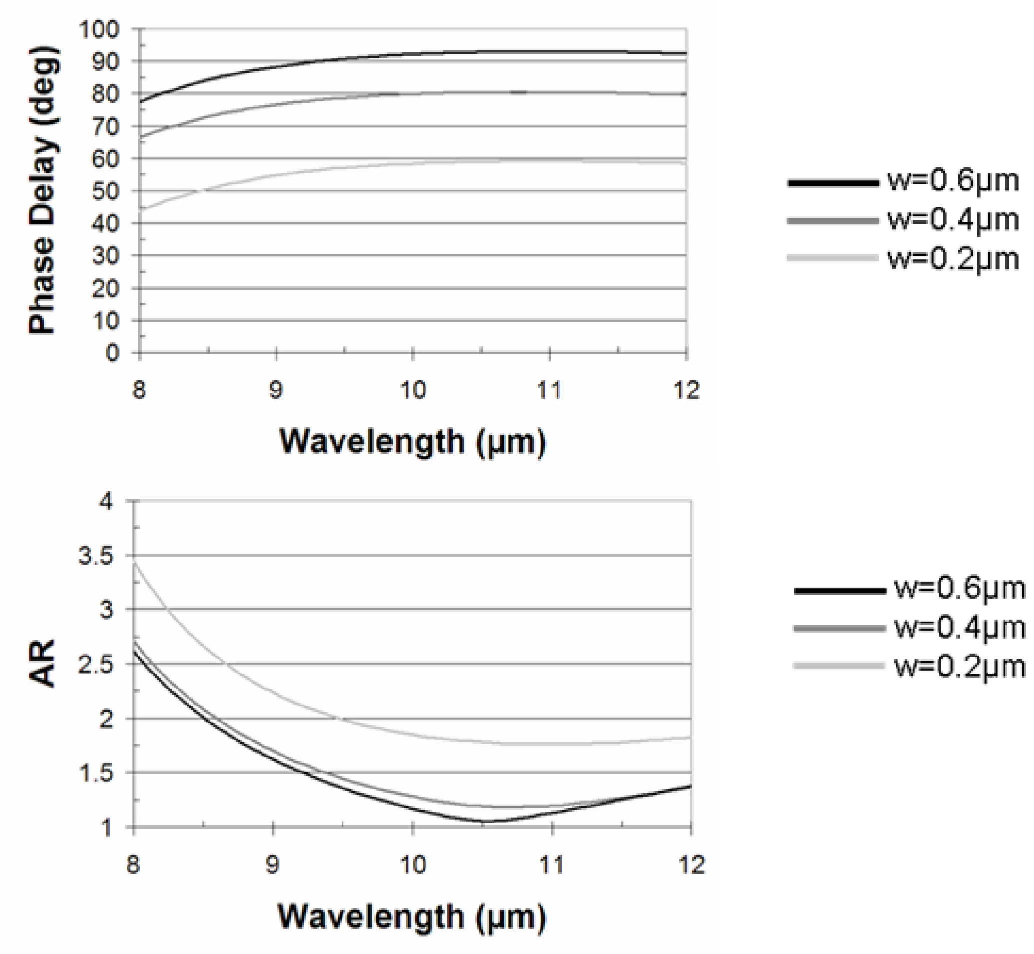

Figure 18 Modeled relative phase delay (top) and axial ratio (bottom) for the various meanderline widths shown at right

The next parameter that was varied was the meanderline pulse width, *pw*, while all the other parameters were held constant. The conceptual perception for the impact of *pw* on the meanderline performance was primarily dependent on the relative size of *pw* to *ph*. If the *pw* became much larger that the *ph*, it would be expected that the structure would act more like a linear polarizer. However, such sizes were not investigated since the desire was to induce and control the phase delay. The *pw* was varied from 0.9 µm to 1.1 µm in steps of 0.1 µm to determine the trend of increasing the *pw*. The results of the modeling are shown in Figure 19. From Figure 19 the variation of *pw* seems to have a minor impact on the phase delay and axial ratio of the meanderline.

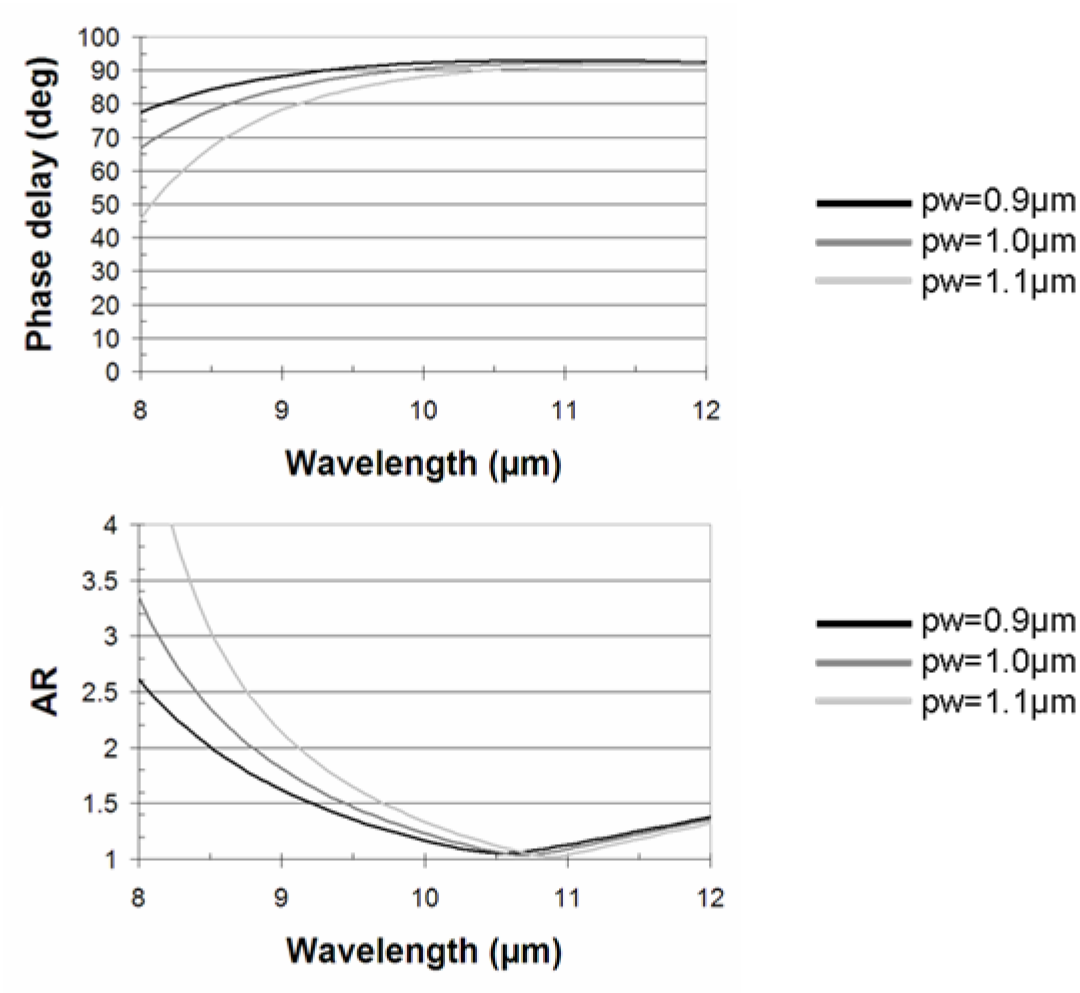

Figure 19 Modeled relative phase delay (top) and axial ratio (bottom) for the various meanderline pulse widths (*pw*) shown at right

The next parameter that was varied was the pulse height, *ph*. The *ph* is a constrained value since it can be no larger that the difference between the period and the width, *dx* – *w*, to prevent overlap between the adjacent meanderlines. The modeled result for this investigation is shown in Figure 20 where the *ph* was varied from 0.6 μm to 0.8 μm in steps of 0.1 μm.

A conceptual prediction of the effect of varying the *ph* prior to the numerical modeling was limited to an expectation that the resonance location where AR is equal to 1 would shift. The numerical results for the effect of varying the *ph* shows that the variation in the *ph* significantly shifts the minimum AR spectral location while only mildly affecting the phase delay.

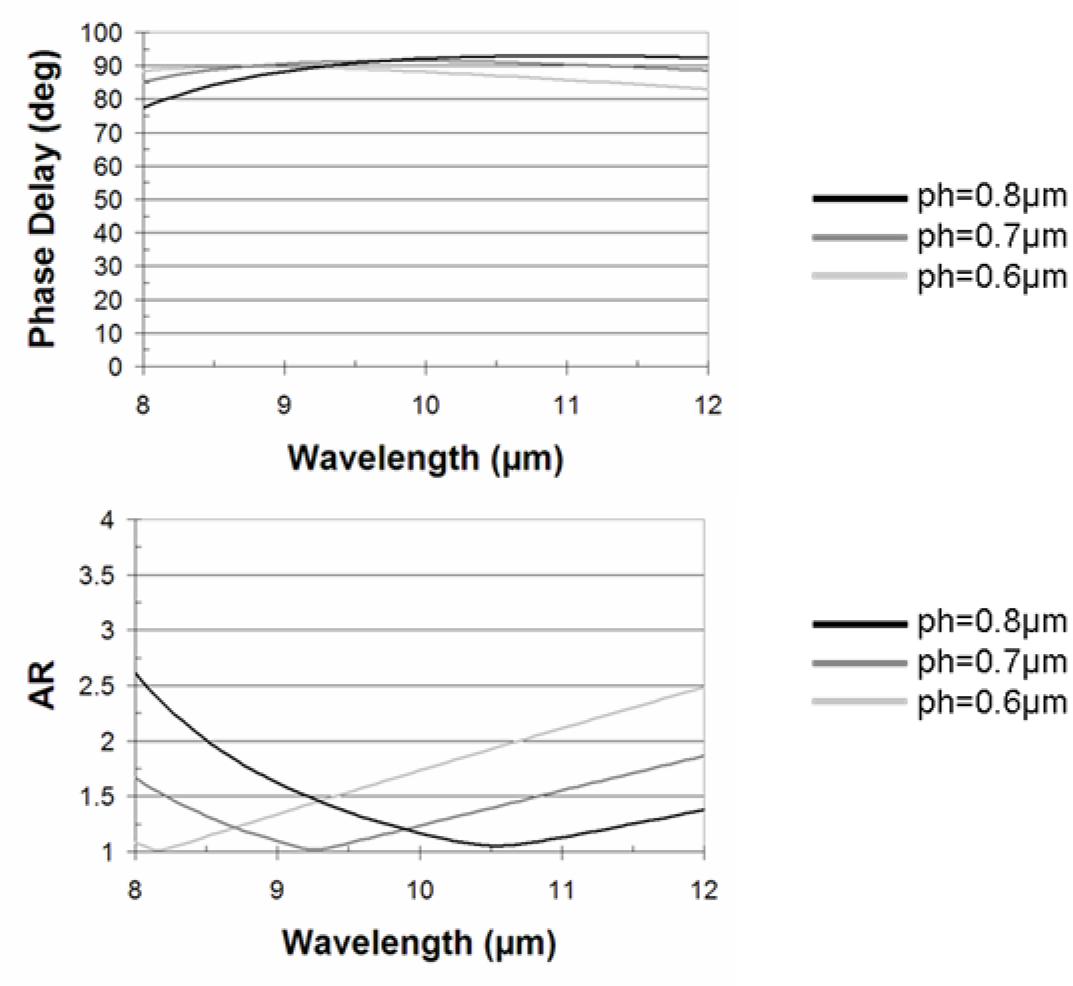

Figure 20 Modeled relative phase delay (top) and axial ratio (bottom) for the various meanderline pulse heights (*ph*) shown at right

The final geometric parameter varied was the spatial period, *dx*, of the meanderline structure. The *dx* variable is expected to have a strong impact by increasing the impedance as it decreases. This is caused by the expected increase in the electromagnetic coupling between the meanderlines as *dx* decreases. This coupling should increase both the inductive and capacitive impedance components as *dx* decreases. Therefore a net increase in the relative phase delay would be expected for a decrease the period. There should also be a higher transmission as the period increases since the impedance mismatch would be lower, leading to lower reflections. The modeled results for the variation of the period is shown in Figure 21 for *dx* ranging from 1.5 µm to 1.9 µm in increments of 0.2 µm. Figure 21 shows that a decrease in *dx* increases the phase delay. It is also seen that the minimum spectral location of the AR does not shift as *dx* changes.

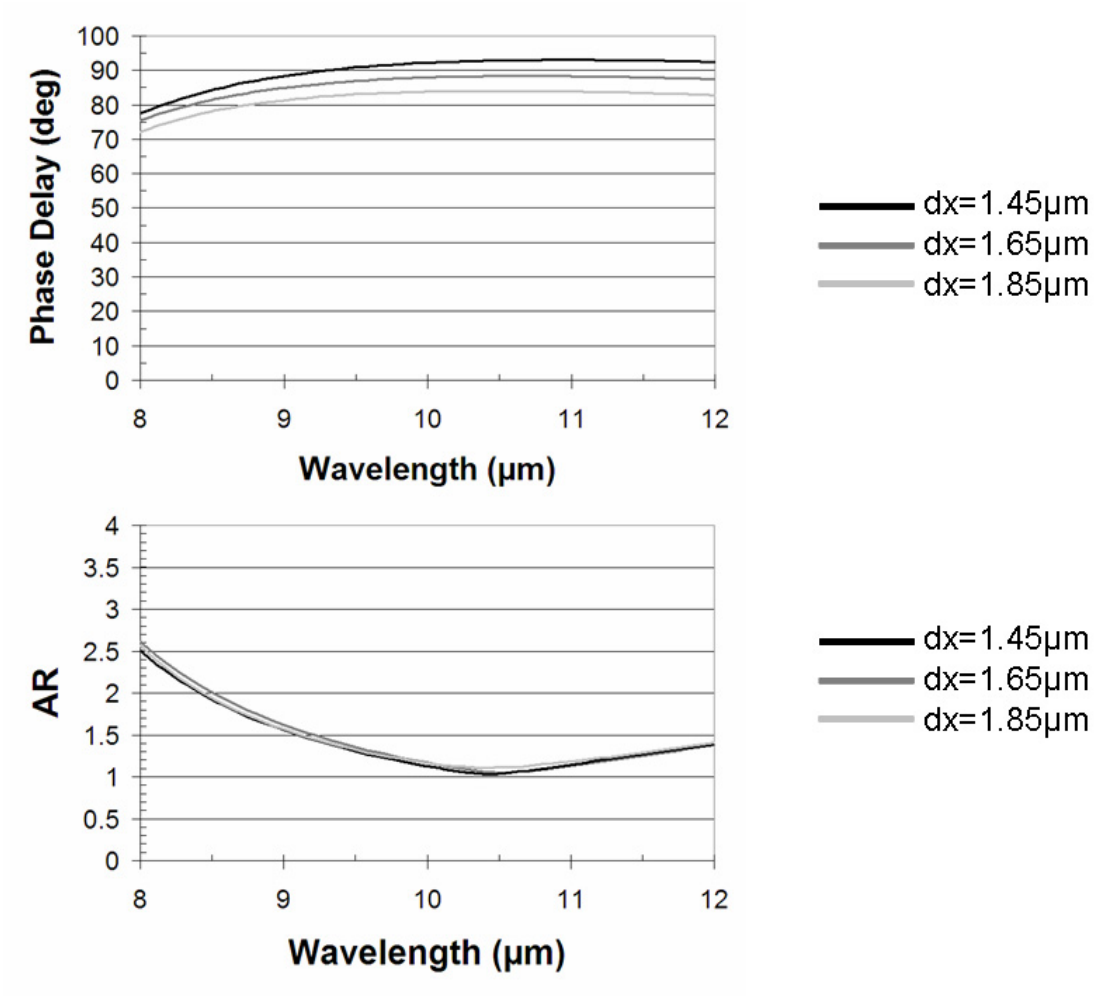

Figure 21 Modeled relative phase delay (top) and axial ratio (bottom) for the various meanderline periodicities (*dx*) shown at right

The purpose for the tolerance study was to develop a notion for the impact of changing the geometric parameters of the meanderline structure on its performance. After the initial scaling down of an RF design by the ratio of the RF wavelength to the effective IR wavelength, the study shows different design variables that can be left to the meanderline designer to achieve the performance to meet a particular specification. The geometric parameters that are the most useful for varying the phase delay are *w* and *dx*. As either *w* or *dx* is decreased, the phase delay is increased while having minimal effect on the location of the spectral minimum of the AR. To vary the spectral minimum of the AR, the *ph* shows the best effect. As the *ph* is increased the spectral minimum of the AR is shifted to shorter wavelengths while not significantly altering the phase delay.

2.2.1 Meanderline Design

Unfortunately, as mentioned previously there is no analytical method by which a meanderline retarder can be designed. However, as seen in the previous section, there are trends that occur in the performance of the meanderline retarder as the geometric parameters are varied. These trends can be utilized to quickly determine a ‘good’ meanderline retarder for the desired function. The challenge is optimizing the geometric parameters to have the highest overall transmission, the flattest spectral axial ratio, and a flat spectral phase delay that is at a desired value.

The extension of these aforementioned concepts is valid for multiple-layer meanderline structures as well. The ideal standoff layer thickness is one quarter of an effective wavelength [4].

$$d_{\text{standoff}} \sim \frac{\lambda}{4n} \qquad \text{Equation 41}$$

In Equation 41, d_{standoff} is the standoff layer thickness between meanderline layers, λ is the free space wavelength, and n is the refractive index of the standoff layer. The benefit of using multiple layers is that the impedance mismatch at each of the layers will become smaller and there will be a higher overall transmission.

2.3 Fabrication Tolerances

One of the important aspects of fabricating the meanderline structures is an understanding of the tolerances that the geometry can have and still perform well. Due to the definition of the geometries, the parameter that is most susceptible to fabrication constraints is the meanderline width, w, since the other parameters are all defined in terms of the centerline of the meanderline structure as shown in Figure 22. As the meanderline is written, the fidelity between the pattern input into the e-beam writer and the actual pattern written into the resist is excellent. The variation in w arises when the pattern is developed. The development time determines the ultimate fidelity of the pattern. If the pattern is underdeveloped, there will be resist that remains on the wafer in the patterned regions. The resist in the patterned regions will cause all of the metal to be removed during the lift off process. If the pattern is overdeveloped, w will increase beyond that intended and the contrast will decrease, *i.e.* edges will become rounded. The width is controlled by doing dose matrices and geometry characterizations, which will be discussed in Section 3.1.2. The other geometric parameters define the centerline of meanderline structure except for the period which describes the spacing between the meanderlines, as shown in Figure 22. These variables, when fabricated, are limited in their precision only by the interferometric stage in the Lieca EBPG system. Hence the errors in these variables will be minimal when compared to the initial pattern file parameters.

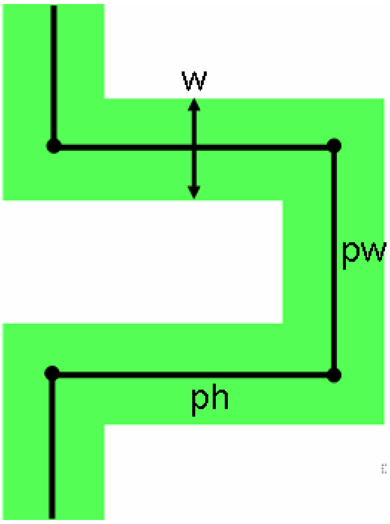

Figure 22 Schematic showing that *w* is the primary variable that will be susceptible to fabrication constraints since all the other variables are defined by the centerline of the meanderline structure.

CHAPTER III
FABRICATION TECHNIQUES

Though the modeling of the meanderline retarders offers insight to the potential for their operation in the IR, it is necessary to fabricate and characterize device performance to obtain measured data to allow for iterative performance optimization. In the laboratory in which these structures were fabricated, there was ready access to an electron beam pattern generator and metal/dielectric deposition equipment. There was also ready access to resources to complete the characterizations of the various processes necessary to fabricate the various designs presented in this dissertation including a JEOL scanning electron microscope and a Veeco atomic force microscope. The fabrication procedures for select structures characterized, in Chapter V, are located in the appendix.

3.1 Electron-Beam Lithography

Electron-beam (e-beam) lithography and photolithography are the two primary methods of patterning resists although other technologies are being developed such as nano-imprint lithography. Photolithography is primarily limited by the wavelength-dependent diffraction limit of the light being used. There is ongoing research to decrease the wavelength of the light to the UV and EUV, however currently, e-beam lithography is the best method to fabricate sub-micron linewidths. For all of the fabrication in this dissertation, e-beam lithography was used.

The advantage of e-beam lithography is that the electrons can be focused to very small beam spots on the order of nanometers. The primary resolution limitation of e-beam lithography is the aberrations that the focusing electric and magnetic field elements induce, much like optical aberrations, and the chromatic aberrations due to the finite energy spectrum of the impinging electrons. Even with these issues, lines have been written to widths of 20 nm. Another advantage for e-beam lithography is that the pattern file can be changed very easily using a CAD program rather than writing an entire mask as would be necessary for photolithography and nano-imprint lithography. However, the drawback is that the e-beam write is a serial process involving a raster scan of the electron spot. Also, the beam requires time to settle on each location and the required dose must be administered depending upon the resist choice, beam current, and spot size. Therefore e-beam lithography can require a large amount of time.

3.1.1 Fundamentals

The e-beam lithography was accomplished using a Leica EBPG 5000+ e-beam writer. The system can operate at voltages of 20, 50, and 100 kV, however it was kept at 50 kV for all the writes for this work. The EBPG has 4 holders for certain types of substrates and these include: 4” wafer, 3” wafer, piece parts (up to and including 2” wafers), and a 5” mask holder. The 5” mask holder is design to hold commercially available blank masks with a thickness of 0.09”. Our lab obtained blank Al plates with the same dimension as a 5” mask and used our in-house machine shop to machine desired geometries for lithographic processing including optical flats with a diameter of 2” and a thickness of 1/8”. These are high-tolerance dimensions as there is a maximum ±50 μm of tilt allowed over the entire wafer. Various thicknesses of sheet metal are used to shim the flats to the required tilt tolerance. The tilt is checked on a microscope outfitted with an interferometeric stage, laser, and quad cell detector. The process for preparing a file for writing begins with the initial drawing of the pattern to be written. The program in which the pattern is designed does not necessarily matter as long as the final pattern file is in a GDSII format signified by the file suffix *.gds. The program used for the work was L-Edit (Tanner Research, Inc). This software allows for the design of multilayer patterns and is centered around a hierarchal geometrical format. This allows complicated geometries, especially arrays, to be built from less complex unit cells.

Once the GDSII file is prepared, it must be converted to the file type required by the Leica EBPG which is a *.gpf file. This conversion is begun by fracturing the GDSII on a Linux workstation via Synopsys CATS software into trapezoidal segments. This essentially means that all of the geometries to be written are converted into trapezoidal mosaics as an approximation; therefore any geometry with curved features will require many trapezoids to approximate the curve to within a specified tolerance. The fracturing involves inputting a desired beam spot size, which is determined by the beam current and sets the resolution, and beam step size, which determines the center-to-center distance between two spots. The resolution determines the fine incremented grid that the fractured pattern is mapped onto. The importance of the beam spot size is that it is a function of the beam current, which plays a role in determining the speed at which the pattern will be written. The higher the beam current, in general, the larger the beam spot due to the mutual repulsion of the electrons. Also, the larger the current, the faster a required dose is reached at a given location and the faster the write will proceed. The beam step size also plays a role in determining the speed of the write as is shown in Equation 42. The maximum writefield size is 800 μm by 800 μm. The upper limit is due to the unacceptable beam distortion due to the scanning. The larger the sweep the larger and more elliptical the beam spot will become. The meanderline structures are rectilinear and are readily converted from the *.gds to the *.cflt format for fracturing. The final format after fracturing in CATS has the file type *.cflt. The file must then be converted to a file type that is specific to the Leica EBPG which is the final *.gpf file. The beam step size and beam current along with the necessary dose for exposure determine the frequency that the EBPG can write. The frequency represents the number of spots the EBPG can expose in a second. This relationship is shown in Equation 42. The maximum write frequency that the Leica EBPG system will write is 50 MHz which is considerably faster than outfitted SEMs that tend to write with frequencies in the kHz range.

$$f[MHz] = \frac{0.1 \cdot I_{beam}[nA]}{dose\left[{}^{\mu C}\!/_{cm^2}\right] \cdot \left(stepsize[\mu m]\right)^2} \qquad \text{Equation 42}$$

For all of the writes in this work, a single e-beam resist was used, ZEP520A-7, and it was chosen because of the very low dose necessary to expose the resist. The other resist commonly used, poly(methyl methacrylate) (PMMA), has a required dose that is up to six times that necessary for ZEP. This directly leads to write times that are correspondingly six times longer for PMMA than with ZEP. The specific doses used for the fabrication are mentioned in the Appendix, noting that the dose varies with the material environment around the resist layer. The desire for shorter write times is caused by the very large arrays that are necessary for the characterization of the meanderline retarders. Simply to characterize a meanderline structure, a minimum area of 6 mm by 6 mm is necessary for the use of the ellipsometer, discussed in Section 4.2. To gauge the time of write comparisons, a 1 cm^2 area of meanderlines takes approximately 1 hour to write in ZEP, using a

25 nA beam, while the corresponding area using PMMA would require up to 6 hours, which can become quite costly for large structures.

3.1.2 Characterizations

To have repeatable geometries for the meanderline retarders in the e-beam write, it is necessary to determine the dose that is required to expose the resist to achieve a desired geometry. If the resist is overdosed, it is much like an overexposed image in photography as there is lower contrast and lines become wider and corners become rounded. The dose is very sensitive to the geometry of the meanderlines, since they are in such close proximity to one another. This occurs because as the high energy electrons enter the substrate there are two general phenomena that will occur, elastic and inelastic scatter. The elastic scattering changes the angle of propagation of the electron without changing its energy. Inelastic scattering causes energy loss in the electron via many different processes including auger electron emission, X-ray emission, and secondary electrons. Since the elastically scattered electrons change the direction of their propagation, there is a certain probability that they will scatter laterally in a substrate and back to the source. These backscattered electrons can expose regions in the resist outside the patterned file. This effect is especially pronounced in densely packed geometries, such as meanderlines and therefore any change in the geometry will likely change the necessary dose for exposure. The dose for each of the substrates used is different due to the different electrical environments and compounded with the different geometries. The dose for each of the fabricated geometries is described in the Appendix.

Other aspects to e-beam lithography that are important for line-width concern are the thickness of the resist being used, and the thickness of the metal being deposited. The rule of thumb is that the thickness of the metal should be about one third of the thickness of the resist for a clean liftoff. The other rule of thumb is that the minimum achievable line width is on the order of the thickness of the resist. Both rules tend to give good starting points for fabrication and they were used in this research.

3.1.2.1 E-beam Lithography on High-Resistivity Silicon Substrate

Silicon is the most commonly used substrate in our research group and therefore the best characterized under a variety of geometries from isolated bond wires to densely packed frequency selective surfaces. Silicon was ideal for initial fabrications of structures for operation in the LWIR. For the initial meanderline designs, silicon was used to correlate models to measurements because of the pre-existing fabrication techniques. The two fabrication process for the silicon substrate are described below with the first being the process for a minimum achievable line width of about 400 nm and the second for a minimum achievable line width of about 150 nm.

The wafer was first thoroughly cleaned by spinning the wafer during sequential rinsing with three organic solvents: acetone, methanol, and isopropyl alcohol (IPA). After cleaning, the wafer was heated to 180°C for 3 minutes as a dehydration bake, to remove any residual water from the substrate. The resist was spun onto the substrate, without an adhesion promoter, at a speed of 3000 rpm producing a uniform ~315 nm layer of resist. After spinning the resist, the wafer was heated on a hotplate for 4 minutes at 180°C to bake out the solvent. The pattern was then written at a 50 kV accelerating voltage using a beam current of 25 nA, to achieve an approximate spot size of 25 nm. This spot size was chosen since the initial desired line width was expected to be about 400 nm or so, and it allowed for 16 exposure spots for the width. This is more than is needed but allowed for a 25 nm increment in the widths which gave more flexibility in the geometrical constraints used in the modeling. After exposure, the wafer was developed in ZEP RD, xylene, for 1.5 minutes and rinsed with IPA. To ensure that there was no residual resist in the developed regions, the wafer underwent plasma etching in a Branson barrel etcher for 2 minutes. The 420-mTorr O_2 plasma was excited by an RF power of 200 W.

The second goal was to achieve an expected minimum line width below 200 nm, it was necessary to use thinner resist. There are two methods to reducing the thickness of the resist, to dilute the resist in a solvent, which for ZEP is anisole, or to simply spin the resist at a higher spin speed. Spinning faster is more convenient but not as flexible since most spin charts show an asymptotic thickness after a certain speed. However, in our case, spinning faster gave the desired results. By increasing the spin speed to 6000 rpm the thickness was reduced to about 215 nm. The remainder of the process was identical to the recipe already presented for the thicker resist.

The next step was to characterize the line widths as fabricated. The experiment that was done was to take a meanderline design, hold the period at a constant value of 1.45 µm, and vary the widths in the pattern file from 75 to 275 nm. The goal was to determine what the true widths of the lines were for a given input width, at a constant period. The resulting images of the fabricated meanderlines are shown in Figure 23. It is seen in the figure that the fabricated widths did indeed differ from the design widths but that their relationship was linear over the design widths ranging from 100 to 250 nm corresponding to true widths of 130 to 320 nm. The standard deviation bars correspond to the measurements of the widths in various positions in the array. The important conclusions made were that the actual width, as a function of a design width, will be linear over a rather large range for a given period, and that the lines are typically overexposed by about 50 nm. As an observation, it is also seen in the SEM images in Figure 23 that the proximity effect becomes quite noticeable as the edges become closer and rounded as they approach the neighboring structures more closely.

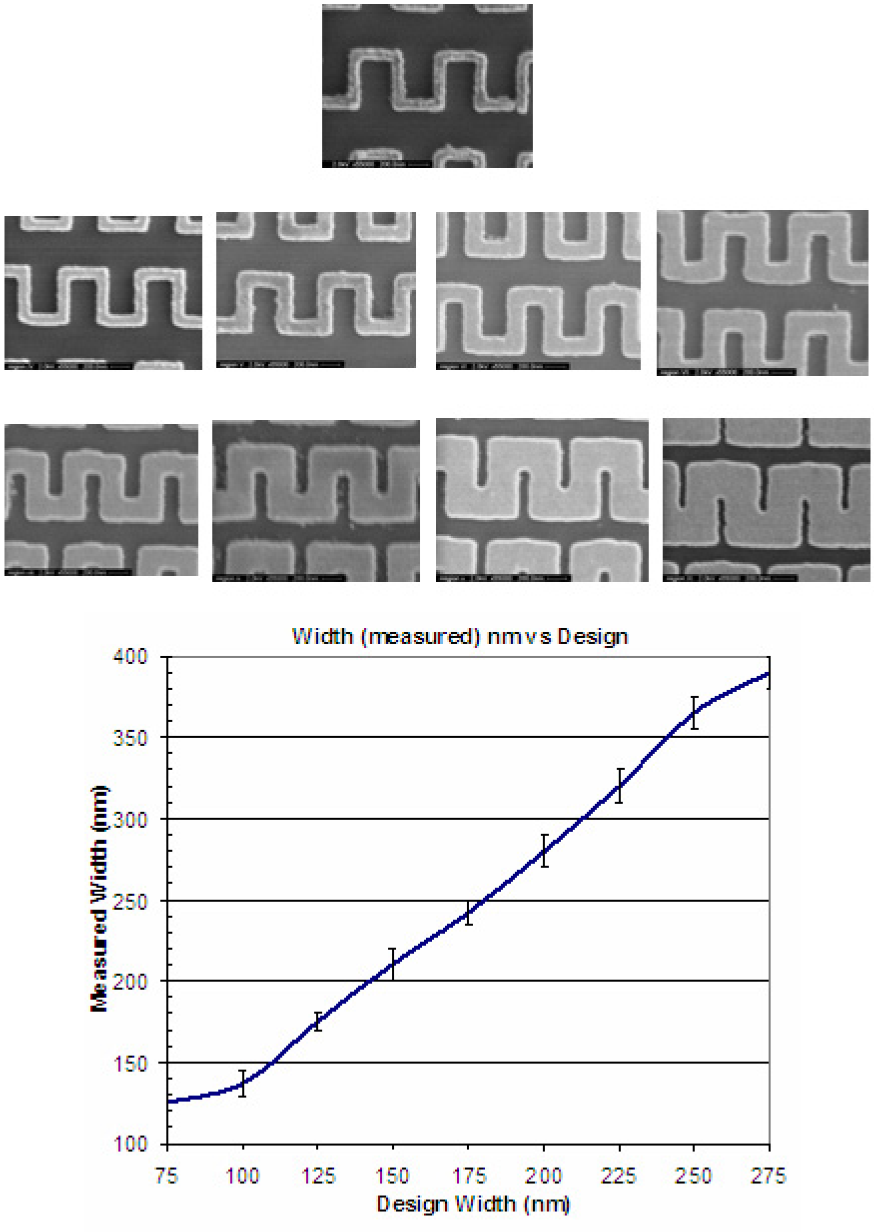

Figure 23 SEM images of the fabricated meanderline with 215 nm thick resist (top) and plot of the measured widths as a function of the design widths (bottom)

3.1.2.2 E-beam Lithography on Fused Silica Substrate

For the meanderlines that were to function in the MWIR from 3 to 5 µm, fused silica was used as the substrate since it passes radiation well from about visible to 4.5 µm. The complication with fused silica is that it is a very good dielectric and it is transparent at visible wavelengths with a low electrical permittivity. This means that while the electron beam is incident on the resist above, the charge has no route to ground. The result is that the charge will lodge itself much like a static electric charge on a TV screen. This stored charge is a problem because the electrons that are accelerated toward the resist now experience a repulsive force from the accumulated charge and the beam will sweep erratically causing severe pattern fidelity problems including stitching errors for writes larger that a single write field. To prevent this in the case of fused silica, a conductive layer is needed to allow dissipation of the charge. For the Si this was not a problem because, even though it was high resistivity Si, it was conductive enough to dissipate the charge effectively. As will be seen, typical method to negate this problem is to either put a metal layer beneath or above the resist.

Also, the transparency of the fused silica is not a problem with the electron beam itself, but rather the method by which the Leica EBPG measures the height of the writing surface. The EBPG uses the specular reflection of a laser, λ=633 nm, to determine the surface height via a calibrated quad cell detector. This essentially means that the surface that is to be written needs to be reflective at a wavelength of 633 nm, in order for the EBPG to adjust the focus of the electron beam to keep a constant beam spot and circular spot shape.

These two problems both have solutions that were investigated: sputtering a very thin metal layer on top of the resist and applying a spin-on-conductive polymer (Mitsubishi-Rayon's AquaSAVE) above the resist with a thin metal region on two sides of the wafer for reflection measurements. It is of note that it is necessary to sputter or thermally evaporate the metal rather than use electron-beam evaporation because during an e-beam evaporation there are enough backscattered electrons from the crucible and metal to expose all of the resist, thereby ruining it for further lithographic processing.

The process of sputtering Au onto the ZEP solves both the problem of electrical discharge and poor reflectivity without exposing the resist with stray highly energetic electrons. There is also an advantage that the EBPG can measure the height at all points that it writes since the entire surface is reflective. The problem with using the Au layer over the entire substrate is that the Au needs to be removed before the resist can be developed. An effort was made to use Transene's gold etch TFA, which is a KI-I_2 complex solution and cyanide free, however the etchant attacked the ZEP520A-7 resist very quickly. Another problem was that RF sputtering has a much lower deposition rate than does DC sputtering and the wafer had to statically remain beneath the target causing unwanted heating of the ZEP resist. Therefore the metal deposition process was changed to a DC sputtering of Ni which can be removed by Transene thin film nickel etchant TFB which is nitric-acid based. There was some degree of success with this etchant as it attacked ZEP slowly, but it still attacked the resist causing the resist to rip off of the fused silica substrate.

The method that worked the best at removing the Ni layer was the use of cleanroom-quality floor tape. The Ni, when sputtered onto ZEP, has very poor adhesion, and as case in point a person can rub their glove over a region coated by Ni and some of the metal would come off. The initial efforts involved Scotch brand desk tape, but it is very narrow and required many attempts to remove all of the Ni. When the Scotch tape comes into contact with the ZEP resist, some of the adhesive remains on the resist preventing development, since the best solvent for the adhesive is acetone which also dissolves ZEP. The cleanroom-quality floor tape was wide enough to cover the entire wafer and was smoothed down gently to remove all air bubbles. When the tape was gently lifted, the Ni was removed entirely with a single use of the tape and the development process could continue with no problems. Since the Ni layer was the only surface that came into contact with the adhesive, no adhesive residue remained on the resist allowing for good development.

3.1.2.3 E-beam Lithography on Barium Fluoride Substrate

Barium fluoride (BaF_2) is commonly used as an IR window since it has a very high transmission (~95%) from UV to approximately an 11.5 μm wavelength. It also has a very low refractive index with an index of 1.4 at a wavelength of 10.5 μm. There have been no published articles concerning e-beam lithography on BaF_2 as of this writing and a process had to be developed. The physical properties that were most important for working with BaF_2 were that it is highly susceptible to both thermal and mechanical shock. Both of these properties make BaF_2 difficult to work with from the perspective of resist processing since the entire wafer will have to bake at 180°C. BaF_2 is also a salt and readily dissolves in both alkaline and acidic solutions.

Special BaF_2 wafers were ordered from Global Optics (UK) Ltd. with the specifications of a 50.4 mm diameter ± 0.1 mm and a thickness of 3.10 mm +0.00/-0.05 mm. The wafers were also ordered to be optically flat ($\lambda/10$ at 633 nm) which more than satisfied optical flatness at the IR wavelengths of interest in the MWIR and LWIR. These dimensions were desired since they matched the dimensions of previously used optical flats, as mentioned in Section 3.1, and the holder for lithography in the EBPG was already available.

The e-beam lithographic processing for the BaF_2 was similar to the fused silica processing. A thin Ni layer was also sputtered onto the BaF_2 but the biggest difference came in the ZEP processing. When baking the ZEP on fused silica wafers, the typical bake times are between 4 and 5 minutes and then the wafers are promptly removed from the hotplate. However, for BaF_2, it was necessary to allow the BaF_2 wafers to cool slowly to room temperature. This basically meant that the ZEP was baking for much longer than the 4 minutes, and this increased baking reduced the solubility of the ZEP in the organic solvent methylene chloride. Therefore to successfully remove the ZEP for liftoff processing it was necessary to use Zeon Corporation's ZDMAC ZEP Remover.

3.1.2.4 Multi-Layer Lithography

In order to have multiple layer meanderline retarders, it was necessary to develop processes that would allow for multiple layers. For the work presented, there were two different materials used for standoff layers: silicon and BCB. The silicon was used for the meanderline retarders fabricated onto silicon substrates for operation in the LWIR while the BCB was used for the fused silica and barium fluoride substrates for operation in the MWIR and LWIR, respectively.

The process for using silicon as a standoff layer is shown schematically in Figure 24. The first meanderline layer is fabricated and silicon is then e-beam evaporated onto the structure to a thickness of 400 nm. Electron-beam evaporation is a very conformal method of deposition, and since the meanderlines have a thickness of ~100 nm, a vertical 100-nm profile will be present after evaporation. This deviation of planarity does not allow for good lithography, and it was necessary to planarize the surface. Initial efforts were concerned with the possibility of mechanically polishing the surface, but that was not successful. The path forward was determined to be the use of a spin-on dielectric, BCB. The optical properties of BCB are discussed in Section 4.3.4.

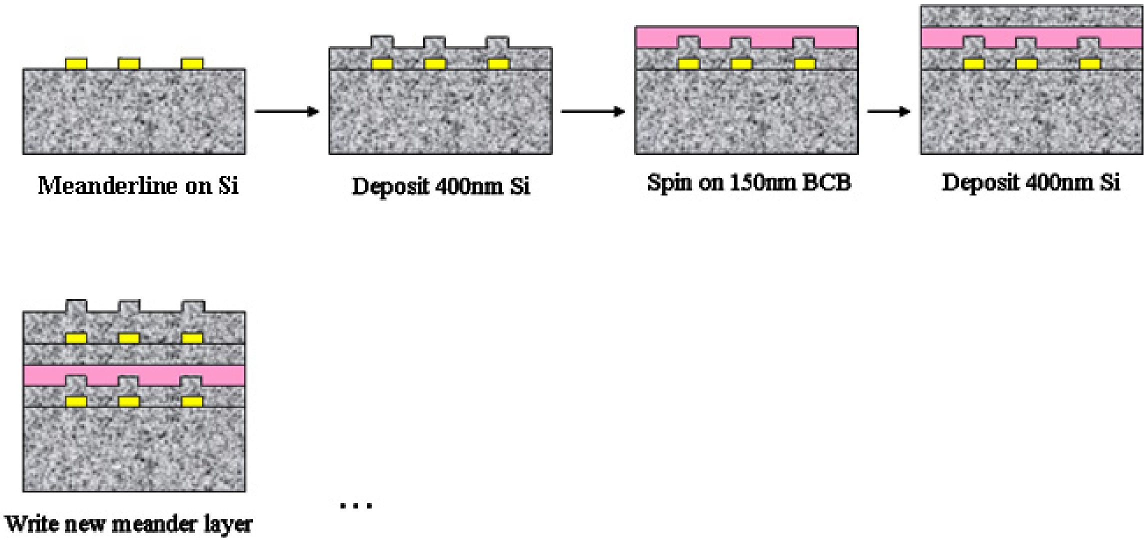

Figure 24 Flow chart showing the fabrication of the multiple layers using silicon

BCB was spun onto the surface at a thickness of 150 nm. To get this thickness, it was necessary to dilute the BCB from its original concentration. The BCB was diluted using mesitylene in a ratio of 10 parts BCB to 30 parts mesitylene by weight and spun at a speed of 3000 rpm to achieve the desired thickness of 150 nm as measured on the ellipsometer. As a demonstration of the increased planarity, an atomic force micrograph was taken after depositing silicon to a thickness of 890 nm and then again with the BCB layer spun onto the surface. These images are shown in Figure 25. The images in Figure 25 show the un-planarized surface at left with a surface peak-to-peak roughness measured to be at about 80 nm. After the application of the BCB, the peak-to-peak surface roughness decreased to less than 10 nm, which is suitable for electron-beam lithography.

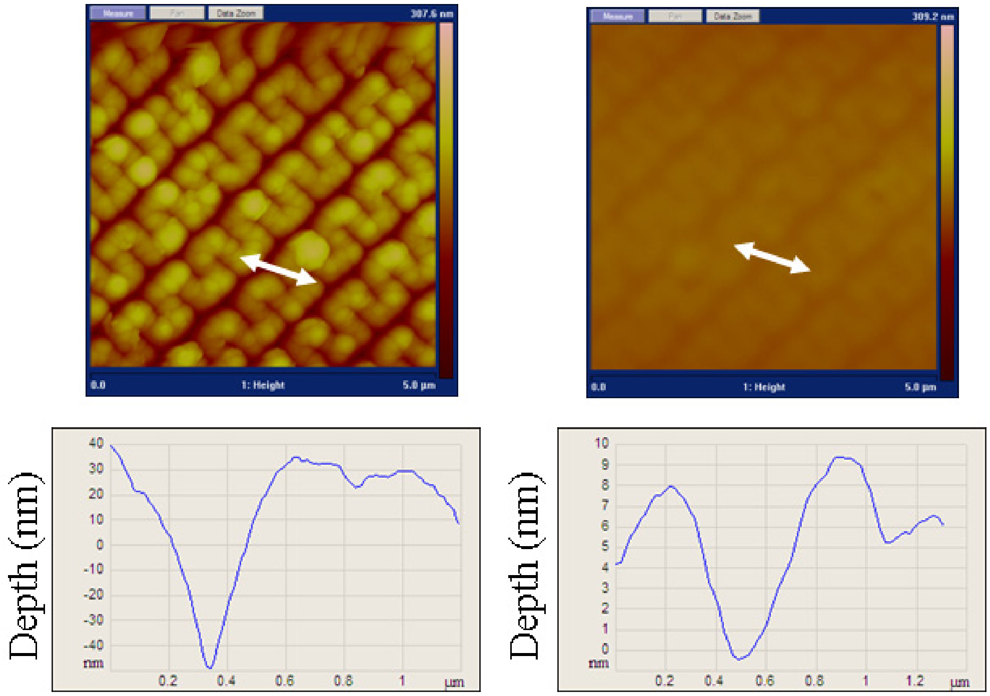

Figure 25 Atomic force micrographs of the surface profile as a function of distance along the inset arrows after (left) 890 nm Si deposition and (right) 890 nm Si deposition with 150 nm BCB spun onto the surface. Note the factor of 10 improvements in peak-to-peak roughness as measured after the BCB layer.

The BCB layer was also suitable because of its adherence to the silicon layer, and was also a good substrate for the silicon evaporation since the silicon adhered to the BCB in the same manner as the BCB adhered to the silicon. This point is significant, in that it has been observed that just because one material adheres well to another as a substrate does not imply that the reverse is true.

3.2 Thin Film Fabrication Techniques

During the course of this research it was necessary to deposit different metals and dielectrics. The methods by which these depositions were made involved physical vapor deposition (PVD) processes including thermal/electron-beam evaporation and DC/RF sputtering.

3.2.1 Electron-Beam Evaporation

The electron-beam (e-beam) evaporations were done in a BOC Edwards evaporation system. The system has four water-cooled copper pockets on a revolving platter that allow for the changing of materials during e-beam evaporation without breaking vacuum. This feature is necessary for any materials that require a separate adhesion layer to be evaporated prior to the desired material. It also has two thermal evaporation holders for added flexibility.

E-beam evaporation basically involves focusing and accelerating (4.65 kV) electrons emitted from a cathode onto a target material. As the electron beam hits the target material the material resistance will induce thermal heating of the material. Upon reaching the evaporation temperature, at the surrounding pressure, the atoms will have sufficient kinetic energy to be ejected from the evaporant and coat a target wafer. The temperature of the evaporant is controlled by varying the filament current to within a precision of 1 mA. It is important that the chamber pressure be sufficiently low so that the mean-free path of the ejected atoms is larger than the distance from the evaporant to the target wafer for good line-of-sight deposition. For the purpose of this research the chamber pressure was always lower than 1×10^{-5} Torr to promote repeatability in the thin film properties and ensure excellent directionality. This low pressure also reduces the rate at which impurities can grow while evaporating a material, and is especially a concern when evaporating materials that readily oxidize as this will reduce the purity of a thin film.

Inside the chamber, a quartz crystal is used to monitor the thickness of the evaporated material on the wafer. The piezoelectric quartz oscillator has a resonant frequency that changes because of the added mass of the films and in this way the thickness of the film on the crystal can be found if the density of the material (g/cm^3) and its acoustic impedance ($g/cm^3/s$) are known. To convert the thickness measured at the crystal monitor to a value that corresponds to the thickness at the wafer, a witness sample is placed in the chamber and the thickness is measured after evaporation using a Veeco Dektak 3 mechanical stylus profilometer. The thickness as measured is compared to the thickness at the crystal and the ratio between the two is the tooling factor that is saved in the control panel. The crystal is usable until it accumulates a layer thickness of 200 nm at which point it is replaced.

Another important aspect of thin film fabrication is the consideration of adhesion to a substrate surface. There are two primary methods for producing good adhesive properties at an interfacial layer of two different layers: covalent bonding over a thickness range of many atomic spacings and diffusive bonding. The covalent bondings occur frequently as a result of depositing an oxidizing metal onto an oxide substrate. A good example of this is Ti evaporated onto a Si substrate as Ti readily oxidizes to TiO_2 and Si always has a thin native SiO_2 layer at the boundary allowing some of the Ti to form TiO_2 compounds within the SiO_2 lattice. This covalent bonding works well for thin films however generally as the film becomes thicker the high stresses at the interface lead to poorer adhesion. However not all metals readily form oxides, such as Au, and thus adhere poorly to oxide substrates. To promote adhesion for these metals, a thin film of oxidizing metal (Ti, Cr, or Ni) is generally evaporated for good adhesion to the substrate. Directly following this evaporation, and without breaking vacuum, the inert metal is evaporated and adheres to the intermediate layer. If the vacuum is broken or too much time lapses between the evaporations, the boundary between the oxidizing metal and the vacuum will oxidize thereby reducing the adherence of the inert metal to the intermediate layer. [31]

3.2.2 RF/DC Magnetron Sputtering

Evaporation is preferred for the purposes of metallizing a lithographic pattern to promote good liftoff. However, when fabricating on transparent substrates it was necessary to deposit a thin metal layer above the e-beam resist layer to allow for electronic discharge and reflectivity as discussed in the section concerning e-beam lithography. Most of our currently characterized metal films are deposited using e-beam evaporation, and this process is not feasible for depositing a metal film above the e-beam resist. This is due to the fact that there are enough electrons backscattered from the evaporant to expose the highly sensitive electron beam resist, thereby ruining it for later processing. The remedy for this was to sputter the thin metal film, which worked well for both Ni and Au.

The system used in this research is a Materials Research Corporation 8667 sputtering system that allows for both DC and RF sputtering capabilities. The system has two DC targets and one RF target that can be changed readily.

3.2.2.1 DC Sputtering Basics

Sputtering is essentially the bombardment of inert gas ions onto a target surface with the intention of ejecting the target atom from the surface. The inert gas ion, generally argon, originates from the plasma discharge environment. In the case of DC sputtering, the plasma is set up by first taking a chamber to a low vacuum ($\sim 10^{-5}$ Torr) and adding the flow of an inert gas. The pressure of the chamber will increase to a minimum of about 10 mTorr and then a high DC potential is induced between the target and the substrate. Since it is the Ar^+ ions that actually collide with the target, the target must be at a high negative potential with the substrate generally grounded. Once the plasma is ignited, the Ar^+ ions will sputter the target onto the substrate.

To improve the rates of deposition and to more easily sustain the plasma discharge, magnets are arranged on the back of the target in a ring. All of the magnets are arranged to have one pole toward the center of the ring and the other pole pointing away from the center. This arrangement of magnets sets up a magnetic field that traps electrons in a helical trajectory near the target. The advantage of this is to increase the collision rates of the Ar gas with the ionizing electrons as opposed to the linear paths without the magnetic field. The increased density of ionized Ar leads to larger sputter rates without having to increase the pressure to unacceptably high levels. However, it also causes non-uniform consumption of the target in the region of higher ion density, generally appearing as a worn out ring on the target. This non-uniform consumption causes non-uniform sputter coverage of the substrate as compared to electron beam or thermal evaporation. There is an advantage of using the DC sputtering technique due to the entrapment of energetic electrons away from the substrate, and this is what prevents the electrons from potentially exposing sensitive e-beam resist that may be on the substrate. DC sputtering allows for a high rate of deposition of metals. However, if insulators are the desired target RF sputtering is necessary.

3.2.2.2 RF Sputtering Basics

The purpose of RF sputtering is to offer a means by which an insulating material can be deposited. If an insulating material were to be DC sputtered there would be no path by which the charge could dissipate, which would ultimately limit the current. By changing the potential source from a DC to an AC source the RF voltages can be coupled to any material, conductive or insulating. Another advantage of RF sputtering is that there is uniform target consumption, leading to more uniform depositions than with DC sputtering. The RF sputter system used for this research operated at a frequency of 13.56 MHz.

For further reference of the applied and theoretical aspects of both DC and RF sputtering, consult Reference [31].

CHAPTER IV
INFRARED MATERIAL-CHARACTERIZATION TECHNIQUES

For all of the structures that were fabricated, it was necessary to characterize the various aspects of their functionality and the optical properties of the materials used. The meanderline retarders were primarily characterized using transmission ellipsometric techniques. The materials that were used to fabricate the structures include the necessary substrates, metals, and standoff layers. Each of these materials was investigated so that the various characteristics of each were known to ensure the materials with the most desirable properties were used. All of the materials used in the construction of the meanderlines were analyzed individually using ellipsometric techniques to determine the necessary optical constants for the bands of interest. The various thin film thicknesses of the standoff dielectrics were also ascertained ellipsometrically.

4.1 Stokes Parameter Measurement at 10.6 µm

The proof-of-concept meanderline design was initially characterized with a laser to determine whether it would function as expected. The wavelength of characterization was 10.6 µm using a CO_2 laser as the source. The polarization change caused by the meanderlines was characterized using the Stokes parameters of the input and output beam. Our experimental setup, shown in Figure 26, included a linearly polarized CO_2 laser beam, two BaF_2 wire-grid polarizers, and a quarter-wave plate. Two thermal detectors were used, with one used to calibrate for laser-power fluctuations. The Stokes parameters were determined, in the usual way, through a set of power measurements. The first power measurements were made without the quarter-wave plate in the optical train and with the analyzing polarizer rotated from 0 to 360 degrees. The resulting dependence of received power as a function of the analyzing polarizer angle was fitted to a periodic function, and I_0, I_{45}, and I_{90} (the power measurements along the angles in subscript) were determined from the fitted curve. The angle 0° corresponded to an orientation parallel to the meanderline axis. The other power measurement was with the quarter-wave retarder in the optical train (fast axis horizontal) and the analyzing polarizer at 45 degrees, producing the value I_{q45}. The Stokes parameters were then calculated using [6]

$$S_0 = I_0 + I_{90} \qquad S_1 = I_0 - I_{90} \qquad S_2 = 2\, I_{45} - S_0 \qquad S_3 = 2\, I_{q45} - S_0 \qquad \text{Equation 43}$$

The Stokes parameters are then used to determine the orientation (ψ) and AR of the polarization ellipse using [6]

$$\tan(2\,\psi) = S_3 / S_0 \ \text{ and } \ AR = 1 / [\, \tan(\, \tfrac{1}{2} \sin^{-1}(\, S_3 / S_1 \,)\,)\,] \qquad \text{Equation 44}$$

From the standard deviation of the power measurements with respect to the fitted curve the uncertainties in the retardance, Stokes parameters, orientation, and AR can be calculated [32]. This characterization process was used for initial measurements, however it was determined that the IR ellipsometer would be better suited, faster, and offer a spectral characterization of the structures. The Stokes parameter determination was used for the measurements presented in Reference [33].

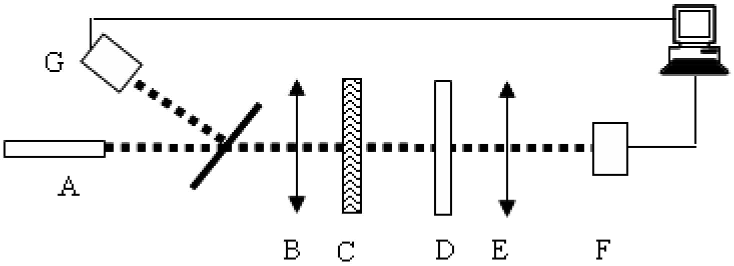

Figure 26 Schematic of the experimental setup: A) CO2 laser; B) wire grid linear polarizer; C) meanderline; D) quarter-wave plate; E) analyzing polarizer; F) & G) signal and reference detectors connected to a computer for data acquisition.

4.2 Ellipsometer

Ellipsometery has been used as a precise and flexible method of determining the optical properties of both bulk and thin film materials. The basic advantage is that to determine the optical properties at a dielectric interface all that has to be done is to measure polarization change in the light as it reflects from the surface. This allows for measurement of the optical properties since the amplitude and phase of the reflected fields will be functions of the real and imaginary refractive index, as described by the Fresnel reflection coefficients for both the electric field in and perpendicular to the plane of incidence. The superposition of the orthogonal reflected fields will have a characteristic polarization ellipse, and, assuming no de-polarization, a power measurement can be used to determine the ellipsometric parameters of interest.

The ellipsometer used for the measurements reported in this dissertation was the infrared variable-angle spectroscopic ellipsometer (IR-VASE), manufactured by J.A. Woollam Co. and shown in Figure 27. The source of the ellipsometer is a glowbar filament source with a variable

DC power supply for fine control of the brightness. The spectral range of the ellipsometer is limited by the gray body spectrum of the globar, and there is typically enough power in the spectrum for characterizations from 2 to 40 μm using Fourier transform infrared (FTIR.) spectroscopy. This method basically uses a Michelson interferometer with a nominally incoherent source to measure the interference pattern as a function of mirror displacement, which is essentially a measurement of the spectral autocorrelation of the source. Thus, the Fourier transform of the autocorrelation determines the power spectrum of the source. This procedure offers fast determination of power spectra and high spectral resolution, which is limited by the accuracy of the motion of the stage that holds the moving mirrors. The ellipsometer also holds the sample and detector on rotational stages that allow for ellipsometric measurements at many different angles of incidence for both reflection and transmission modes. The extra angles of incidence offer more data for the fitting software to use, giving a higher precision to the inferred properties.

The advantage of having the ellipsometer with the FTIR configuration is the quick determination of transmission and reflection spectra with different initial linear polarization settings. This was especially useful in the spectral characterization of the meanderlines.

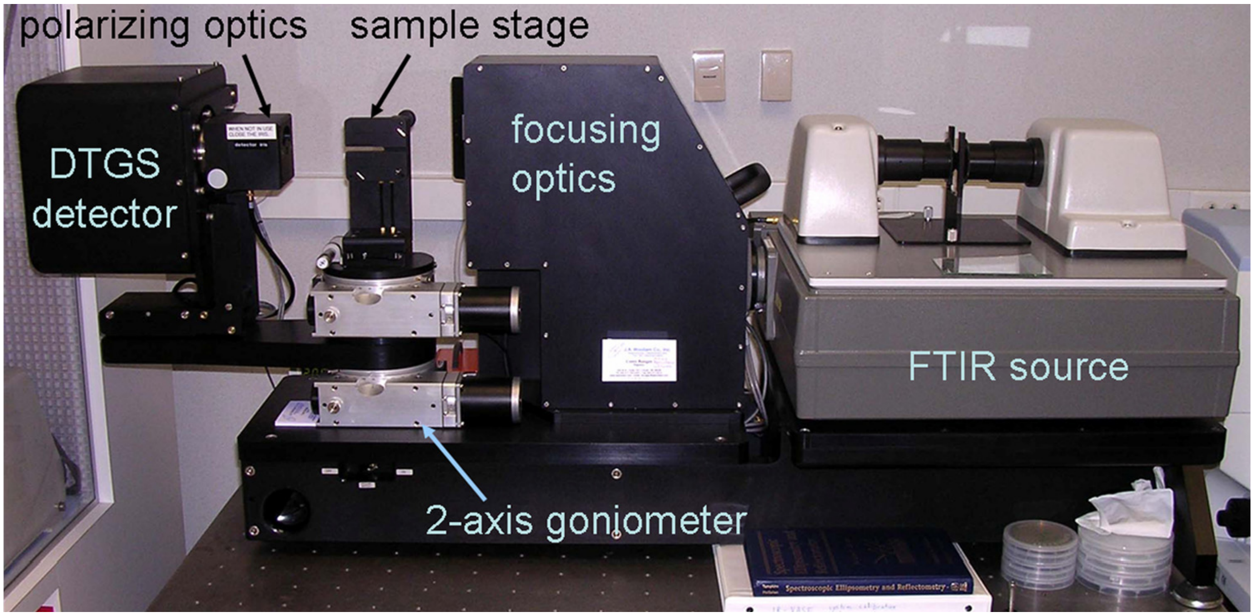

Figure 27 J.A. Wollam Co. IR-VASE thin film characterization system

4.2.1 Material Characterization Procedures

The following sections are dedicated to the presentation of the optical properties as they were measured and analyzed using Kramers-Krönig-consistent oscillators and the polarimetric parameters as measured on the IR-VASE. Before presenting the actual data and oscillator fits for the optical properties of the material data, the process for determining the optical constants will be presented.

When describing the interaction of light with matter there are generally two different approximations. The first concerns the interaction of the radiation with the inner bound electrons of the atom and their motion about the nucleus, generally considered a bound-charge interaction. The other deals with electrons that are essentially free of any binding potentials, generally considered a free-charge interaction. These two descriptions of light-matter interaction work well for most situations when the electron is the primary particle interacting with the radiation. The primary exception to these interactions includes semiconductors where a more quantum mechanical approach is necessary due to the periodic potentials induced by the order and inter-atomic interaction of the atoms in the crystal lattice. For lower frequency excitation, the radiation interacts primarily with polar molecular vibration and rotational modes (gases). When the light couples to phonon modes in the lattices of ionic or partially ionic compounds this leads to resstrahlen bands of reflection. The method by which the ellipsometry analysis relates the measured optical properties to actual material properties is to fit the measured curve with various oscillator models. These oscillator models are Kramers-Krönig consistent and can represent each of the interactions discussed above. The process for inferring the optical properties from the measured ellipsometric quantities is outlined below.

The general process for acquiring data is as follows:

1. Load sample on to goniometer stage
2. Follow alignment procedure to ensure that the sample is flat and its thickness accounted for in the following measurements
3. Open IRVASE scan settings window (shown below in Figure 28)

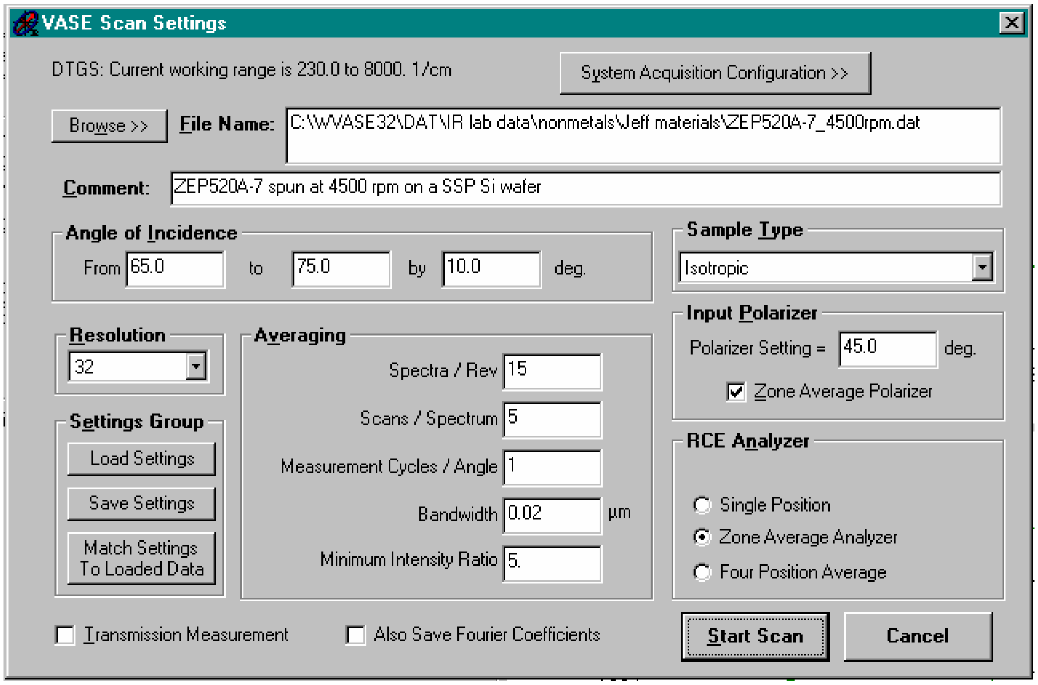

DTGS: Current working range is 230.0 to 8000. 1/cm

File Name: C:\WVASE32\DAT\IR lab data\nonmetals\Jeff materials\ZEP520A-7_4500rpm.dat

Comment: ZEP520A-7 spun at 4500 rpm on a SSP Si wafer

Angle of Incidence
From 65.0 to 75.0 by 10.0 deg.

Sample Type
Isotropic

Input Polarizer
Polarizer Setting = 45.0 deg.
☑ Zone Average Polarizer

Resolution
32

Averaging
Spectra / Rev 15
Scans / Spectrum 5
Measurement Cycles / Angle 1
Bandwidth 0.02 µm
Minimum Intensity Ratio 5.

Settings Group

RCE Analyzer
○ Single Position
● Zone Average Analyzer
○ Four Position Average

☐ Transmission Measurement
☐ Also Save Fourier Coefficients

Figure 28 Scan settings window for the IRVASE data acquisition

4. Set the file path for saving the data and write comments concerning the details of the sample preparation or fabrication steps (comments are saved with the data)
5. Set the desired angles of incidence. For best results choose a central angle that is near the Brewster angle for dielectrics or the principal angle for metals with other angles on the high and low side of this angle
6. Set the desired resolution for the data in units of cm^{-1} (1, 4, 16, 32, 64, or 128)
7. Set the desired averaging parameters. The parameters shown in Figure 28 are for quick data acquisition as the unknown quantity was thickness and the optical properties were already known for this particular material.

Once the data set is acquired, it will be represented as spectral variations in α and δ, which are defined in Equation 3. The variations will look like those shown in Figure 29. In this figure the multiple angle data is seen along with a typical thin film spectrum. The large contrast variation in α and δ is due to the interference effect in the thin film and is shown in circle I and circle III of Figure 29. As the film becomes thicker, the number of these interference peaks will increase and as such, the number of peaks is a good indicator of thickness. If Figure 29 was plotted as a function of frequency rather than wavelength, it would be observed that α and δ would be periodic due to the Fabry-Perot etalon effect of the thin film sandwiched between air and the Si substrate. The details in the α and δ spectrum are also affected by the optical properties of the material. This can be seen in the α and δ spectrum in Figure 29 in circles I, II, and III. Circle I shows the different heights of the peaks for the different angles of incidence. Due to the optical path length, the higher the refractive index the higher the peak will be for a given angle of incidence. Also noted in circle I, as the angle increases from normal, the peak decreases and this is due to the decrease in the film phase thickness by the cosine of the incidence angle.

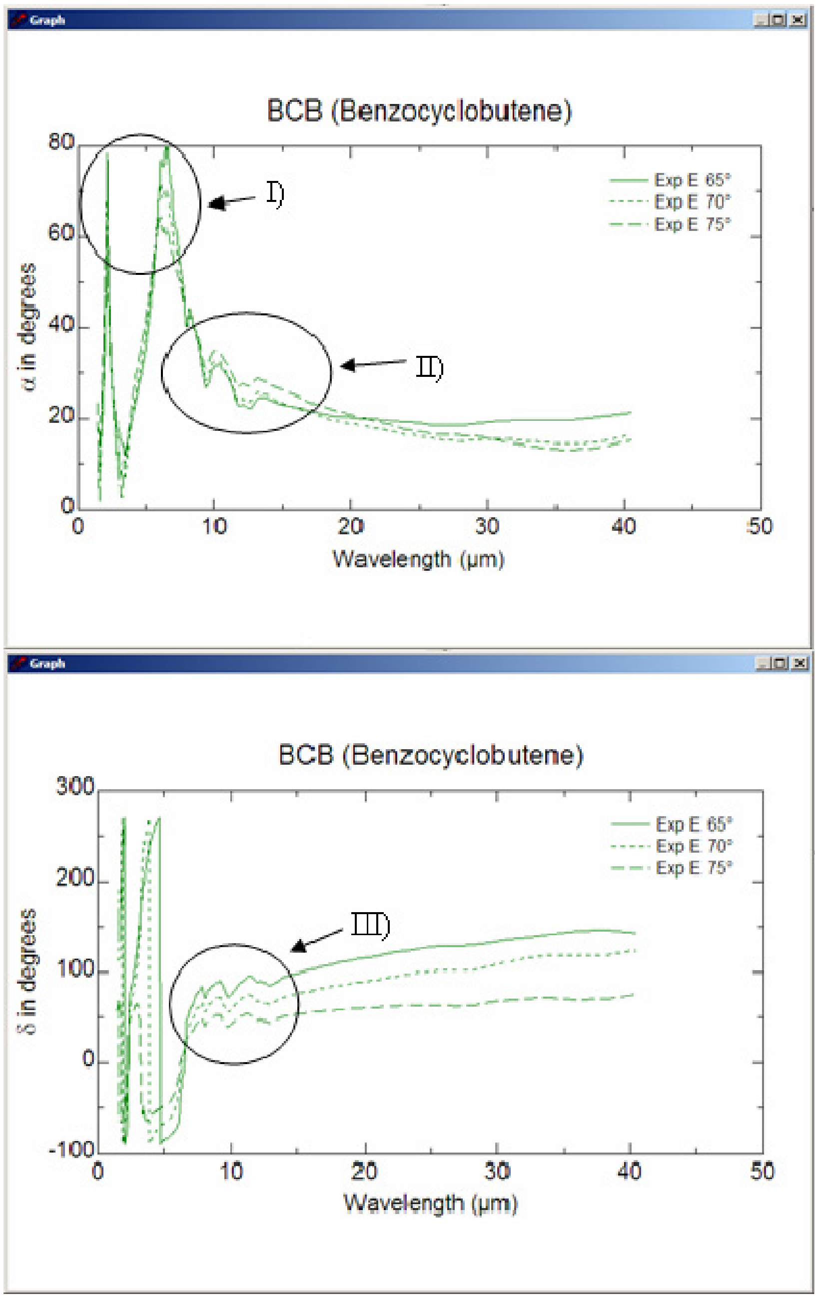

Figure 29 Example snapshot showing the multiple angle data acquired for BCB in IRVASE

Circles II and III show other characteristic examples in the spectrum which are representative of spectral attenuation. These smaller oscillations are not periodic but are spectral regions of optical resonance and will be represented in the model as Kramers-Krönig-consistent oscillators.

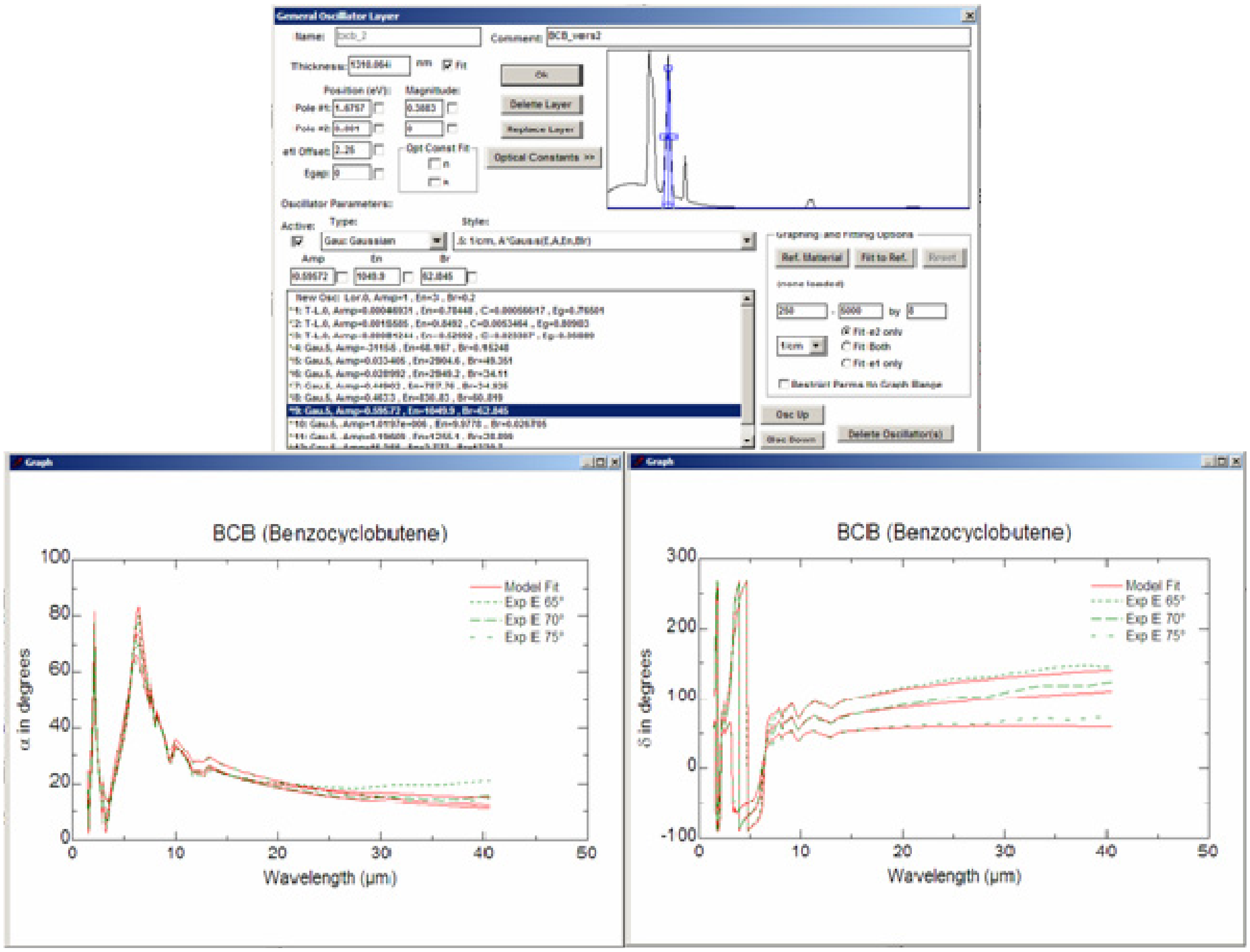

Figure 30 Screenshot of general oscillator model and its corresponding measured (dashed line) and modeled (solid line) α and δ spectra

Once the data is acquired it must be analyzed so that a physically realizable model can be determined. The goal of the model is to determine the optical constants as a sum of oscillators with varying mathematical forms including Gaussian and Lorentzian oscillators. Once a model is built, the α and δ spectra can be generated using the general oscillator parameters. The ultimate goal is to minimize the mean-squared-error (MSE) between the measured spectra and the modeled spectra. The oscillator model is shown in the top of Figure 30 depicting the many oscillators that it takes to represent the material. For the case of BCB, 12 oscillators were used.

The bottom two plots show the measured data (dotted line) and the modeled data (solid line) plotted on top of one another. It is seen that the model sufficiently described BCB up to a wavelength of about 20 μm before diverging from the measured data. From the oscillator model, reliable optical properties that maintain Kramers-Krönig consistency can be determined.

Before the oscillator model is built, it is desirable to already have an initial estimate of the material properties to reduce the time necessary to build a model. An example is knowledge of whether the material is a metal, dielectric, or semiconductor. Another parameter that is useful to have in this context is an approximate thickness for thin film measurements. There are some trends that the spectra will have depending on the fundamental properties of the film. Dielectric thin films will have the characteristic interference oscillations in the α and δ spectrum while bulk dielectrics will not have the interference fringes. A bulk dielectric and a thin film of the same dielectric will have the same optical properties as measured using ellipsometry. This is due to the lack of multiple reflections since there is no dielectric stack. Highly conductive metals tend to have a flat α and δ spectrum with $\alpha(\lambda)$ flat at 45° and $\delta(\lambda)$ flat at 180°. For lossy metals, both α and δ will decrease from these values.

4.3 Infrared Characteristics of Materials Used

4.3.1 a-SiO_2: Fused Silica

In order to have the meanderline function in the MWIR, it was necessary to find a substrate that would allow for high transmission in this band. Fused silica is an amorphous form of the compound, SiO_2. The crystalline form, quartz, was undesirable for the meanderline applications because of its material birefringence. The amorphous form is typically heated to destroy the crystalline order, and also has a very high purity that leads to higher transmission in the MWIR.

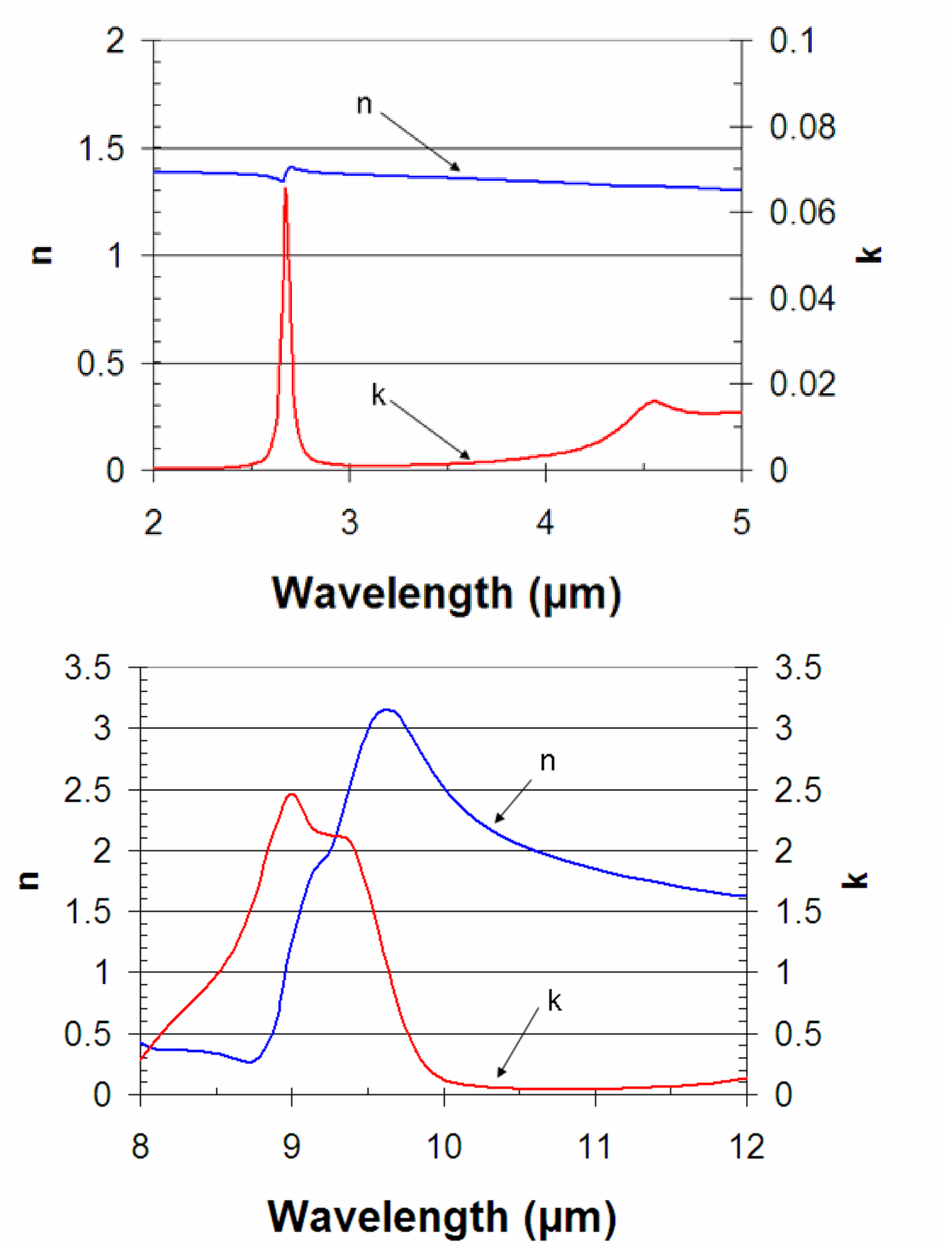

Figure 31 Measured optical properties of the fused silica wafer as measured for (top) the wavelength range of 2 – 5 µm which includes the MWIR and (bottom) wavelength range of 8 – 12 µm corresponding to the LWIR

The physical dimensions of the fused silica wafer used for the fabrication of the MWIR meanderline retarders were a diameter of 100 mm and a thickness of 500 µm. The optical properties of the fused silica wafer are shown in Figure 31 for both the MWIR and the LWIR. The optical properties are represented in terms of *n* and *k*, the real and imaginary part of the complex refractive index. It is observed that the refractive index is fairly flat in the spectral range of 2-5 µm. The optical attenuations between 2 and 5 µm are caused by the flame induced high temperatures required to convert quartz into amorphous silica and the combination of hydrocarbons and oxygen for combustion. These impurities can form into hydroxyl [31] and water in the wafer which increases attenuation in the MWIR. A transmission spectrum was also measured using Fourier transform infrared (FTIR) spectroscopy. The measured spectrum is shown in Figure 32.

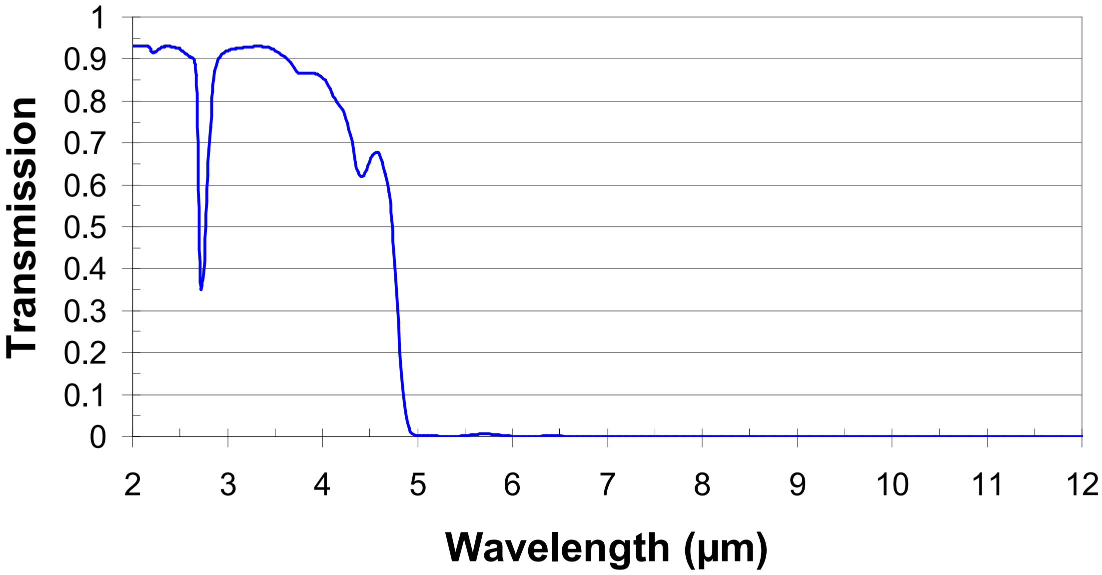

Figure 32 Measured transmission of a fused silica wafer with a thickness of 500 µm from 2-12 µm.

The high attenuation in the transmission spectrum of Figure 32 between 2 and 5 μm is due to water and hydroxyl. The water is sparsely distributed within the fused silica as is seen by noting the small magnitude of *k* in the MWIR seen in Figure 31 (top) as compared to the very large magnitudes of *k* observed in the LWIR. The large *k* values in the LWIR are caused by the strong molecular vibrational resonances of the SiO_2. The magnitudes of *k* in the MWIR were so small that there was no observable perturbing effect on *n* as compared to the LWIR where strong perturbations existed in *n*.

4.3.2 High-ρ Si: High Resistivity Silicon

For the initial efforts for a meanderline retarder in the LWIR, the substrate of choice was high-resitivity silicon. The resistivity of the silicon wafers used was specified at 4-6 kΩ-cm. These silicon wafers were desired due to their purity as signified by the high resistivity and their transparency in the LWIR. The resistivity was high enough to prevent the electrical shorting of the meanderline structures. The physical dimensions of the wafers were a diameter of 76.2 mm and a thickness of 380 μm.

The IR properties of this grade of silicon were desirable, and the LWIR band was free from absorption artifacts. The primary disadvantage to the optical properties of silicon is the high dielectric constant. The average relative permittivity, $\varepsilon_r \sim 11.7$, will lead to a mismatch in the characteristic impedance of air and silicon, which will have to be accounted for in the design of the meanderlines. To determine the optical properties of the silicon, a wafer was characterized and the measured optical properties are shown in Figure 33 in terms of *n* and *k*.

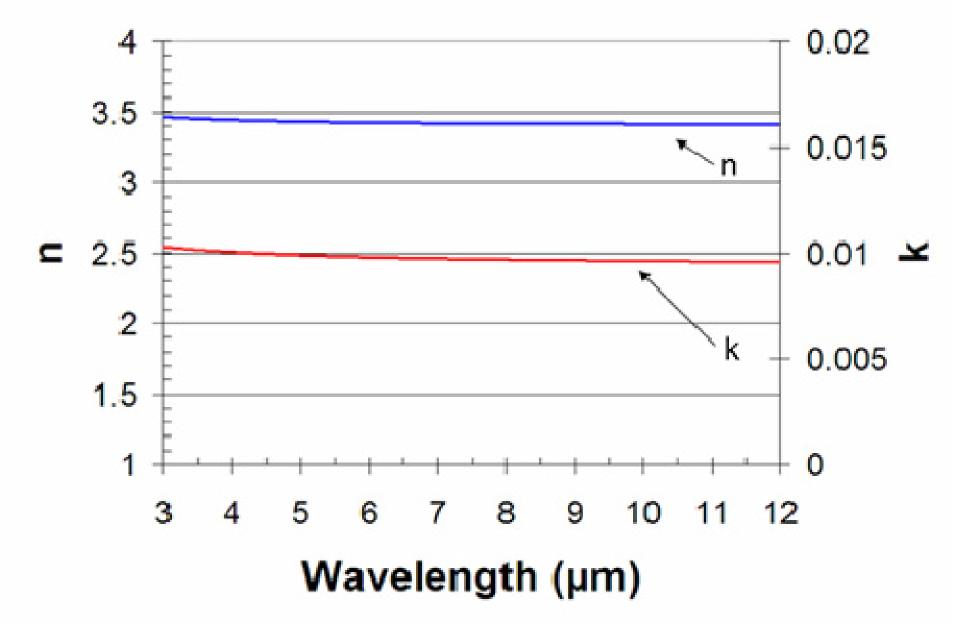

Figure 33 Measured optical properties for high-resistivity Si wafer

From the optical properties for high-resistivity silicon in Figure 33, it is expected that the transmission will indeed be limited by the reflections. To confirm this expected large reflection loss, a transmission spectrum was also measured to determine the best case transmission through the high-resistivity silicon wafer.

The transmission spectrum in Figure 34 shows the spectrally flat transmission trend. This flatness is indicative of the absence of strong material attenuations as was expected by observing the relative flatness of the extinction coefficient in Figure 33. The overall integrated transmission is 55% for almost the entire band which corresponds to the computed Fresnel reflections from the refractive index as measured in Figure 33. The minor fluctuations in the spectral vicinity of 6 µm are noise artifacts arising from the electronic signal processing in the FTIR instrument to compensate for the effects of atmospheric absorption in that spectral range.

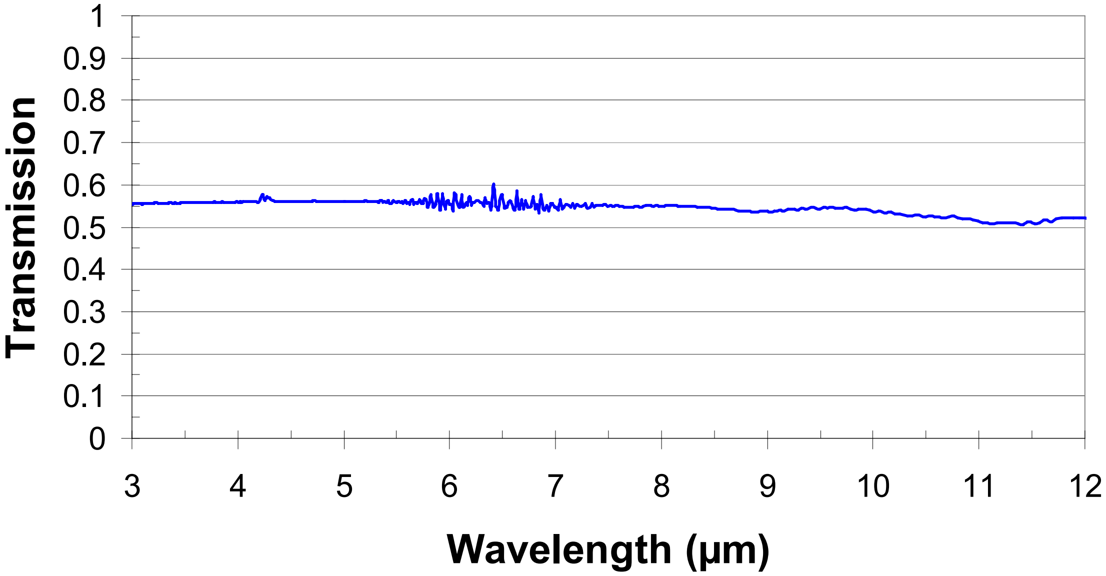

Figure 34 Measured transmission of a high-resistivity silicon wafer with a thickness of 380 µm from 3-12 µm. The fluctuations around 6µm are noise in the measurement.

4.3.3 BaF_2: Barium Fluoride

The final substrate material investigated and used for the fabrication of the meanderline retarders was barium fluoride. Barium fluoride is commonly used as IR windows and has a typical transmission range from UV to about 12 µm. The primary interest in barium fluoride is the fact that it could be used as a substrate for both of the IR bands, MWIR and LWIR. The measured transmission of the BaF_2 wafer that was used for fabrication is shown in Figure 35.

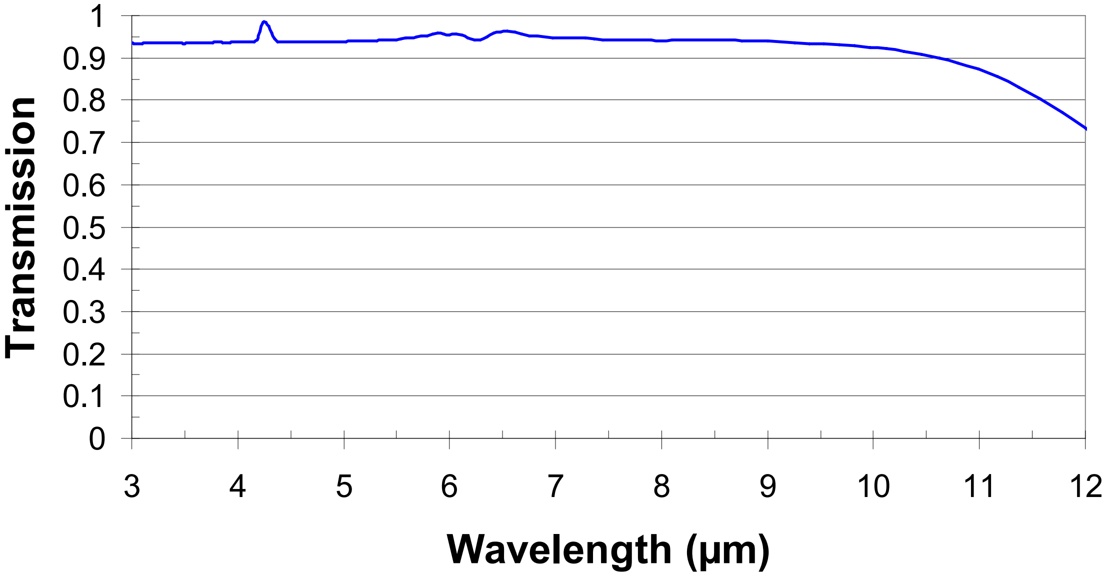

Figure 35 Measured transmission of a Barium Fluoride wafer with a thickness of 3.18 mm from 3-12 µm

The BaF_2 wafer was measured using ellipsometry and the optical properties are shown in Figure 36. The refractive index of the BaF_2 as measured agrees well to the tabulated values found in Reference [34]. The average value of *n* was about 1.39 for the MWIR and 1.35 for the LWIR.

The physical properties of BaF_2 are varied and not well documented in a single source. The main difficulties with using BaF_2 are its susceptibility to both thermal and physical shock. Empirical experiments have shown that the primary difficulty is in cooling the BaF_2. An example would be the fact that the BaF_2 survived placement onto a hotplate at 180°C, but when it was attempted to remove the wafer from the hotplate using tweezers, the wafer cracked into several pieces. Therefore the heating of the BaF_2 is a stable process, however it was necessary to allow the wafer to cool to room temperature over a period of 35 minutes which equates to a cool down rate of 4°C/minute. The mechanical shock properties did not seem to be any more apparent that other materials used and normal precautions were satisfactory to prevent the breaking of the wafers.

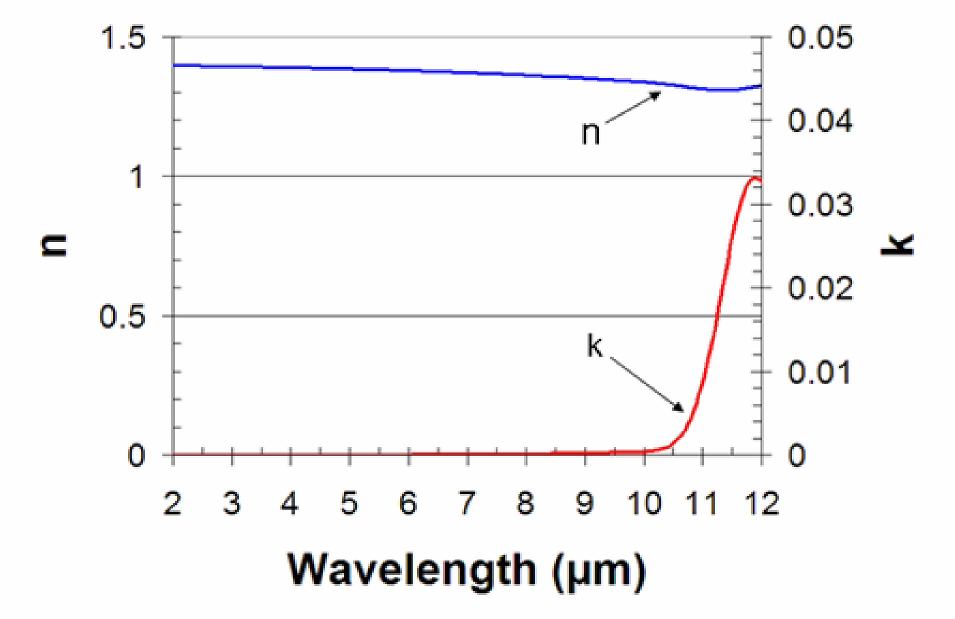

Figure 36 Measured optical properties of the BaF_2 wafer

Another special precaution to be noted in the use of the BaF_2 wafers is its susceptibility for chemical attack by both acidic and alkaline solutions. These properties were discovered during the investigations for the removal of thin metal films over the resist on the substrate. Specifically, the Ni etch solution which was nitric-acid based and the Au etch solution which was a potasium iodide solution, both attacked the BaF_2 by ruining the surface quality of the wafer. The method by which the use of these chemicals was avoided is described in Section 3.1.2.3.

4.3.4 BCB: Benzocyclobutene

For the capability to fabricate multiple layers of meanderlines, it was necessary to find a material that had desirable optical properties, could be deposited with varying thicknesses, and would adhere to the substrates. The material that was used for this task was a spin-on dielectric from Dow chemical company, CYCLOTENE 3022-35, a benzocyclobutene (BCB) polymer. Since BCB can be spun onto a wafer, the thickness can be controlled by the spin speed. The solvent for BCB, mesitylene, was used to dilute the BCB to allow for even thinner layers to be applied.

The optical properties of BCB, after curing, were measured over the wavelengths from 3 to 12 µm for integration into the electromagnetic models. To measure the optical properties, a thickness of 1.3 µm of undiluted BCB was spun onto silicon wafer with a roughened back (to reduce back reflections). The dilution of the BCB is not expected to vary the optical properties of the BCB since the solvent is baked away during the curing of the BCB. The optical properties of BCB are shown in Figure 37.

It is noted in Figure 37 that BCB has many optical resonances over this spectral range. The BCB seems ideal for use in the MWIR as there is only one resonance observed and its strength is small. In the LWIR there seems to be several resonances that could be of concern for the use of this material for transmission applications. To have a better idea of the possible transparency of the BCB in the LWIR, the extinction coefficient was used to determine the spectral attenuation for varying thicknesses of the BCB. This information was plotted in Figure 38 as a computed spectral transmission plot that excludes the surface Fresnel reflections and accounts only for material attenuation.

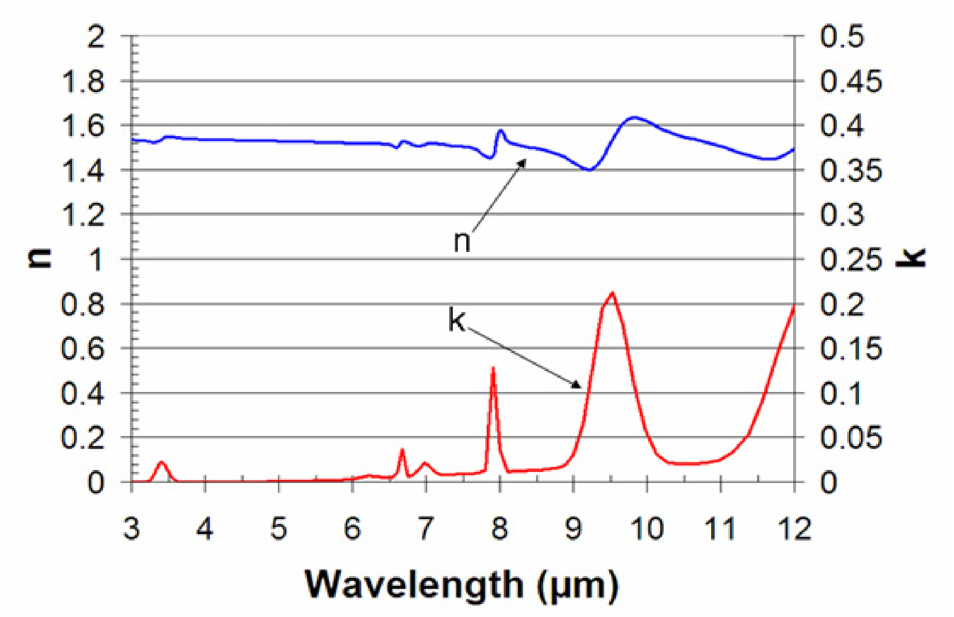

Figure 37 Measured optical properties for Benzocyclobutene (BCB)

From the transmission plots of Figure 38, it appears that the BCB can be utilized even in the LWIR, as long as the layer thicknesses remain small. For the LWIR, a quarter-wave separation layer at a mean wavelength of 10 µm corresponds to a BCB thickness of 1.6 µm. At this thickness the integrated LWIR transmission drops to about 85% due the relatively strong attenuations at 9.53 and 12.29 µm. However, this reduction is tolerable since it is the only available material that has been found that can both be optically transmissive and survive the multiple fabrication processes. Most other materials have many strong attenuations due to complex molecular structure, organic and inorganic, and the associated allowed vibrational modes of oscillation.

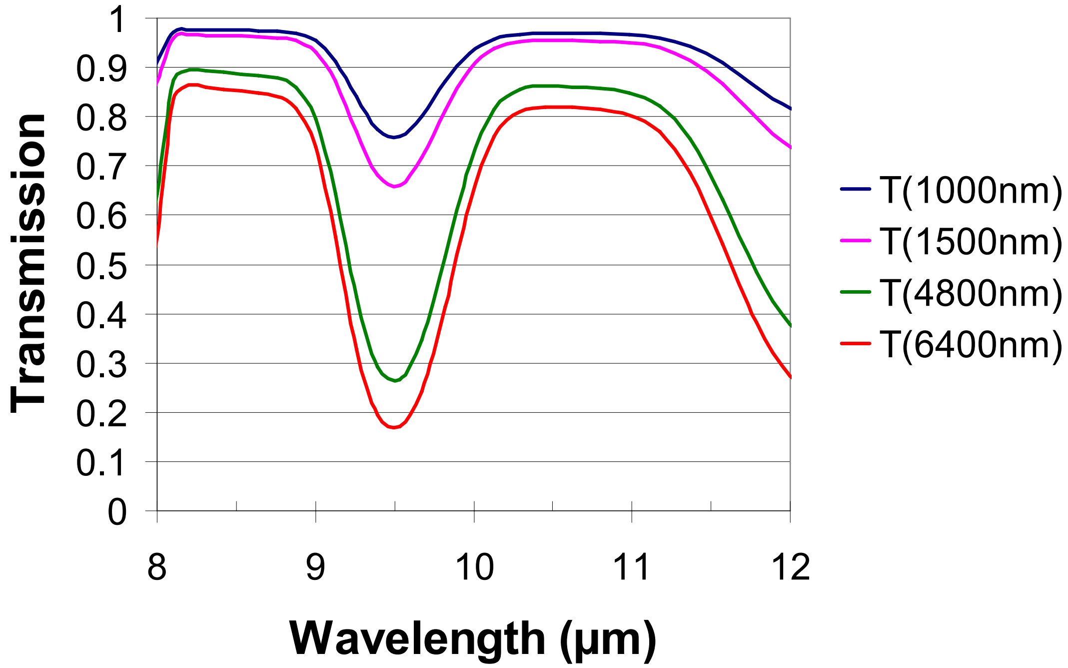

Figure 38 Transmission plots for varying thicknesses of BCB computed using the extinction coefficient from the measured optical properties

As important as the optical properties of BCB, for the success of the multiple layer meanderline, the chemical and physical properties of BCB are important as well. The fabrication process, utlizing e-beam lithography, requires relatively high temperatures and submersion in various organic solvents. Cured BCB is highly resilient to organic solvents and has been observed to resist the following organic solvents: methylene chloride, acetone, isopropyl alcohol (IPA), and xylene (ZEP RD). Thermally, BCB is also very resilient. During processing, the BCB is cured at a temperature of 250 °C while the remaining fabrication-process temperatures never exceed 180 °C.

BCB was characterized carefully for thickness since the standoff layer thickness is an important factor in the meanderline design. Specifically, for use in the MWIR as a standoff layer it was necessary to reduce the thickness of BCB to 600 nm and in the LWIR, 150 nm was needed to planarize the silicon standoff layers. The undiluted BCB, as purchased, has a spin chart represented in Figure 39, for the least viscous BCB available from the manufacturer at the time of purchase. The thinnest that it could be spun was 1 μm at a spin speed of 5000 rpm. Therefore it was necessary to dilute the BCB and determine a dilution ratio and spin-speed recipe that would give the desired thicknesses. To achieve a BCB thickness of 150 nm, the BCB was diluted, by weight, to a ratio of 3:1 BCB:mesitylene and spun at a spin speed of 2000 rpm. To achieve a thickness of 285 nm the BCB was diluted to a ratio of 10:15 BCB:mesitylene and spun at a speed of 3000 rpm, and this was done twice to get the desired standoff thickness of 570 nm for the MWIR double layer meanderline design on fused silica.

Another advantage for BCB during fabrication is that once BCB has been thermally cured, another layer can be spun on without intermixing with the layer beneath. In this way, several layers can be applied and as long as each layer is cured, the total thickness will be the sum of the individual layers.

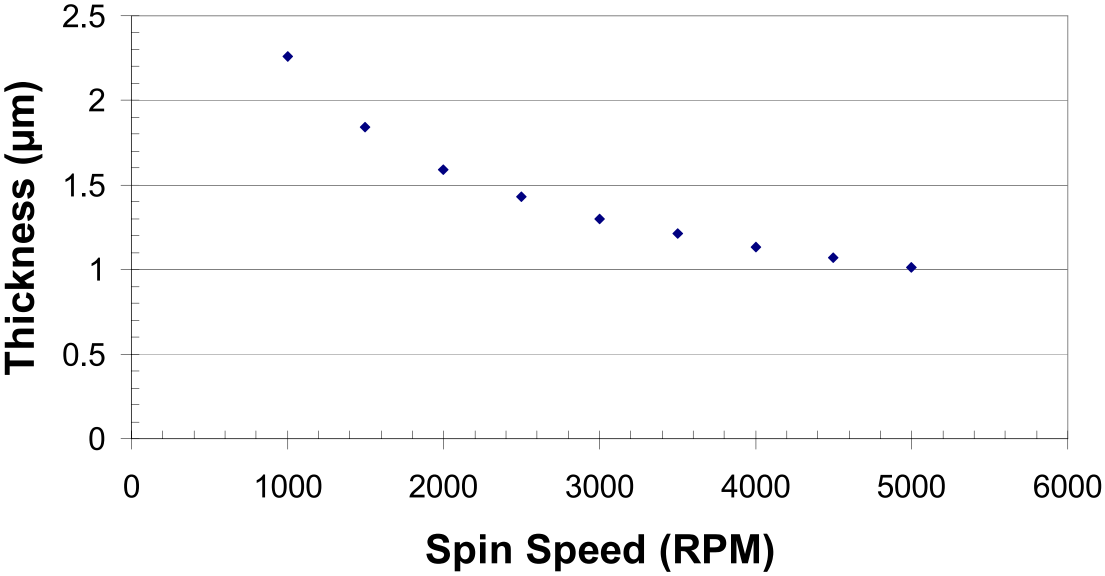

Figure 39 Manufacturer's Spin chart for undiluted CYCLOTENE 3022-35

4.3.5 Metals

The metals used in this research were ellipsometrically characterized and the data was made available in Reference [23]. The metals used in this research included: gold, titanium, and aluminum. Titanium was solely used as an adhesion layer for the gold.

CHAPTER V
MODELED AND MEASURED RESULTS

There were seven meanderline designs fabricated for this research. Design #1 was the initial proof-of-concept meanderline that was to demonstrate that the structure would behave in a similar fashion as observed in the RF. The proof-of-concept structure also was the first attempt to fabricate a meanderline retarder in the IR. The proof-of-concept meanderline was a single-layer design fabricated on silicon and was not designed to operate as a quarter-wave retarder, however it did show favorable spectral trends in the phase delay. Design #2 was a meanderline that was fabricated to operate as a quarter-wave retarder with a phase delay of 90° over the LWIR band. This structure was fabricated and extensively characterized both spectrally and for angle-of-incidence performance as it showed good polarimetric performance. The next two meanderlines (design #3 and design #4) designed and fabricated were used to investigate the benefits and problems that are encountered by using multiple layers to improve the performance. The final meanderline structure fabricated to operate in the LWIR, design #5, was designed using a substrate with low permittivity, BaF_2, to demonstrate the improvements over using high permittivity substrates for the meanderlines. The last structure, design #6, was fabricated to demonstrate that the concept of anisotropic impedance was not limited in geometry to a meanderline design. The structure had a zig-zag pattern and was characterized for its performance.

Design #7 allowed investigation of the meanderline concept, moving the band of operation to the MWIR, to show that the structure can be designed to extend its function to other bands in the IR. This design takes what was learned from the previous designs in the LWIR and demonstrates a multiple-layer meanderline that functions over the MWIR as a quarter-wave retarder. This structure was fabricated and characterized both spectrally and for angle-of-incidence performance as it showed good polarimetric performance.

The last section in this chapter demonstrates the measured performance of the single-layer meanderline, design #2, as it is operated in reflection. This characterization correlates the measured data to both numerically modeled data and the performance as would be predicted by the Smith chart. The discussion also extends to show the limitations of using meanderline retarders in reflection.

5.1 LWIR (8-12 μm) Meanderline Retarders

The first band investigated for using meanderline retarders was the LWIR. This spectral region is a region of atmospheric transparency and offers applications once functional meanderline retarders are demonstrated. There were two paths forward on the material design of the meanderline retarders in this band. The initial modeling and fabrication were done for meanderlines composed of gold and on a silicon substrate. These material choices, though not necessarily ideal due to the high permittivity of the silicon in this band (~11.7), were made due to pre-existing fabrication techniques on silicon. Our initial efforts in the fabrication and characterization of meanderline retarders were to fabricate and model a proof-of-concept design that demonstrated the feasibility of using the meanderline concept at such high frequencies.

5.1.1 Design #1: Single-Layer Proof-of-Concept Meanderline on Si

Design #1 used geometric parameters that would demonstrate the possibility of a broadband phase delay. This proof-of-concept design was to demonstrate a degree of correlation between the modeled and measured performance parameters. The design parameters for the meanderline structure were: $w = 0.4$ µm, $pw = 1.0$ µm, $ph = 1.0$ µm, and $dx = 2.3$ µm. The Au was deposited to a thickness of 100 nm as a starting point. An SEM image of the fabricated structure is shown in Figure 40.

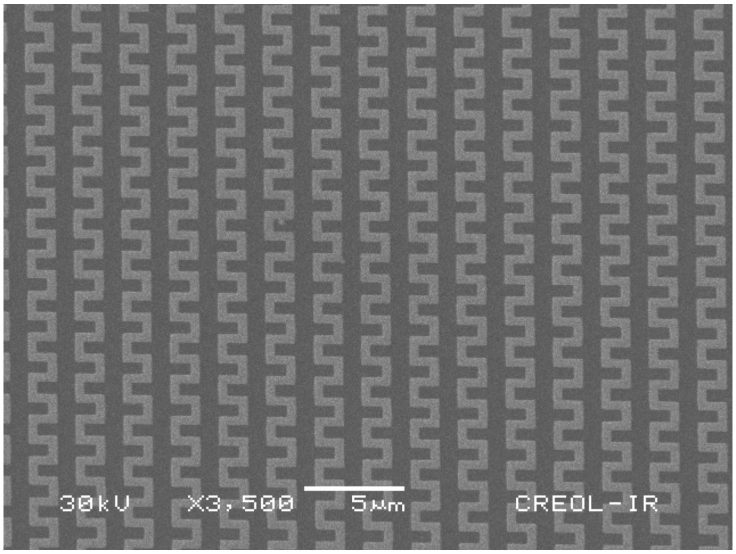

Figure 40 SEM image of the proof-of-concept Au meanderline structure on a Si substrate

After imaging the meanderline structure, measurements were made for all of the geometric parameters to check the dimensional fidelity between the designed structure and the fabricated structure. The width was the only parameter of prime concern because it is the parameter that is the most difficult to fabricate exactly. The other parameters are independent of e-beam resist exposure doses, and are functionally independent of the width of the meanderline. The measured width of the fabricated meanderline was 500 nm. The model was then re-run to accommodate the as-is fabricated thickness and the comparison between the modeled and measured data. This data is shown in Figure 41. The empirically determined sheet resistance for this structure was found to be 7.25 Ω/□.

The modeled and measured values for the performance of the proof-of-concept meanderline design show good correlation. From Figure 41, it is seen that the meanderline design as fabricated has an average transmission of about 30%. The power budget calculation for this structure included a measured dielectric reflection loss, R_{sub}, of 45%. The reflection loss of the meanderlines with a phase delay of 60°, R_{meander}, is expected to be 24% as calculated on the Smith chart. Therefore the transmission predicted was 42% before accounting for any metal losses. Using the measured transmission of 30% and with the loss mechanisms mentioned into Equation 34, the ohmic loss of the metal, A_{metal}, was calculated to be 28%.

Though the phase delay induced by the structure was not spectrally flat, it certainly showed the potential for a broadband phase delay. The modeled and measured spectral phase delay correlates well on the average. The spectral trends also agree fairly well. The measured phase delay does not flatten off spectrally as soon as the modeled data, but it does flatten. This data shows the feasibility of a broadband meanderline retarder. The good polarization performance can be observed by looking at the modeled and measured axial ratio. The axial ratio of the transmitted radiation shows good spectral performance as it is fairly flat after a wavelength of 10 μm. The relatively low transmission was an expected result of the large impedance mismatch of the meanderline/Si interface with air along with the ohmic losses associated with the Au.

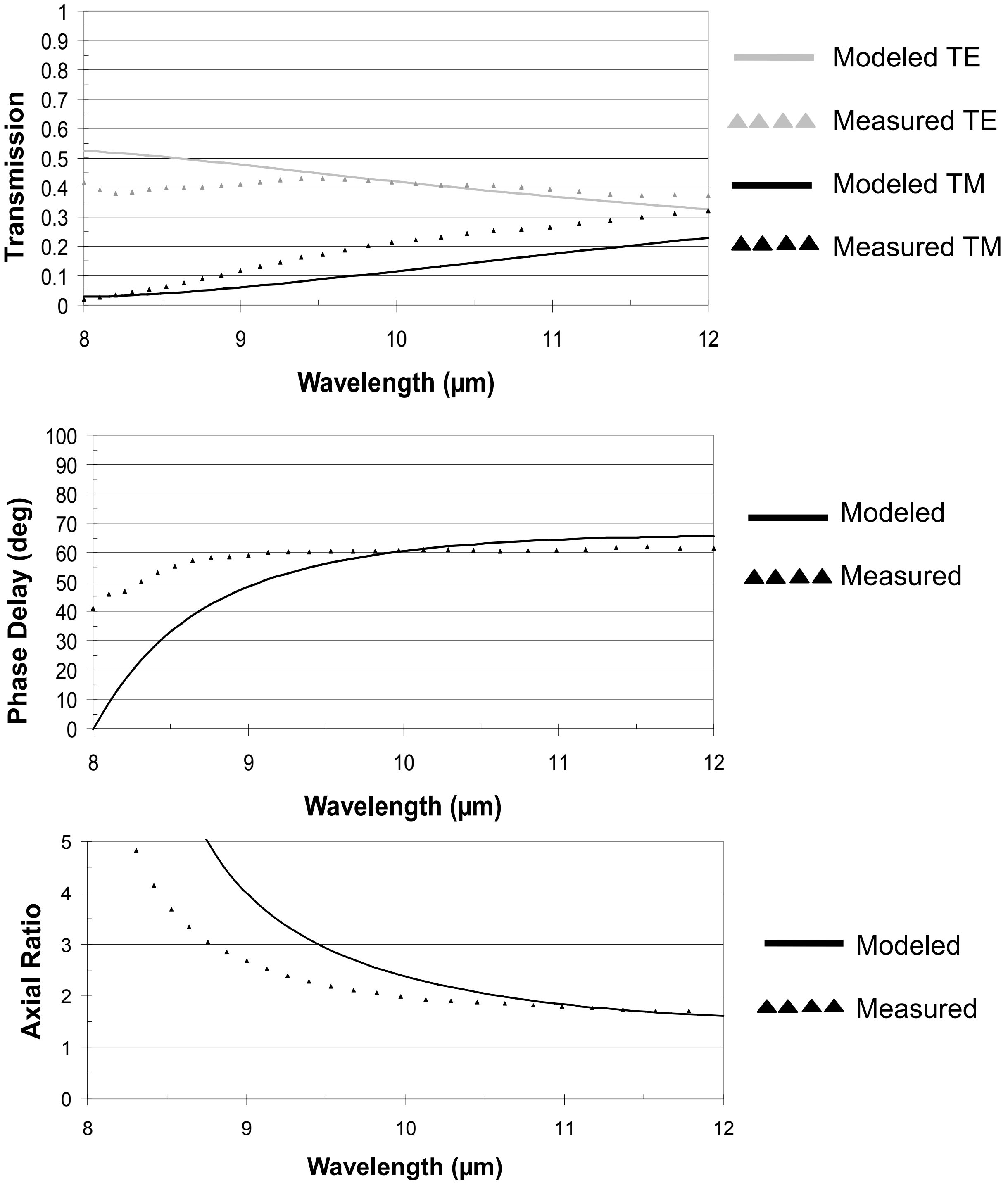

Figure 41 Plots showing the modeled and measured performance of the proof-of-concept meanderline design

5.1.2 Design #2: Single-Layer 90° Meanderline Retarder on Si

The first attempt at designing a meanderline retarder to operate at a phase delay of 90° was done using silicon as the substrate for the LWIR. This was done for the same reason as the proof-of-concept design, relative simplicity in the fabrication processes. The same issues were present concerning the high reflection losses due to the high permittivity of the silicon. The same value for the sheet resistance was used as for the proof-of-concept design with a value of 7.25 Ω/□.

Before modeling the single-layer meanderline line retarder to operate at 90°, design #2, the ideal transmission performance was estimated using the transmission equations in Section 1.4.1. In the IR, the impedance relation in Equation 9 simplifies to

$$Z = \frac{1}{n}\sqrt{\frac{\mu_0}{\varepsilon_0}} \qquad \text{Equation 45}$$

Z is given as a function of *n*, the refractive index, with the assumption that the relative permeability goes to 1 in the IR allowing $n = \sqrt{\varepsilon_r}$. Since air has characteristic impedance that is essentially equal to the impedance of free space, the normalized admittance of the silicon/air interface simplifies to

$$y_{Si/air} = \frac{1}{n_{Si}} \qquad \text{Equation 46}$$

If the meanderline is assumed lossless then Equation 19 reduces to

$$y_L = \chi - i\gamma = \frac{1}{n_{Si}} - i\gamma \qquad \text{Equation 47}$$

Now if Equation 22 is solved for the magnitude of the reflection using Equation 24, the magnitude of the reflection coefficient is calculated to be $|\Gamma_h| = 0.803$. The transmitted power is given by

$$T = 1 - |\Gamma|^2 \qquad \text{Equation 48}$$

Solving Equation 48 gives a total power transmission of 35.5% for an ideal lossless meanderline retarder on an infinite silicon substrate. However, since the single layer meanderline retarders are not measured on an infinite silicon substrate, the reflections of the second boundary on the back of the wafer reduce the ideal power transmitted to 25.1%. This value is important as it sets the ideal transmission with for a meanderline with no ohmic loss. A transmission value lower than 25.1% is caused by the loss in the metal since the substrate is essentially lossless.

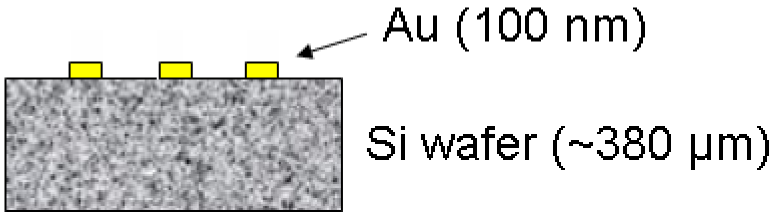

Figure 42 Cross-section of the single-layer 90° meanderline retarder

The design process for the 90° meanderline retarder was to use the trends discussed in Section 2.1.3 to modify the proof-of-concept design to accommodate the larger phase delay. A schematic of the cross-section of the structure is shown in Figure 42 The first modification was to increase the relative phase delay to see if it was feasible to achieve a 90° phase delay using a single layer. There were two potential approaches for increasing the phase delay: increase the *w* and/or decrease *dx*. To increase the phase delay to the desired value it was necessary to decrease the periodicity to 1.45 µm and increase the width to 0.6 µm. The final design parameters for the single-layer meanderline retarder were: $w = 0.6$ µm, $pw = 0.95$ µm, $ph = 0.8$ µm, and $dx = 1.45$ µm. Unfortunately, this leaves very little space between the actual geometries as observed in the SEM image in Figure 43. The gap separation between the meanderlines is simply the sum of the *ph* and *w* subtracted from *dx*. For this design the expected gap was 150 nm, which is a very small region that is not to be exposed. To achieve this resolution it was necessary to thin the ZEP520A-7 resist to a thickness of approximately 250 nm. The characterization of this process is shown in Section 3.1.2.1.

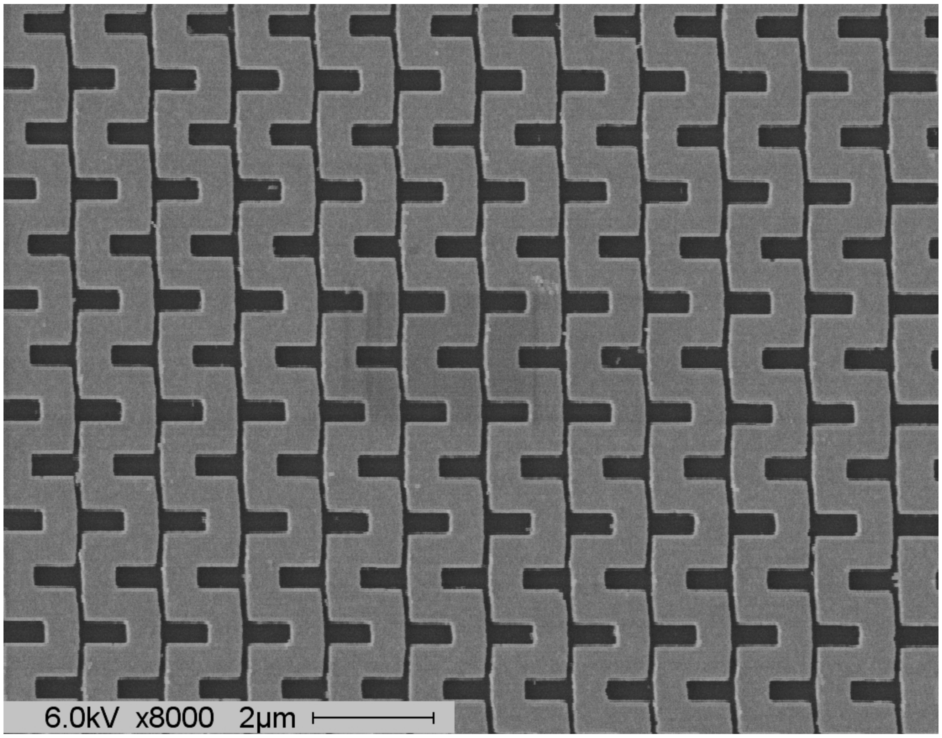

Figure 43 SEM image of the single layer meanderline designed to have a 90° retardance.

To achieve this design width, the pattern file with was 0.5 µm with the expectation of overexposure by about 50 nm on each side. This left little room for fabrication error since if the widths were too wide, the structures would overlap causing electrical shorting of the structure. A higher magnification of the structure is shown in Figure 44 to demonstrate the very close proximity of the structures to one another.

The actual measured linewidth of the fabricated structure was very good with a measured width of 600 nm. The measured separation between the meanderline structures was 155 nm. The thickness of the gold for the meanderline structure was 100 nm, which corresponds to about 10 skin depths at a wavelength of 10 µm. The modeled and measured results for this meanderline design are shown in Figure 45. The results shown show the magnitude of the relative phase delay to be spectrally broad over this band. The spectral trend seen in the phase delay is that the short wavelength phase delay cuts down to 60° while the long wavelength response levels off at about 100°.

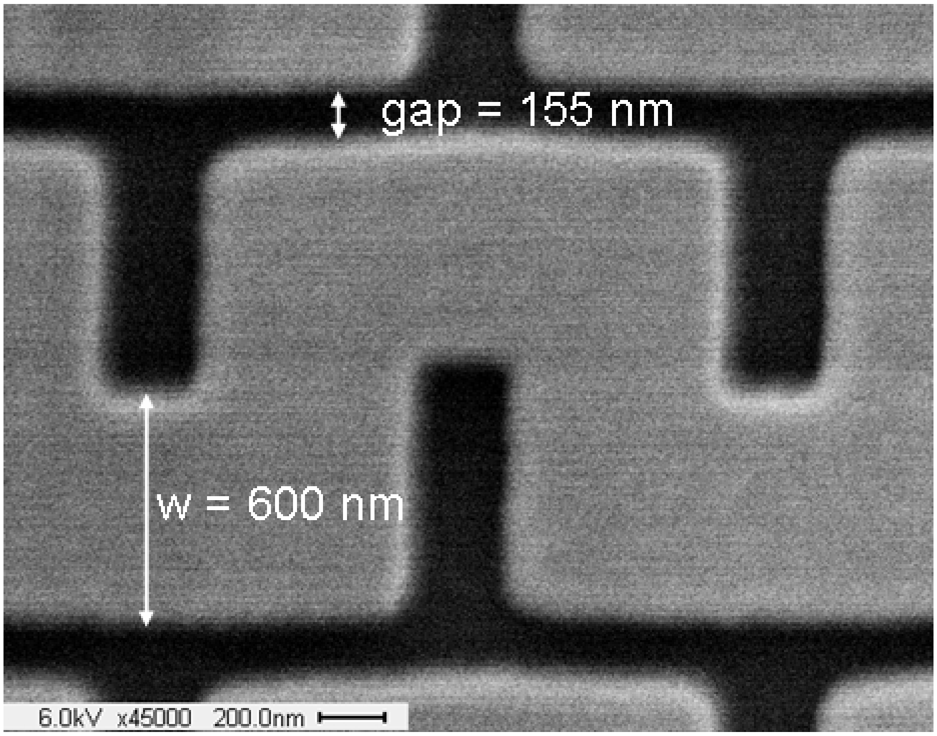

Figure 44 SEM image showing the measured width and gap of the fabricated meanderline structure

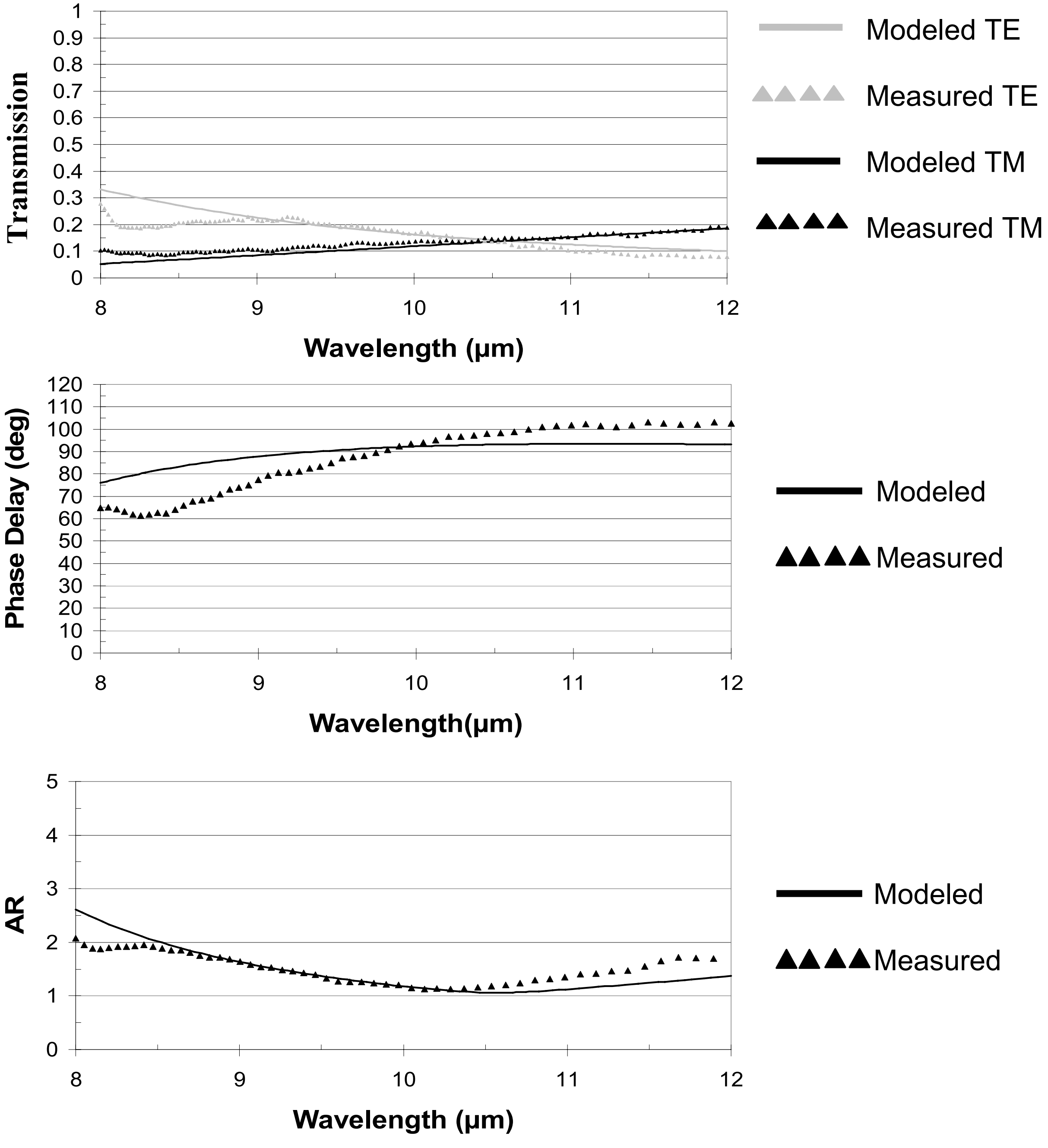

Figure 45 Plots showing the modeled and measured performance of the single-layer 90° retarder meanderline design on high-resistivity silicon at normal incidence

This spectral trend agrees well with the modeled data. The transmission plot in Figure 45 shows that the overall transmission follows the expectation for high reflections. The transmission plots also show that the value for the empirically determined sheet resistance represented the overall conductivity well. It is of note that to model this structure in PMM, it was necessary to treat the substrate as an infinite half space. Therefore the computed transmission coefficients were corrected in post processing to include the dielectric reflection from the back interface of the silicon wafer. The orthogonal transmission power coefficients have a spectral intersection at a wavelength of about 10.5 μm and this spectral intersection is also observed in the measured spectra. This intersection is useful since it is in this spectral region where the axial ratio is at its minimum assuming the phase delay remains around 90°.

The power budget analysis for this design included a double interface dielectric reflection, R_{sub}, of 45%. The silicon susbtrate is essentially lossless therefore A_{sub} is equal to zero. The reflection of the single-layer meanderline with a retarderance of 90°, R_{meander}, was expected to be 50%. The expected transmission using the metal loss value, $A_{\text{metal}} = 28\%$, that was measured for design #1 was 20%. Using Equation 34 for a power budget analysis and the measured transmission of about 15%, the calculated ohmic loss, A_{metal}, due to the gold meanderlines is 45%. The ohmic loss in the gold is measured to be 1.6 times larger than for the proof-of-concept design. This increased loss is expected because the quarter-wave meanderlines have a smaller period, 1.45 μm, compared to the period of the proof-of-concept design, 2.3 μm, and their width is also greater. Since the period was smaller for the quarter-wave meanderline, the meanderlines were more densely packed causing more electromagnetic interaction with the lossy metal.

It is also of note that the primary purpose was to demonstrate that a meanderline could be fabricated that could act as a quarter-wave retarder over the LWIR band. This structure demonstrates that the retardance can be made close to 90 degrees over most of the 8 – 12 µm range.

The performance discussed so far concerned normal incidence radiation. If the meanderline structure were to be used at either an off angle of incidence or in a fast F/# optical sytem, it would be relevant to know how well the meanderline structure performs over these angles. In this study, the IR-VASE was used to make the same measurements that were made at normal incidence for other angles of incidence ranging from 0° to 60°. The meanderline structure does not have bilateral symmetry as discussed in Section 1.4.3. Therefore it was necessary to model and measure the polarimetric parameters for off-angles of incidence for planes of incidence along $\alpha = 0°$ and 90°. The data for angles of incidence of 0°, 40°, and 60° are shown in Figure 46 and Figure 47 for $\alpha = 0°$ and $\alpha = 90°$. These angles were chosen because the meanderline showed little variations up to 40° and the overall trends were more obvious by presenting these three angles along both planes of symmetry.

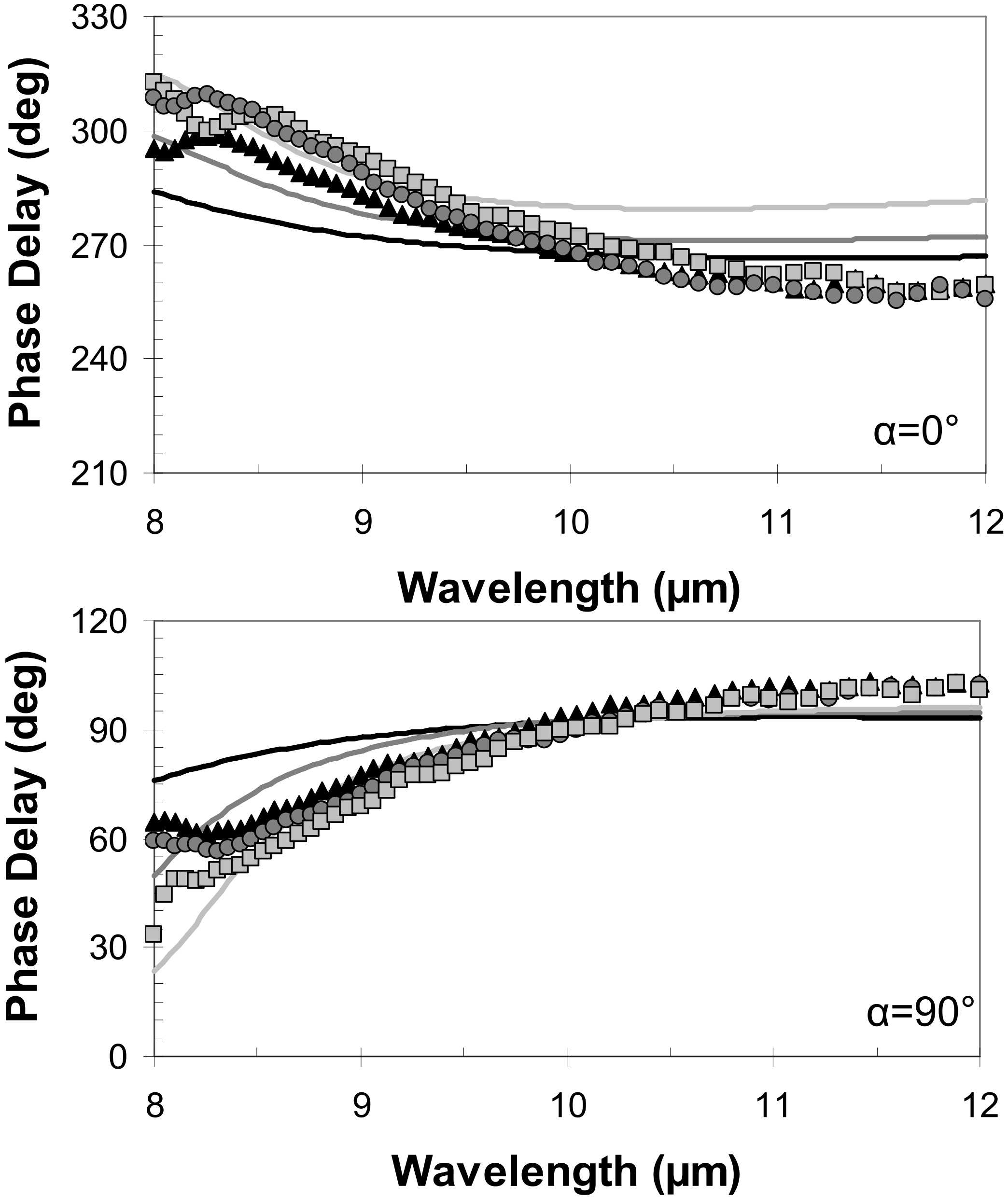

Figure 46 Measured and modeled relative phase delays for the angles of incidence of 0°, 40°, and 60° along the planes of incidence along α=0° (top) and 90° (bottom). The solid lines are modeled results and represent: 0° (black), 40° (med gray), and 60° (light gray). The measured results are represented as: 0° (triangle), 40° (circle), and 60° (square).

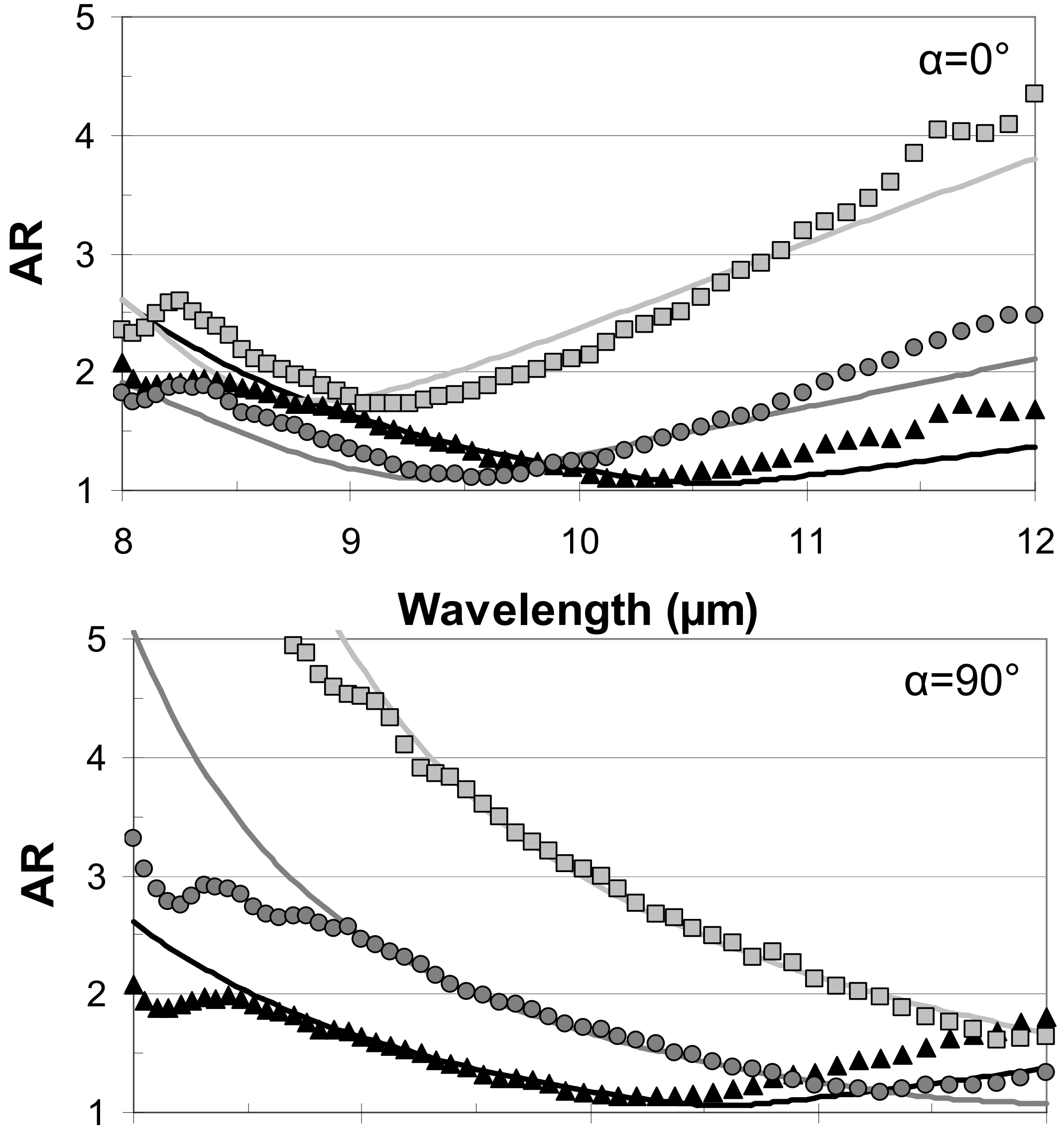

Figure 47 Measured and modeled axial ratios for the angles of incidence of 0°, 40°, and 60° along the planes of incidence along α=0° (top) and 90° (bottom). The solid lines are modeled results and represent: 0° (black), 40° (med gray), and 60° (light gray). The measured results are represented as: 0° (triangle), 40° (circle), and 60° (square).

The meanderline element was measured using the infrared variable-angle spectroscopic ellipsometer (IR-VASE), working in transmission for a range in the incidence angles between 0º and 60º, with measurements every 2º. The output of the ellipsometric data has been processed to obtain the phase delay between components, and the axial ratio (AR) of the polarization ellipse when illuminated with linearly polarized light oriented at 45º with respect to the meanderlines. The measurement has been done for the spectral range of interest (8 – 12 μm).

The modeled and measured results for the off-angles of incidence characterizations show good correlation. The good correlation is shown for both planes of incidence. The analysis of the phase delay characterizing the retarder element shows that the change in the angle of incidence, θ, produces little effect on this parameter. The effect is even less noticeable for the $\alpha = 90º$ orientation where the prediction from the model show a more stable dependence. This performance allows for extending the use of these retarders well beyond the paraxial range without a significant departure in the phase delay introduced by the element. The spectral dependence of the axial ratio for three different angles of incidence ($\theta = 0º$, 40º, and 60º) is plotted in Figure 47. In the case of $\alpha = 0º$, the AR minimum shifts toward shorter wavelengths as the incidence angle increases. However, when illuminating in the plane $\alpha = 90º$, the lowest AR moves towards longer wavelengths when increasing the angle of incidence. It is also observed that the average AR remains less than 3 in the whole band for angles of incidence up to 40° for both planes of incidence. Since the phase is fairly constant, the change in the AR can be attributed to the change in the projected amplitudes of the incident electric field onto the meanderline structure as the incidence angle is increased. At off angles, the incident ratio of the two orthogonal field amplitudes is not equal to 1 since the component of the field in the plane of incidence will have its projection onto the meanderline decreased by the cosine of the incident angle. This also explains why the AR shifts to shorter wavelengths along one plane of incidence and to longer wavelengths for the other plane. It is also important to note that there were no diffraction effects observed as the angle of incidence increased since the period was much smaller than the wavelength.

To make a comparison of the angular performance of this meanderline to a birefringent crystal quarter-wave retarder, the case of a single wavelength will be considered first. At a wavelength of 10.3 μm the meanderline retarder exhibits a minimum AR of 1.1. At an angle of 40° the AR is 1.4 and at an angle of 60° the AR is 2.4 as seen from Figure 47. For comparison, Figure 3 shows that both multiple–order and compound-single-order crystal retarders have a retardance that corresponds to an AR of 1.3 at angles of incidence of just 8° and 11°, respectively. The single-order crystal quarter-wave plate will have an AR = 2 at an incidence angle of 40°, but at 60° the optical path length within the crystal has doubled causing the quarter-wave plate to now act as a half-wave plate transmitting linearly polarized light with an AR = ∞. Therefore the meanderline shows more stability of the AR as a function of incidence angle.

For a spectral comparison of the meanderline to a crystal retarder, it is observed that the measured AR remained under 2 for the entire LWIR band. As per Figure 3, the meanderline retarder functioned much better than a multiple-order quarter-wave plate. The single-order and compound-single-order retarders show a retardance corresponding to an AR = 1.6 for 85% of the center wavelength, 8.7 μm in this band, and an AR = 1.2 for 115% of the center wavelength, 11.8 μm in this band. For an even comparison, the AR at 8.7 μm and 11.8 μm is 1.8 and 1.7, respectively, for the single-layer meanderline. Therefore the single-layer meanderline retarder showed a spectral performance similar to the performance of the ideal crystal quarter-wave plate in terms of spectral axial ratio.

The integrated spectral transmissivity was also calculated by means of Equation 49.

$$T_{p,s}(\theta,\alpha) = \frac{\int_{8\mu m}^{12\mu m} T_{p,s}(\lambda,\theta,\alpha)\Phi_{\lambda,bb}(\lambda,T=300)d\lambda}{\int_{8\mu m}^{12\mu m} \Phi_{\lambda,bb}(\lambda,T=300)d\lambda}, \qquad \text{Equation 49}$$

In Equation 49, $\Phi_{\lambda,bb}(\lambda,T=300)$ is the spectral blackbody radiance at 300 K. Then $T_{p,s}(\theta,\alpha)$ expresses the in-band transmittance for thermal sources at room temperature as a function of the angle of incidence, θ, the orientation of the plane of incidence, α, and the orientation of the electric field, parallel (TM) or perpendicular (TE) to the plane of incidence. The results are given in Figure 48. It is observed that the in-band transmittance is better bounded for the case of $\alpha = 0^{\circ}$ than for the case $\alpha = 90^{\circ}$. Though the angular performance of the integrated transmission is stable, it is observed that even at normal incidence the overall transmission of the meanderline retarder is about 15%. This low transmission is due to the impedance mismatches of the silicon and the meanderline structure with air as previously discussed. To improve the transmission of this structure, an anti-reflection coating can be applied to the backside of the silicon wafer. With this coating, the transmission of an lossless single layer meanderline will be 35.5% and therefore the transmission of this design can be increased.

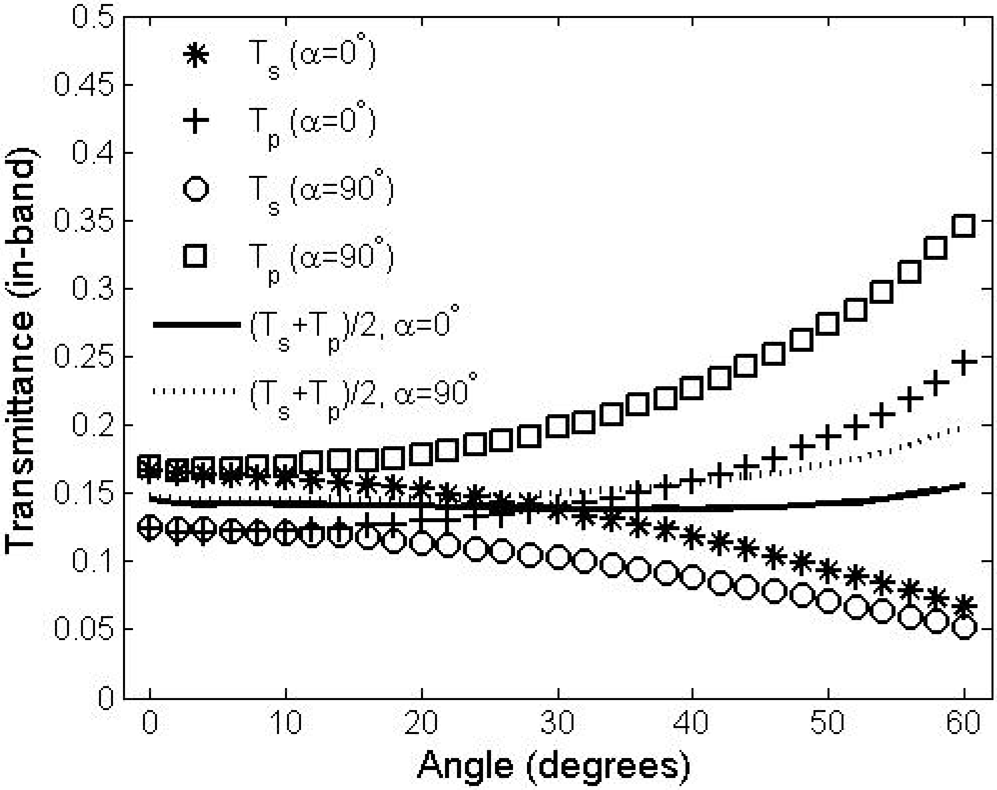

Figure 48 Plot of the integrated orthogonal transmissivity for a blackbody thermal emitter at T = 300K radiating through the single layer meanderline of silicon. Note how the integrated transmissivity remains flat at ~14% up to an incident angle of 40° for both planes of incidence.

5.1.3 Design #3: Double-Layer 90° Meanderline Retarder on Si with Si Standoff Layer

Once the single-layer meanderline was fully characterized, efforts were begun to investigate the feasibility of using multiple-layer meanderlines separated by a dielectric to increase the transmission through the structure. The design for multiple layers began by expanding the meanderline structure to two layers on a silicon substrate, design #3. Ideally, this will match the impedance of the meanderline stack to the characteristic impedance if the silicon. For the case of a meanderline stack that is matched, the transmission will be limited in the LWIR to 55% by the double interface reflections caused by the impedance mismatch of the silicon to air.

The ability to evaporate elemental silicon was developed and therefore silicon was used as the standoff layer for the meanderline. Silicon was desired since it would match the characteristic wave impedance of the substrate to the characteristic impedance of the standoff layers. The goal was to design and fabricate the double layer meanderline with a superstrate layer of silicon. The immersion in silicon was expected to simplify the electrical environment around each of the meanderline layers. Each of the meanderline layers had identical geometry as it was desired to have a 45° phase delay induced at each layer. The primary complication with the intended double layer device was that it involved actually fabricating two separate meanderline layers separated by a dielectric standoff layer. This standoff layer requires special fabrication techniques to successfully allow for the fabrication of the top layer. This fabrication process is described in Section 3.1.2.4. A cross-section of the double-layer meanderline structure is shown in Figure 49.

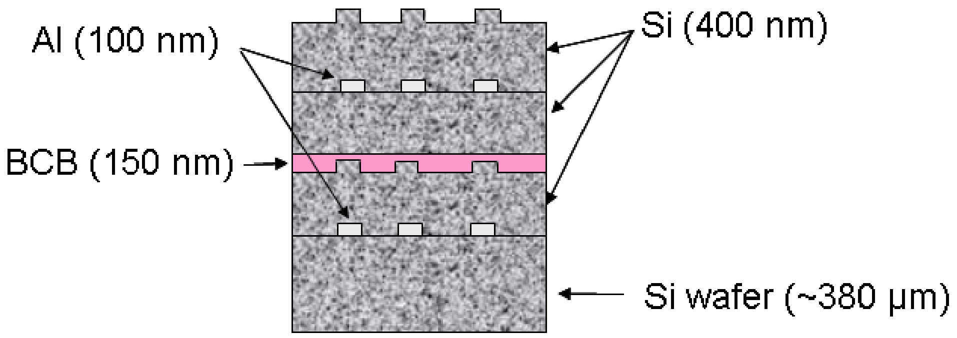

Figure 49 Cross-section of the double layer meanderline including the Si standoff layers and BCB planarization layer

The modeling of the double layer meanderline was essentially an extension of the single layer meanderline design. The primary difference was that the model was set up as two meanderline layers immersed in silicon. The silicon was modeled as infinite half spaces since this was the initial expectation to approximate the double layer meanderline with a silicon superstrate. Once the meanderline was fabricated it was realized that although the source of illumination was broadband, there were interference effects in the superstrate silicon layer. The superstrate layer thickness, 990 nm as measured, acted like a transmission line and the transformed impedance of the meanderline varied with the silicon thickness. These investigations will be shown at the end of this section including the updated model used to account for coherent interference of the radiation in the superstrate layer. The substrate was 380 µm thick and was well thicker than the correlation length for the source in the material; therefore it was accurately modeled as an infinite half-space with the transmission data being corrected in the same fashion as the single layer meanderline.

Using the PMM software the design for the double layer meanderline was developed. Since the goal was to have two meanderline layers with equivalent geometries, the design began with a single layer meanderline immersed in silicon that would apply a 45° phase delay. The metal used for the double layer meanderline on silicon was changed to aluminum because of its expected higher conductivity at these frequencies as compared to gold. [35] The second meanderline layer was added over a silicon standoff layer with an effective quarter-wave thickness at the central frequency. This thickness equated to 890 nm which included the BCB planarization layer. PMM was used along with the measured frequency-dependent material properties to optimize the performance by maximizing the efficiency, defined as the percent of initial optical power transmitted in the desired polarization state. Several dielectrics were characterized for use as a dielectric standoff layer, but evaporated silicon was chosen since it is essentially lossless in the long-wave IR. Although silicon's high permittivity (ε_r~11.7) was not desired for bandwidth considerations, it allowed for thinner dielectric layers for the same effective propagation distance (ideal from a fabrication perspective). The optimized meanderline geometry for both layers was: w = 0.225 μm, pw = 0.6 μm, ph = 0.5 μm, and dx = 1.2 μm. The ideal dielectric standoff thickness was 0.890 μm. The model with these parameters showed an axial ratio ≤ 1.5 from 8 – 12 μm; however the design was remodeled after fabrication to include the as-fabricated dimensions. The dimension that varied was the width which increased to 0.3 μm from the design width of 0.225 μm. The first and second Si thicknesses were changed from 400 nm to 340 nm and from 400 nm to 415 nm, respectively, as measured for a total Si thickness of 755 nm.

This design showed an axial ratio of ~2 from 8 - 12 μm and an average measured transmission of 22%. The measured axial ratio and phase delay are shown along with the modeled results in Figure 50. From the measured results, it is observed that the phase delay and axial ratio remain fairly flat from ~9 μm to 14 μm. The peak in the phase delay seen at 8.3 μm seems to be due to the Fabry-Perot resonance set up within the silicon superstrate layer. This is plausible because after fabrication, more silicon was deposited onto the superstrate to determine its effects. The peak in phase delay shifted to longer wavelengths as the thickness of silicon increased as shown in Figure 51.

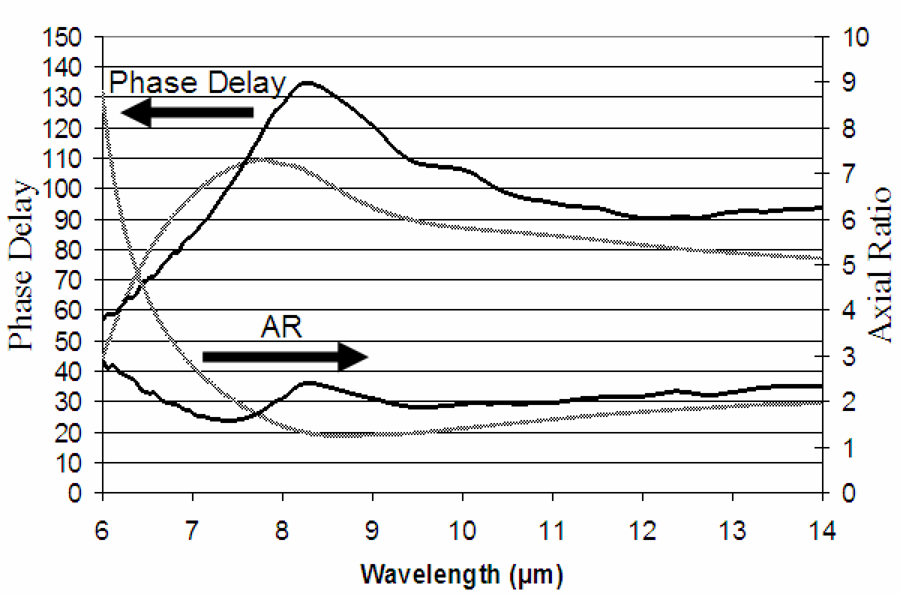

Figure 50 plot showing the measured (black line) and modeled (grey line) performance of the double layer meanderline fabricated on silicon using a silicon standoff layer with a superstrate silicon thickness of 400 nm.

Therefore, it is feasible to consider that if the superstrate layer is at an appropriate thickness, the peak can be at a substantially higher frequency that will allow for very flat phase response and axial ratio performance in the band of interest. It may also be conceivable that the best thickness may very well be a zero thickness superstrate since we will see that the trend shows a performance degradation as the thickness is increased. However, it is also observed that the spectral location of the intersection of the two transmission coefficients moves to longer wavelengths as the superstrate thickness increases. This spectral location is of importance since its ideal location is in the center of the band of interest. The performance of the double layer meanderline was characterized with each increase in the silicon superstate thickness and the data is shown in Figure 51.

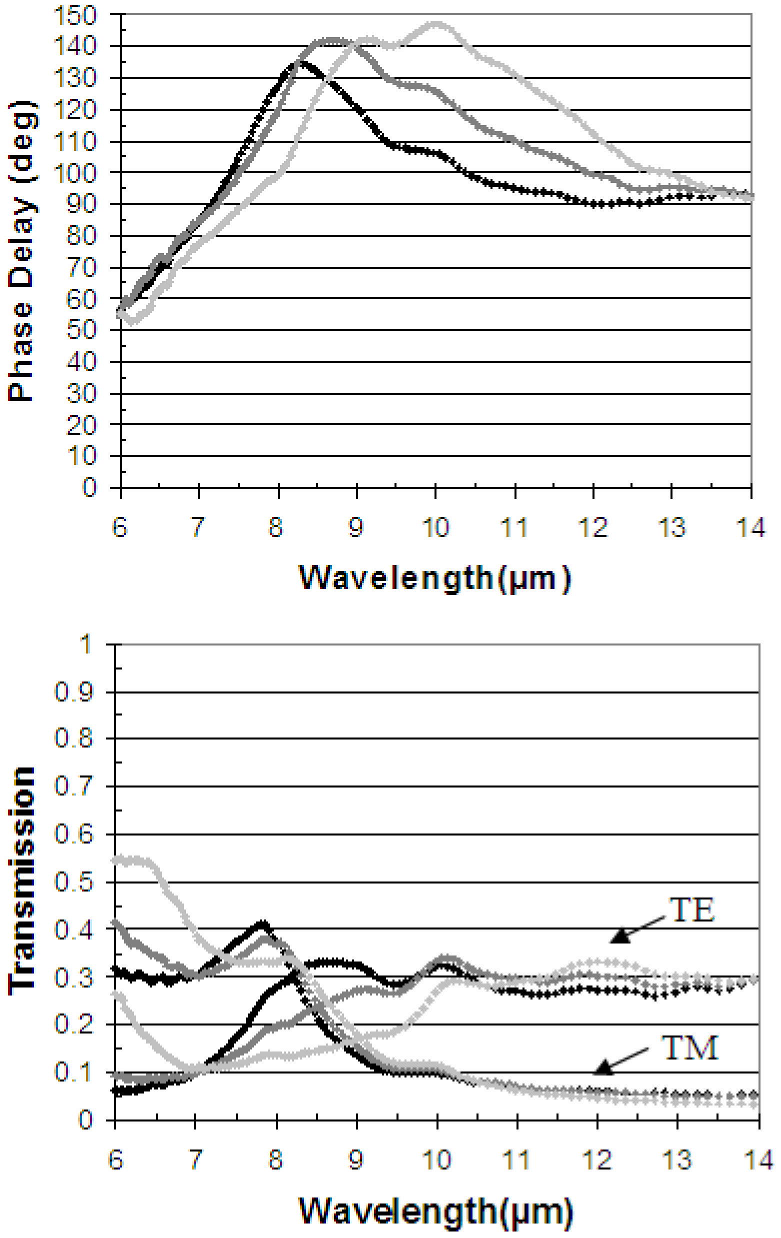

Figure 51 The graphs above show the phase delay (top) and orthogonal transmission coefficients (bottom) induced by the double layer meanderline on silicon. The superstrate thicknesses are 987 nm (black dots), 1112 nm (medium grey dots), and 1326 nm (light grey dots).

Though this design did not perform ideally, its performance does allow for some conclusions to be drawn. The phase delay varied from 130° to 90° over 8 μm – 12 μm. The phase delay was greater than the desired 90°, but shows that the transmission would be improved over the single layer design for the same phase delay. The higher the phase delay in a meanderline structure, the more reflections will be expected. The integrated LWIR transmission of this structure was 22%, even though the phase delay was larger than 90°. The conclusion drawn is that if the fabricated structure were to operate with a phase delay of 90°, the transmission would have been larger than the transmission of the single layer meanderline. Also, though the silicon superstrate varied the polarimetric performance as a function of its thickness, this problem can be mitigated with the use of an anti-reflection coating over the silicon superstrate. The anti-reflection coating will prevent any reflections from the top silicon boundary back to the meanderline structures. With another antireflection coating applied to the back side of the silicon wafer the transmission of the overall structure can be increased.

The power budget analysis for this structure included the double interface dielectric reflection, R_{sub}, of 45% and an expected meanderline ohmic loss, A_{metal}, that would be similar to the proof-of-concept design at about 28% for each meanderline layer. The predicted transmission assumed that the structure would have a good impedance match, and the expected transmission was 29%. Using the measured transmission that averaged 22%, the reflection loss, R_{meaner}, was calculated via Equation 34. The calculated reflection loss was 22% for the meanderline structure.

The overall analysis of this structure is that it shows a very flat axial ratio over the LWIR. This spectrally flat axial ratio shows that using multiple layers of meanderlines may potentially broaden the band of operation over the use of single layers. It was also observed that the transmission of the structure was 22% as compared to the single layer meanderline which had 15%. The increase in transmission was due to the impedance matching by using more than one layer of meanderlines even though the higher than desirable phase delay led to some reflections from the meanderline stack with this design.

5.1.4 Design #4: Triple-Layer 90° Meanderline Retarder on Si with Si Standoff Layers

The next step in expanding the multiple layer concepts for the meanderline was to design and fabricate a three-layer meanderline. The initial belief was that the transmission could be increased over the double layer design due to better impedance matching of the layers to the silicon.

However, there was also the possibility that the increase in the layers could cause more loss, due to the gold meanderlines, than could be gained via impedance matching. Though it was known that Al had a higher IR conductivity, Al could not be used due to a process issue with its evaporation at the time of fabrication. So, Au was used for this design. A schematic of the three layer meanderline concept is shown in Figure 52.

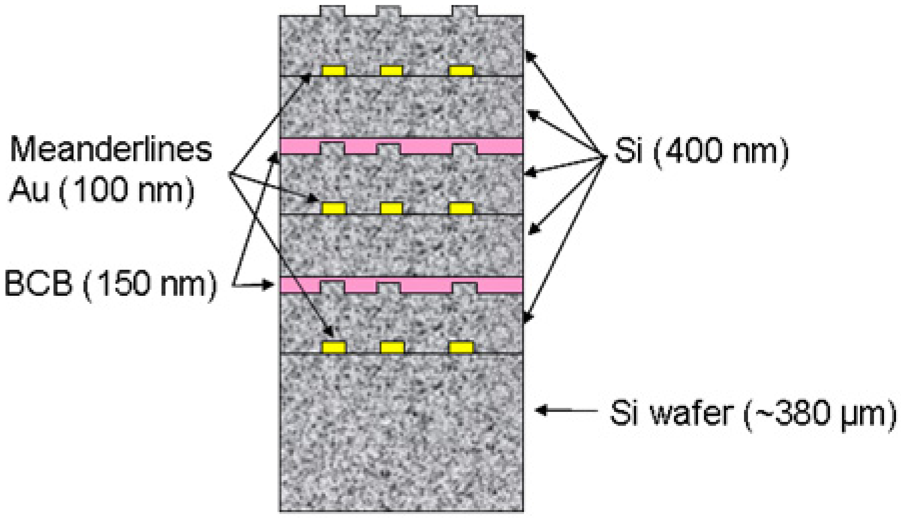

Figure 52 Schematic showing the cross section of the three layer meanderline stack

To achieve the performance necessary to give a full retardance of 90° for the three-layer meanderline, the middle layer had to induce a phase delay that was two times the phase delay of the outer two layers. This is seen if the ideal performance of the three layer meanderline is visualized on a Smith chart as depicted in Figure 53. To get the desired phase delay of 90°, it is necessary that the inductive phase advance be equal and opposite to the capacitive phase delay for each of the orthogonal components. The figure shows the capacitive phase delay as it propagates through the three layers. The phase delay induced from the first and third layers are still half of the phase delay induced in the second layer. The end goal is to obtain a solution that is close to the center of the Smith chart to have an impedance match along with the needed phase delay.

The necessity for relatively small phase delays at each layer led to the widths of the meanderlines to be very small compared to the larger single-layer structure. The design parameters for the top and bottom layers of the three layer meanderline retarder were: $w_{\text{top/bottom}}$ = 150 nm, w_{middle} = 200 nm, *pw* = 0.4 µm, *ph* = 0.5 µm, and *dx* = 1.0 µm. The thickness of Au deposited was 100 nm with a Ti adhesion layer thickness of 5 nm. The difficulty with this design for both the modeling and the fabrication was the necessity to have an intermediate layer of BCB sandwiched between two silicon layers.

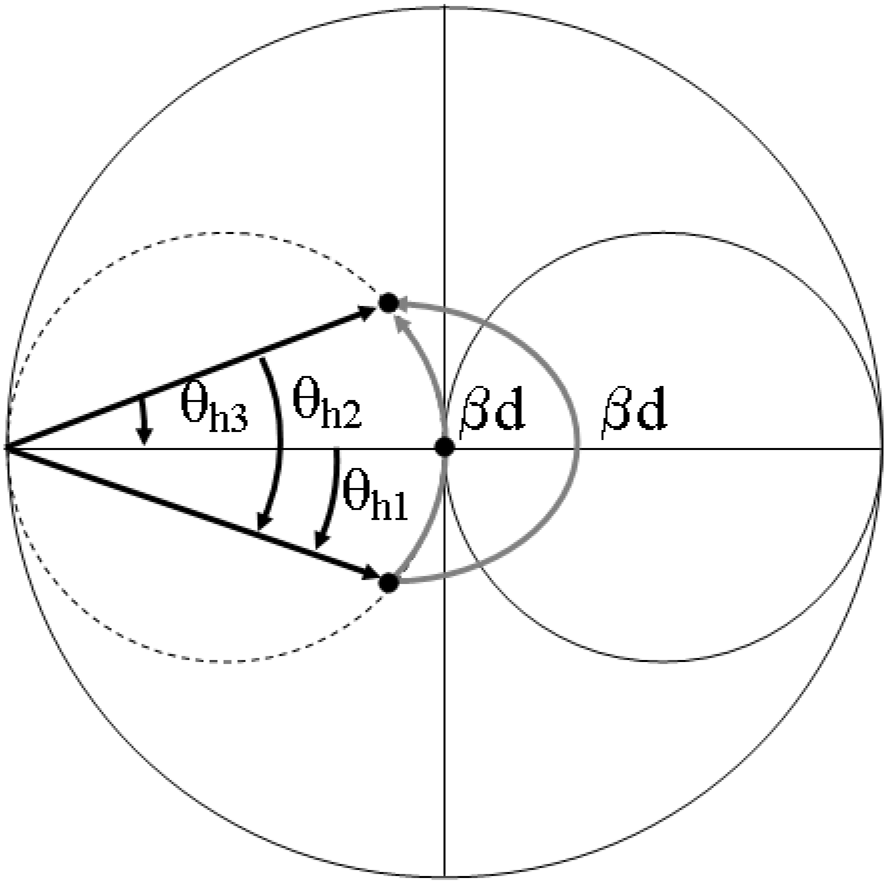

Figure 53 Smith chart representation of the ideal three layer meanderline structure and the induced phase delay caused by the capacitive component (the component perpendicular to the meanderline axis). It is of note that the final location is matched at the center of the Smith chart while also having a total phase delay of 22.5°.

This was necessary as discussed in Section 3.1.2.4 to planarize the evaporated silicon layer in preparation for the fabrication of the layer above. However, the layer of BCB was spun on for a thickness of 150 nm which was experimentally determined to be sufficient for lithography, and the thickness of the silicon pillars were 100 nm. This led to a very difficult layer to model due to the intermixing of the silicon pillars and the BCB. This also left the “true” thickness of BCB unknown for the input into PMM. It was expected that the BCB would not have a strong impact on the performance due to its small thickness with respect to the effective wavelength in the silicon. The thickness of the BCB was expected to be approximately 5% of the effective wavelength. The method for modeling this was to treat the silicon/BCB/silicon layer as a planar stratified dielectric stack within PMM.

The modeled and measured results for the three layer structure are shown in Figure 54. From this data it is observed that the basic functionality for a three-layer meanderline retarder using silicon is confirmed. However, it is also noted that the induced phase delay is fairly high at an average measured value of 130°. This high phase delay is due to the fact the widths of the meanderlines were in fact larger than they needed to be to induce a net 90° phase delay. To improve the phase differential performance of the structure it would be necessary to reduce the line widths, thereby increasing the difficulty in fabrication. However, even though the phase differential performance could be improved, it is observed that the transmission coefficients are still very low with an average 16.8% transmission for the band. The introduction of a third layer of structures introduces more metallic losses and does not effectively improve the overall functionality of the meanderline in the LWIR using silicon as a substrate and standoff material.

The power budget analysis included a 45% loss due to the double interface dielectric reflections of the silicon, R_{sub}. Using the loss calculated in the proof-of-concept design, 28% of the incident power was attenuated, A_{metal}, in each layer for a total loss of 63% for the three layers. The transmission of the three layer meanderline was 16.8%. Using Equation 34, the loss due the reflection of the meanderline stack, R_{meander}, can be calculated. Such a large phase delay implies that the impedance is greater than what was necessary for the 90° retardance and therefore reflections will exist because the meanderline stack was not ideally matched to the silicon. The calculated reflection loss due to the meanderline stack was 18%.

The calculated reflection loss of the three layer stack, 18%, is less than the calculated reflection loss of the double layer stack, 22%, even though the phase delay of the three layer stack was greater. The phase delay of the two layer stack averaged 110° and the three layer stack averaged 130°. Though the reflection loss of the meanderline stack was lower for the three layer design, the ohmic loss of three layers of meanderline became the limiting value at a total of 63% of the incident power being dissipated in the metal. Therefore, for the IR, the most layers a meanderline design can have to maintain a relatively high transmission is limited to two.

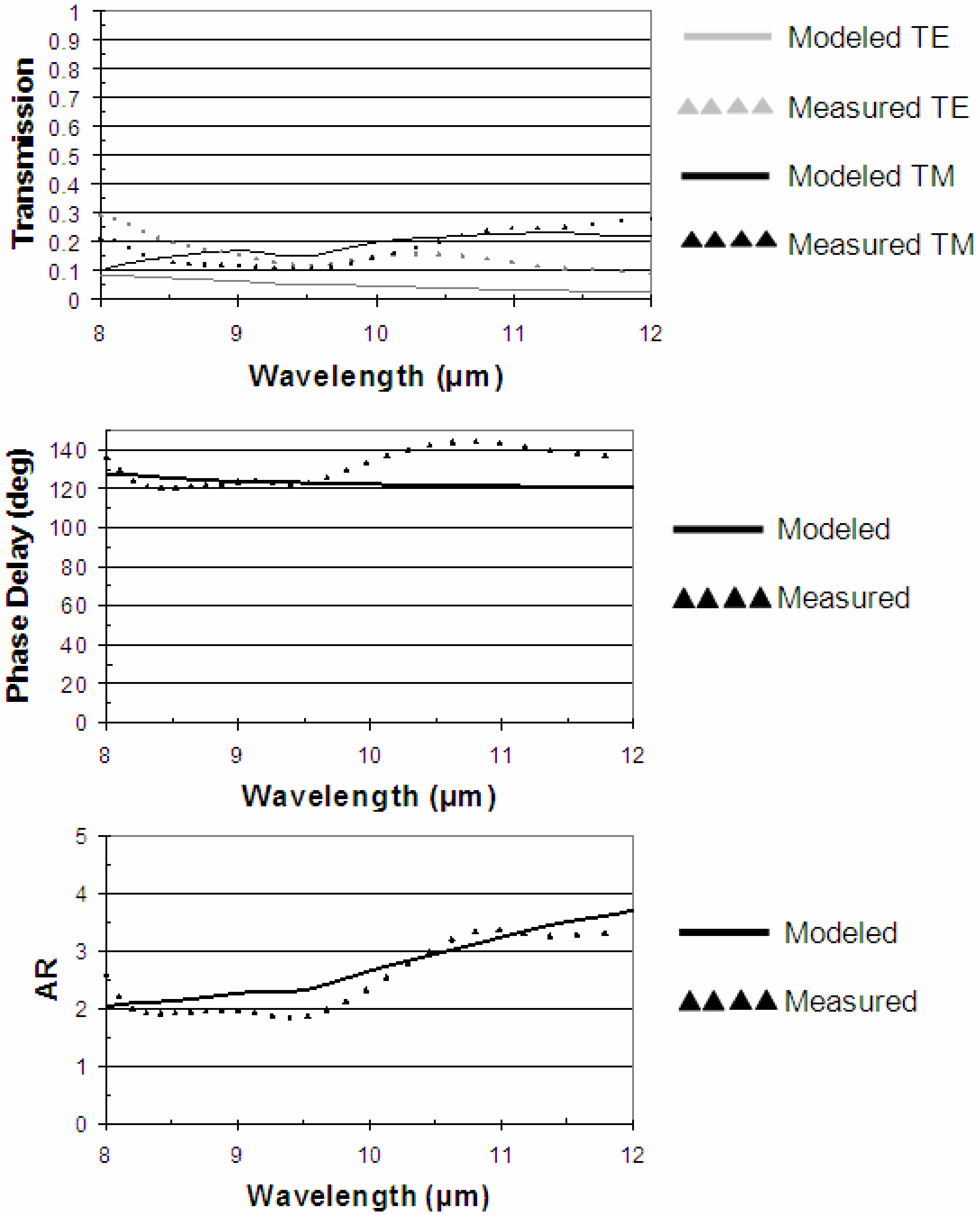

Figure 54 Plots showing the modeled and measured performance of the triple-layer meanderline design on high-resistivity silicon at normal incidence using the Si/BCB/Si standoff layer

Desired width = 150 nm (top/bottom layer of 3-layer design)

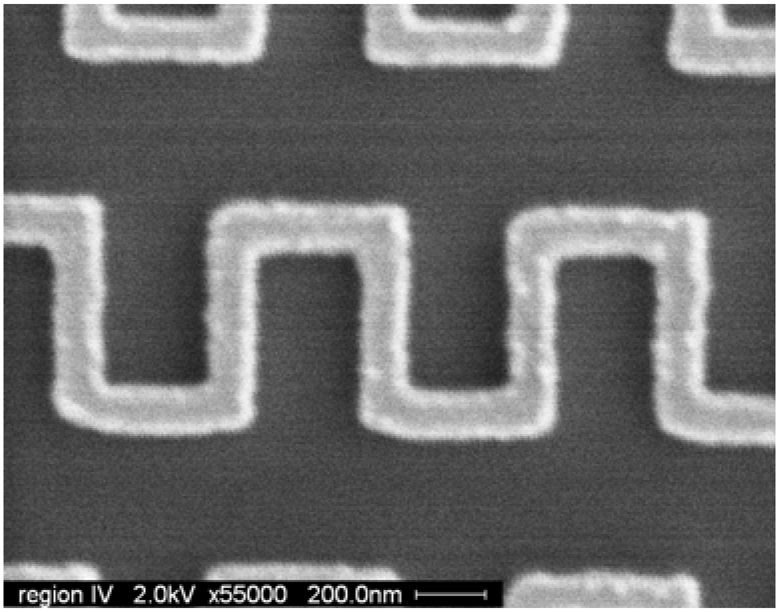

Desired width = 200 nm (inner layer of 3-layer design)

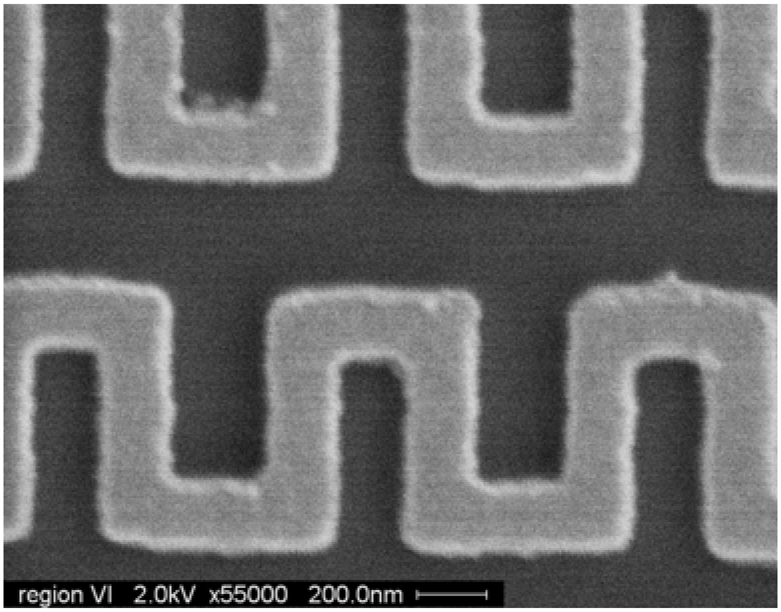

Figure 55 SEM images of the two designs for the three layers of the three layer meanderline retarder.

5.1.5 Design #5: Double-Layer Meanderline Retarder on BaF_2 with BCB Standoff Layer

The goal in the LWIR was to have a broad-band quarter-wave retarder. The initial efforts using multiple layer meanderlines involved the use of silicon substrates and silicon as the standoff medium between the adjacent meanderline layers in the stack. The polarization properties showed good performance over this band, however as discussed in earlier sections, the transmission was relatively low at ~15%. A double layer meanderline, design #5, was fabricated onto barium fluoride due to it low permittivity and large transmission bandwidth. The difficult aspect using BaF_2 was that there were no examples in the literature of fabricating structures onto a BaF_2 substrate using e-beam lithography. There were certainly no discussions concerning the multiple layer lithographic processes that would be necessary to fabricate this stacked structure. Therefore, this design would have some difficulties that would have to be overcome during the course of fabrication. However, the expected gains in performance, specifically transmission, would make the investigation relevant.

The first design modeled and measured was the first effort to fabricate a multiple layer meanderline retarder onto the barium fluoride substrate. The goal was to demonstrate that a double layer meanderline could function and be fabricated on the BaF_2 substrate. The differences in the fabrication of the meanderline on fused silica and barium fluoride are significant. First, since both substrates were transparent, Ni was again used to offer a route to ground and a reflective layer for the Lieca e-beam writer. The primary difference occurred when removing the ZEP resist while lifting off the excess metal evaporated for the meanderlines. Initially, after liftoff, the structures would look normal and function. The BCB was then spun on to a thickness of 1.3 μm and the next layer was written and metallized. The lift-off process is where the complication arose, and these complications were that, upon submersing the wafer into a bath of methlyene chloride, the BCB layer would lift off of the barium fluoride. It took several iterations of fabrication to determine why this was a problem, especially since it was well known that the BCB did not dissolve in any of the organic solvents used: Acetone, IPA, methanol, methylene chloride. The problem was found when the processing differences were analyzed between the use of fused silica and barium fluoride. When baking the ZEP520A-7 resist on the fused silica, it baked for five minutes at 180°C and then was promptly removed from the hot plate. However, when processing the barium fluoride substrate, the resist was baked for five minutes at 180°C, and then the hotplate was set to cool slowly at a rate of about 4°C/minute until room temperature. It was necessary to have this rate of cool down to prevent the barium fluoride wafer from cracking into several pieces because of its susceptibility to thermal shock of the material. The ZEP resist was then baking for much more time than for the fused silica wafer processing. As ZEP is baked for longer periods of time, it will dissolve more slowly in organic solvents including methylene chloride. The barium fluoride wafer soaked in methylene chloride for ten minutes, and this was enough time to remove the excess metal on the wafer. Upon inspection in a microscope, the structures appeared fine, however even though the excess metal had lifted off not all of the ZEP resist had dissolved away from wafer surface. Thus when the next BCB layer was spun on and another meanderline layer was written, the lift off process of soaking in methylene chloride for ten minutes would continue to dissolve the ZEP resist beneath the BCB layer. As the ZEP continued to dissolve beneath the BCB layer, it would come off of the wafer. The solution was to use a more aggressive solvent for the ZEP resist, ZPMAC ZEP remover (Zeon Corporation). ZPMAC was specifically designed to dissolve ZEP resist and when this remover was used for the liftoff processing, there were no more issues with the adhesion of the BCB to the Barium Fluoride substrate.

Once this fabrication issue was solved, the initial design was fabricated and tested. BCB was the only available material that could be used as the standoff layer, so the spectral losses and refractive index perturbations were expected to be visible in the measured and modeled data. The advantage of using BCB (n~1.55) is that it has a refractive index that is similar to the barium fluoride (n~1.4) which allows for fairly good dielectric matching at the interfaces and electrically similar environments around the meanderline structures.

The initial design parameters were: $w = 0.5$ µm, $pw = 1.6$ µm, $ph = 1.2$ µm, and $dx = 3.0$ µm. With these parameters, the device was fabricated using Al with the top and bottom layers having identical geometry. A cross section of the structure stack is shown in Figure 56. The thickness of the BCB standoff layer was 1.3 µm.

The power budget analysis is as follows. It was expected that the BCB would affect the spectral performance of the meanderline retarder because of its spectral attenuation in the LWIR. The loss that was expected based on a calculation that incorporated both the integrated material attenuation loss of the 1.3 µm of BCB (10%) and the dielectric reflection loss (9.1%) was 19.1%, A_{standoff}. If it is assumed that the ohmic losses of Al are similar to Au then the measured metal loss of Section 5.1.1 can be used to estimate the losses for this structure. The measured loss was

28% for a single layer, A_{metal}. Therefore a two layer structure would be expected to have an ohmic loss of 48%. Therefore the ideal power transmission of a perfectly matched double layered meanderline on BaF_2 using BCB as the standoff material is expected to be 42%. The empirically determined sheet resistance for the Al on the BaF_2 was 12 Ω/□ for the double layer stack.

The measured and modeled performances of this design are shown in Figure 57. It is observed in Figure 57 that the transmission coefficients are modeled to be much lower than they were measured to be. This is due to the necessary adjustment to the input sheet resistance that was to improve the correlation in the modeled and measured polarimetric values.

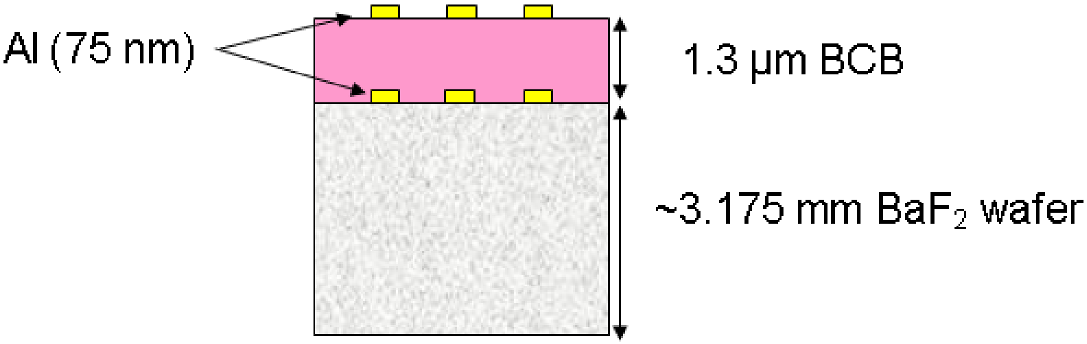

Figure 56 Cross section of the double-layer LWIR meanderline retarder fabricated onto the BaF_2 substrate

The primary benefit for this measurement is that it shows that a double layer meanderline structure can be fabricated onto the barium fluoride substrate that could be made to function as a 90° retarder. It is also seen that the expected benefit of the higher transmission over the use of the silicon substrate is substantiated as the average transmission for this structure was 60% over the 8 – 12 μm band of interest. Though the expected transmission was 42%, the higher measured value corresponds to the fact that the Al is less lossy than the gold that was used earlier. The loss as measured for each aluminum layer, A_{metal}, is 14%. The total transmission is marked improvement over the ~15% measured using the silicon substrate. The AR remained below 2 for nearly the entire band which shows the potential for excellent spectral performance once the phase delay is increased to the desired 90°.

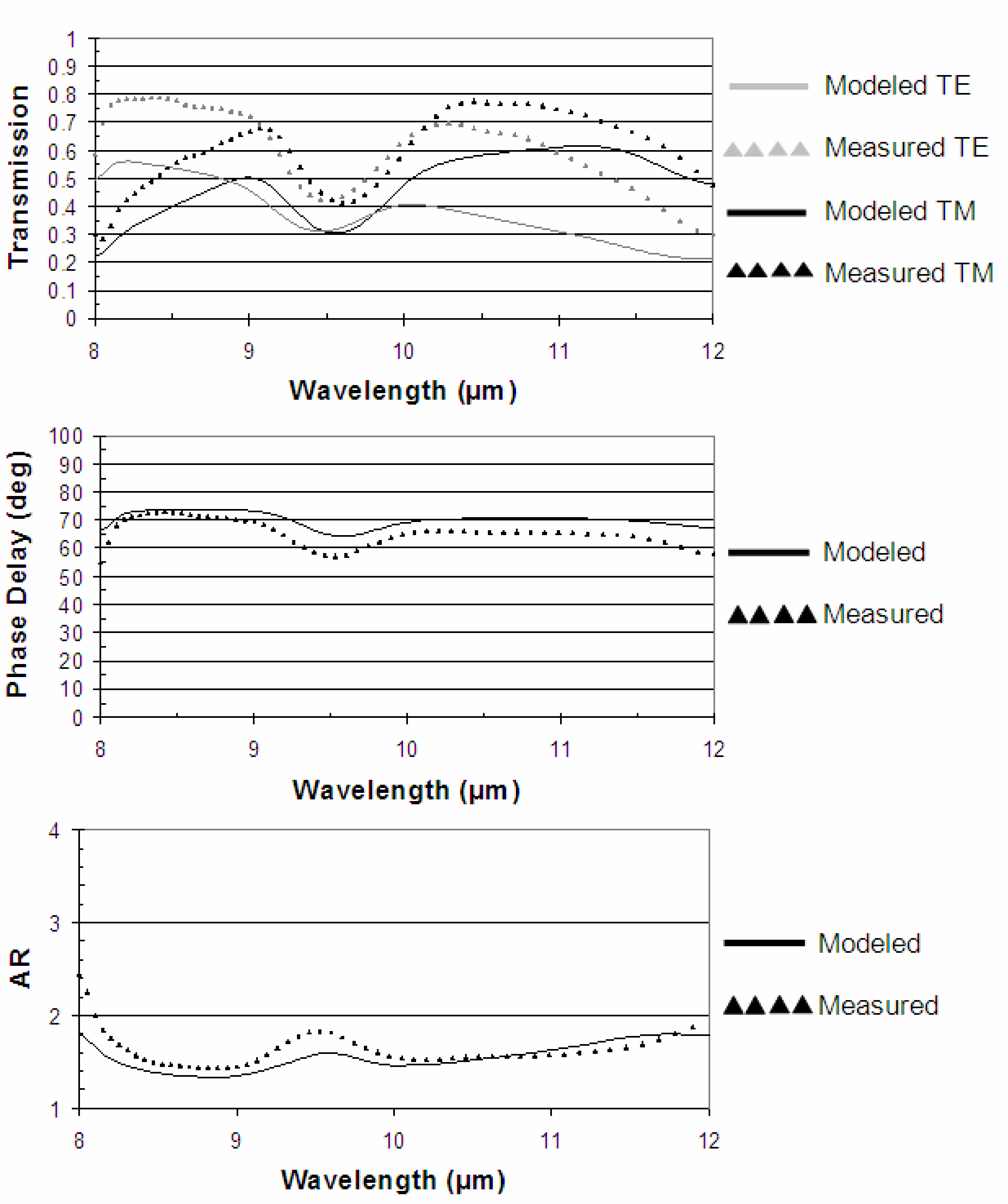

Figure 57 Measured (triangles) and modeled (solid) data representing the performance of the BaF_2 double layer meanderline.

5.1.6 Design #6: Single Layer Zig-Zag Retarder: Proof-of-Concept

The investigation of the meanderline retarders was extended to include another geometry. Specifically, the zig-zag pattern was investigated, design #6. Conceptually, it was expected that the zig-zag pattern should act in a similar fashion to the meanderline design as the inductive and capacitive descriptions for the meanderline would still hold, though more complex in nature. The geometry of the zig-zag pattern is depicted in Figure 58 along with the cross section of the fabricated structure.

When the parameters were optimized in the modeling the ideal parameters for the single layer were found to be: w = 550 nm, pw = 1.0 µm, ph = 1.3 µm, dx = 2.0 µm. The metal used was gold at a thickness of 75 nm. Using the equivalent sheet resistance that was determined for the single-layer meanderline on silicon, 7.25 Ω/□, the expected retardance was 90°. However, this change in geometry changed the value of the equivalent sheet resistance for this structure. The equivalent sheet resistance for this geometry on silicon was 12 Ω/□. The fabricated zig-zag meanderline is shown in Figure 59.

The polarimetric properties of the zig-zag meanderlines were expected to follow the same essential trends as did the meanderline structure for varying the geometric parameters. The best transmissive performance of the structure is to transmit 25% of its radiation in a circularly polarized state. The modeled and measured results for the zig-zag pattern are depicted in Figure 62. In the measured results, a broadband phase delay is observed with an AR that remains less than 2 for wavelengths greater than 9.5 µm. The integrated transmission for this structure is measured to be 23% which compares well with the single-layer proof of concept meanderline design which showed an average transmission of 30%. This design would be expected to have a lower transmission because of its higher induced phase delay compared to the proof-of-concept single layer meanderline design. This expectation is because the impedance mismatch of a single-layer structure will be greater as the phase delay is increased. This relation is depicted on the Smith chart in Figure 11.

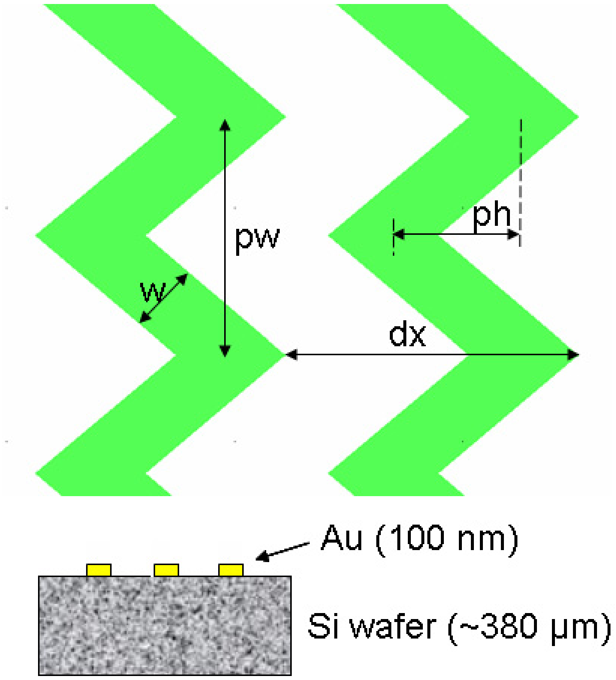

Figure 58 Depiction of the geometric definitions for the zig-zag meanderline line (top) and a cross-section of the structure as fabricated.

In summary, the concept and description of the meanderline is not limited by the geometry of the meanderline structure. This zig-zag pattern shows that if a structure is periodic, continuous in one direction, and discontinuous in the orthogonal direction it can demonstrate the anisotropic impedance that is necessary to change the polarization of transmitted radiation.

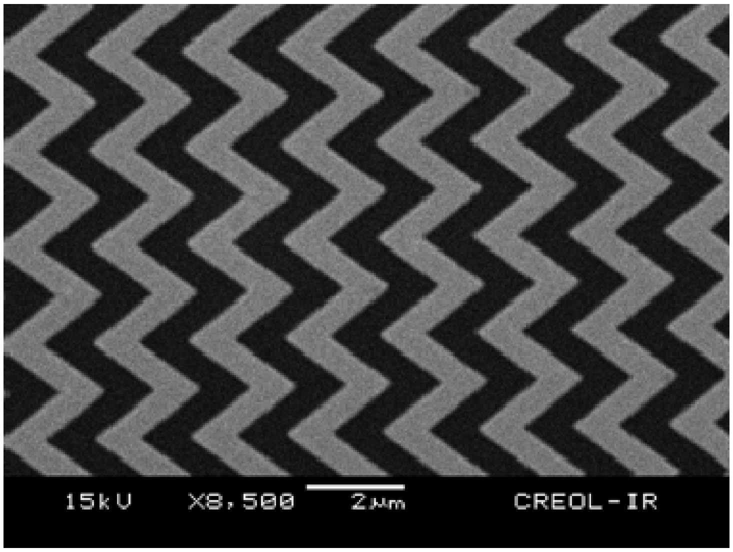

Figure 59 SEM images of the fabricated gold zig-zag variation of the meanderline geometry

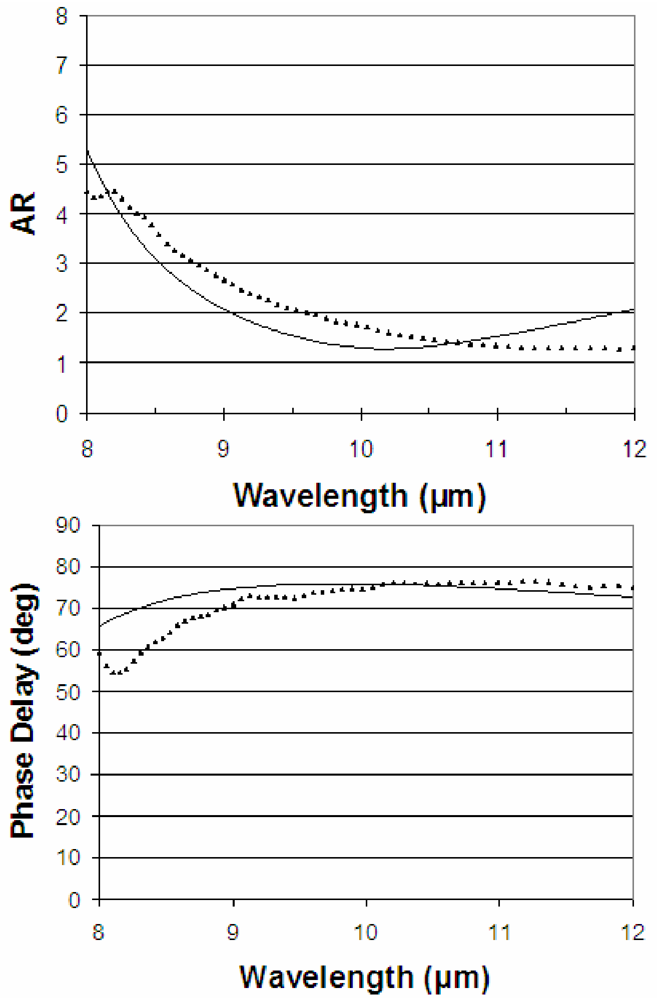

Figure 60 Measured (triangles) and modeled (solid) data representing the performance of the single-layer zig-zag meanderline design on silicon.

5.2 MWIR (3-5 μm) Meanderline Retarders

Once the meanderline retarder was demonstrated in the LWIR, it was desired to move the band of operation to the mid-wave infrared, wavelengths of 3 – 5 μm. The primary challenge with moving to this band is that the wavelengths become very small, especially in the materials. However, the line widths that can be fabricated are limited by the electron-beam writer which has demonstrated line widths as small as 20 nm. To aid in making the structures as large as possible, a low permittivity substrate was sought for this band. A low permittivity substrate was not easily realizable in the LWIR, however in the MWIR a good candidate material became apparent: fused silica. Fused silica is amorphous silicon dioxide and has an integrated in band transmission in the MWIR of 78%. The spectral transmission for fused silica was shown in Figure 32 and the optical properties are further discussed in Section 4.3.1.

5.2.1 Design #7: Double-Layer Meanderline Retarder on Fused Silica with BCB Standoff Layer

The refractive index of the fused silica is ~1.4 in the MWIR and this allowed for larger structures and less reflections due to the dielectric mismatches. Design #7, for the two layer meanderline, was to incorporate the BCB as a dielectric standoff layer because of its transmissive properties, as discussed in Section 4.3.4. This design was set to have an Au meanderline layer on the fused silica substrate, a thin layer of BCB, and then a final meanderline layer fabricated onto the BCB.

The goal for the double meanderline retarder on fused silica was to have a broadband phase delay of 90° to act as a broadband quarter-wave retarder. It was expected that these goals would be more likely to be achieved in this band due to the desirable optical properties of the dielectrics in this band. The equivalent sheet resistance value used was $2.6\Omega/\square$. The ideal expectation for the transmission of the double layer meanderline on fused silica was limited by a material attenuation and reflection that was measured to be 78%. Since gold was used, ohmic losses were expected and these losses were expected to be worse in the MWIR than in the LWIR [35].

The parameters that were determined to optimize the modeled performance of the double layer meanderline on fused silica were: $w_1 = 0.3$ µm, $w_2 = 0.26$ µm, $pw = 0.4$ µm, $ph = 0.5$ µm, and *dx* = 1.35 μm. The standoff thickness of the BCB layer was 0.65 μm and the gold thickness was 60 nm. In the above parameters, w_1 corresponds to the thickness of the top layer and w_2 the bottom layer. With these parameters in hand, the meanderline was fabricated and characterized. The schematic of the multiple layer meanderline is shown in Figure 61.

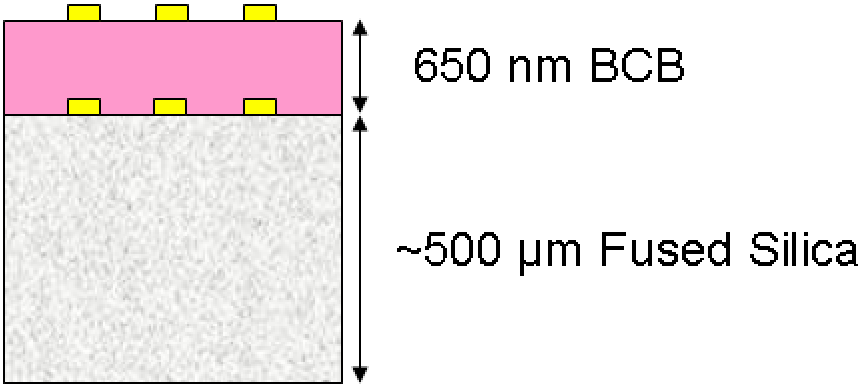

Figure 61 Schematic of fabricated stackup of the MWIR meanderline quarter-wave retarder including the spin-on dielectric standoff layer using Benzocyclobutene (BCB)

The measured performance of the MWIR meanderline retarder was characterized using the same method as with the LWIR, the IRVASE. The modeled and measured performance of the MWIR double-layer meanderline quarter-wave retarder is shown in Figure 62 for normal incidence.

The next characterization was to investigate the stability of the performance of the double-layer meanderline quarter-wave retarder for varying angles of incidence. The angles-of-incidence measurements were done in exactly the same way as for the single-layer meanderline retarder on the silicon substrate. The measured and modeled results were again plotted together to ensure reasonable correlation between them.

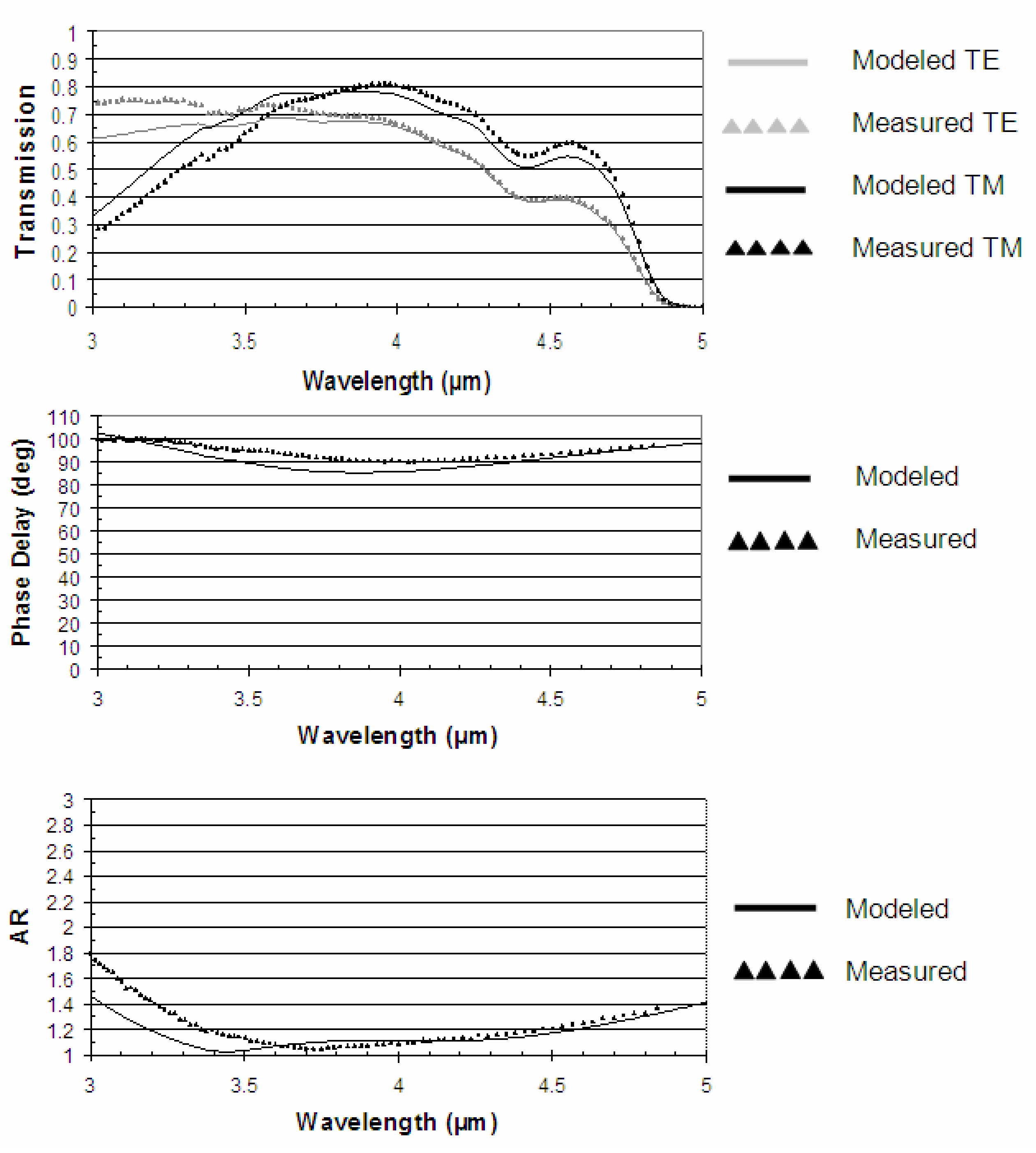

Figure 62 Plots showing the modeled and measured performance of the MWIR double-layer meanderline quarter-wave retarder at normal incidence

The integrated transmission of the structure over the MWIR band was 53%. The power budget analysis for this structure includes a loss caused by substrate attenuation, A_{sub}, of 22%. The meanderline structures are expected to have essentially zero reflections since the structure induced the desired 90° phase delay as described in Section 1.4.2.2. Therefore from the measured transmission of 53% and rearrangement of Equation 34, the expected ohmic loss due each metal layer, A_{metal}, is about 17.5%. The primary constraint on the overall transmission was the material attenuations of the fused silica substrate, as shown in Section 4.3.1, and the ohmic loss of the Au.

The spectral dependence of the axial ratio and phase delay for three different angles of incidence (θ=0º, 40º, and 60º) is plotted for α=0º in Figure 63 and Figure 64, respectively. It is observed that the average AR remains less that 2.0 for wavelengths greater than 3.5 μm and angles of incidence up to 40°. Both the modeled and measured data show that as the angle of incidence increases, the wavelength range in which the AR is less shifts to longer wavelengths. The short wavelength response has an AR that increases quickly. The modeled data correlates the trend in the shift of the AR curve as the angle of incidence increases along this plane of incidence. The phase delay of the modeled and measured data show minor variation for wavelengths greater than about 4 μm. However, the discrepancy between the modeled and measured data increases as the wavelength becomes closer to 3 μm.

The spectral dependence of the axial ratio and phase delay for three different angles of incidence (θ=0º, 40º, and 60º) is plotted for α=90º in Figure 65 and Figure 66, respectively. Along this plane of incidence the average AR remains below 2 for wavelengths greater than 3.5 μm and angles of incidence up to 60º. The AR is shows very little spectral variation up to 40º with the whole band having an AR below two. The phase delay also shows minor spectral variation until the short wavelengths. For this plane of incidence the modeled and measured data are well correlated, however the same trend in discrepancy is observed as for the other plane of incidence for the short wavelengths below 3.5 μm.

The discrepancy between the measured and modeled data at short wavelengths can possibly be explained by the ocurance of diffractive grating lobes. The period of the meanderlines in this design are spaced at 1.35 μm, equivalent to 0.675λ for a wavelength of 3 μm in the BCB standoff layer. Since the spacing is greater than 0.5λ, it would be expected that the top layer of the meanderline stack could diffract into the standoff layer causing some of the radiation to be trapped in the standoff layer because of internal reflection. This diffractive effect would be worse for the plane of incidence along α=90° because of reasons that were discussed in Section 1.4.3. This would reduce the power transmitted along those polarization angles. PMM includes diffractive calculations in its modeled results; however the discrepancy between the modeled and measured phase delays may be caused by the ellipsometer. The ellipsometer cannot directly measure the phase delay of incident radiation. It calculates the phase delay by measuring the geometry of the polarization ellipse in terms of power. Therefore, if the power along one polarization component decreases or increases while the other component is unchanged, with no change in the phase delay between the fields, it will not be interpreted by the ellipsometer that the phase delay is unchanged. The ellispsometer will measure the new polarization ellipse and calculate a new phase delay that corresponds to the new geometry. In this way diffractive effects may have led to the short wavelength discrepancies along both planes of incidence.

As per Figure 3, this meanderline retarder design functioned much better than a multiple-order quarter-wave plate as a function of wavelength at normal incidence. The single-order and compound-single-order retarders show a retardance corresponding to an AR = 1.6 for 85% of the center wavelength, 3.4 μm in this band, and an AR = 1.2 for 115% of the center wavelength, 4.6 μm in this band. For an even comparison, the AR at the wavelengths of 3.4 μm and 4.6 μm is 1.15 and 1.25, respectively. Therefore the double-layer meanderline retarder showed a spectral performance that exceeded the performance of the ideal crystal quarter-wave plate in terms of spectral axial ratio at normal incidence.

To make further angular comparisons of the performance of this meanderline to a birefringent crystal quarter-wave retarder, a single wavelength will be considered. At a wavelength of 4 μm the meanderline retarder exhibits a minimum AR of 1.1. At an angle of 40° the AR is 1.2 and at an angle of 60° the AR is 1.3 as averaged over $\alpha = 0°$ and 90°. For comparison, Figure 3 shows that both the multiple–order and compound-single-order retarders have a retardance that corresponds to an AR of 1.3 at angles of incidence of just 8° and 11°, respectively. The single-order crystal quarter-wave plate will have an AR = 2 at an incidence angle of 40°, but at 60° the optical path length within the crystal has doubled causing the quarter-wave plate to now act as a half wave plate transmitting linearly polarized light with an AR = ∞.

The final comparison between the double layer meanderline retarder and a crystal quarter-wave retarder is in terms of their transmissions. The transmission of a typical crystal that has been anti-reflection coated is approximately 98% and is usually limited by the operation band of the coating. This meanderline design has a transmission, at normal incidence, of 53%. The transmission performance of the meanderline is limited by the attenuation that is caused by the loss in the metal and the substrate as discussed in the power budget analysis.

To summarize the performance of the MWIR double layer meanderline retarder, it shows excellent performance at normal incidence. From Figure 62 it is observed that this design functioned very well, and the correlation between the modeled and measured data is very good at normal incidence. The design phase delay shows an average value of 90° over the MWIR and the corresponding measured data shows a very flat spectral phase response that keeps a phase delay within 10° of the design value. The corresponding state of the transmitted polarization is very nearly circularly polarized for the entire band. The measured axial ratio remains less than 1.7 for the entire band at normal incidence. The spectral region with the lowest axial ratio is measured to be in the spectral vicinity of a wavelength of 3.7 μm, though the spectral range from 3.35 μm to 4.45 μm has an axial ratio less than 1.2. Such good performance was expected due to the low permittivity of the fused silica substrate and the low, and nearly matching, permittivity of the BCB standoff layer. The non-normal angles of incidence along both planes showed good stability of the axial ratio up to 40° for wavelengths longer than 3.5 μm.

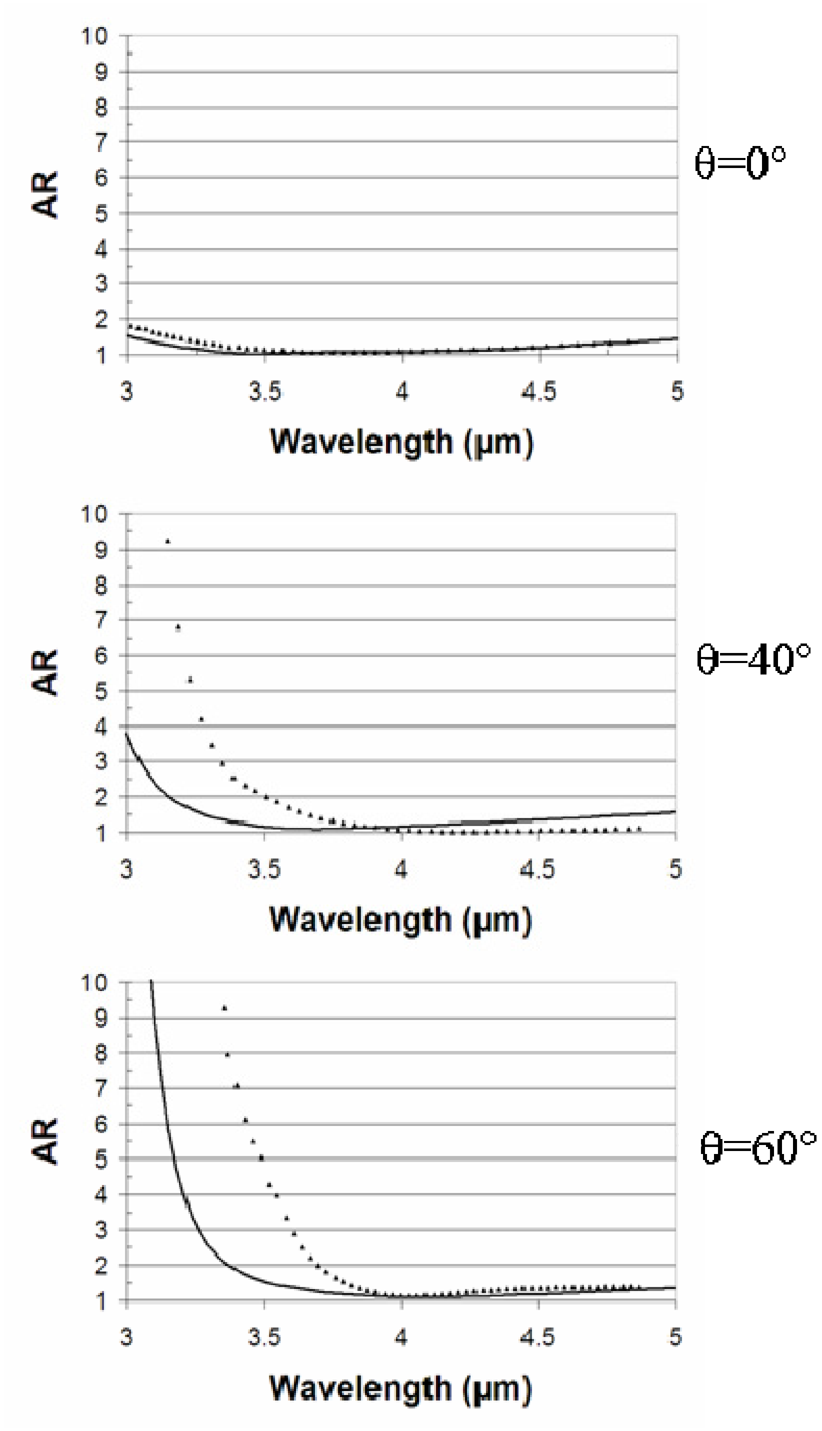

Figure 63 Measured and modeled axial ratios for the angles of incidence of 0°, 40°, and 60° along the plane of incidence α=0°. The solid lines are modeled results and the black triangles are measured results.

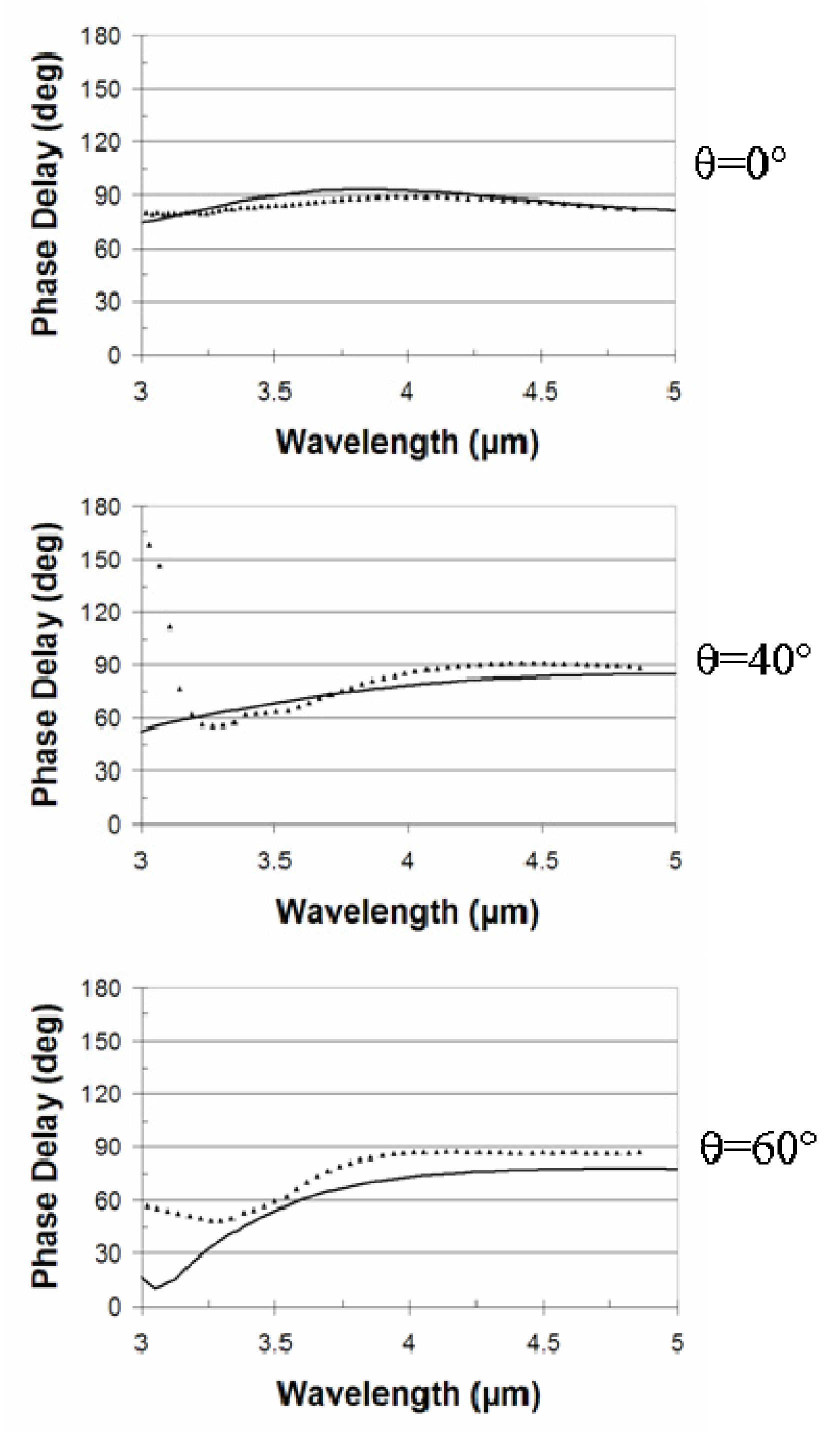

Figure 64 Measured and modeled phase delays for the angles of incidence of 0°, 40°, and 60° along the plane of incidence α=0°. The solid lines are modeled results and the black triangles are measured results.

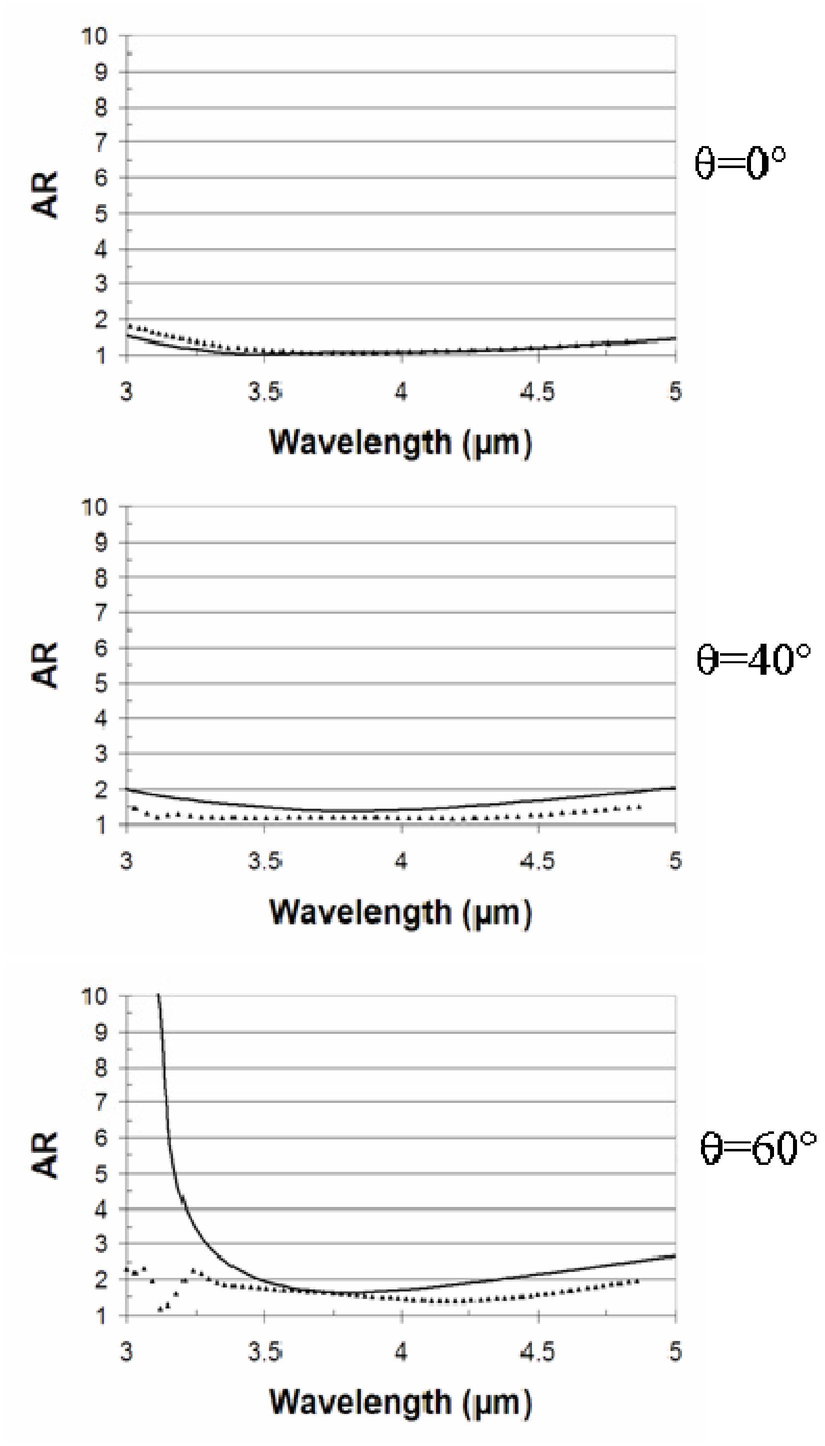

Figure 65 Measured and modeled axial ratios for the angles of incidence of 0°, 40°, and 60° along the plane of incidence α=90°. The solid lines are modeled results and the black triangles are measured results.

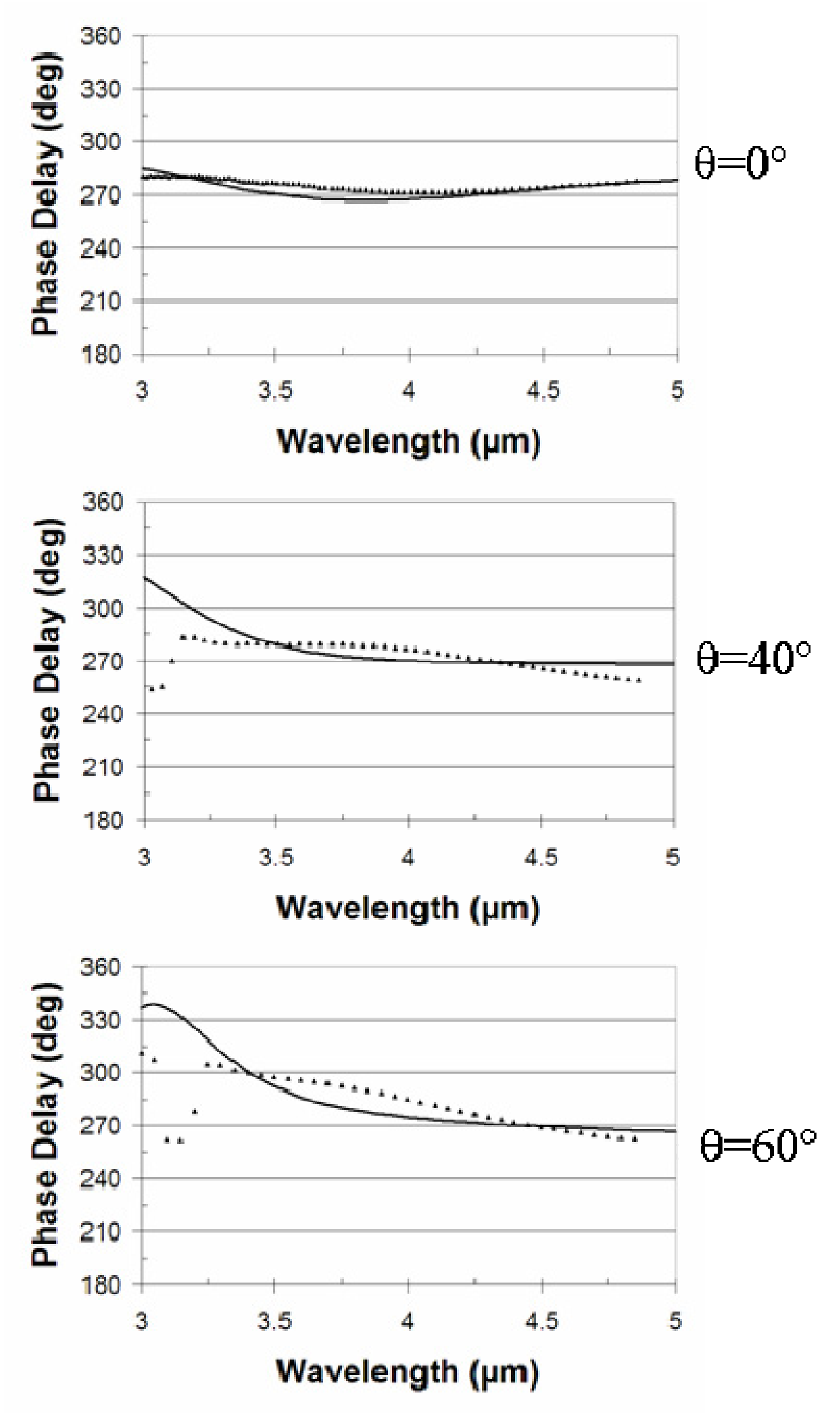

Figure 66 Measured and modeled phase delays for the angles of incidence of 0°, 40°, and 60° along the plane of incidence α=90°. The solid lines are modeled results and the black triangles are measured results.

5.3 LWIR Meanderline Operating in Reflection

The approach used to describe the functionality of the meanderline retarders uses an impedance mismatching condition as the source for the phase retardance. However, all that has been discussed is the use of the structures in transmission mode, however it is entirely conceivable that the reflection polarimetric properties can be modified as well. In this section, the feasibility of using a meanderline retarder in reflection mode will be investigated.

To begin the characterization of the reflective properties of the meanderline structure, the reflection properties of design #2 were characterized. The structure under test was the single layer quarter-wave retarder fabricated on the silicon substrate. This structure was chosen because of the silicon substrate. The silicon will aid in giving the highest reflection from the structure since the dielectric reflections are so high to begin with. Using the Smith chart, an expectation of the phase delay and magnitude of the reflection coefficient can be approximated for an ideal lossless meanderline retarder.

To determine the reflected properties of the single-layer meanderline, a circle was traced on the admittance circle that corresponds to the mismatch between silicon and air. This curve is depicted in Figure 67, along with the transmission and reflection vectors. After the circle is drawn, the transmission line is drawn at an angle of 45° with respect to the horizontal. The intersection of the 45° transmission line and the circle of admittance is the location of the impedance mismatch of the meanderline and air/silicon structure. The mismatch is represented by:

$$z_L = \frac{1}{y_L} = \frac{1}{\frac{1}{n_{Si}} - i\frac{1}{\chi_m}}$$ Equation 51

When this line is traced, it is determined that if the transmission coefficient has a phase angle corresponding to 45°, the reflected field will have a power reflection magnitude of 64% and a reflection phase angle of 164° and $\theta_r = 16°$ as shown in Figure 67.

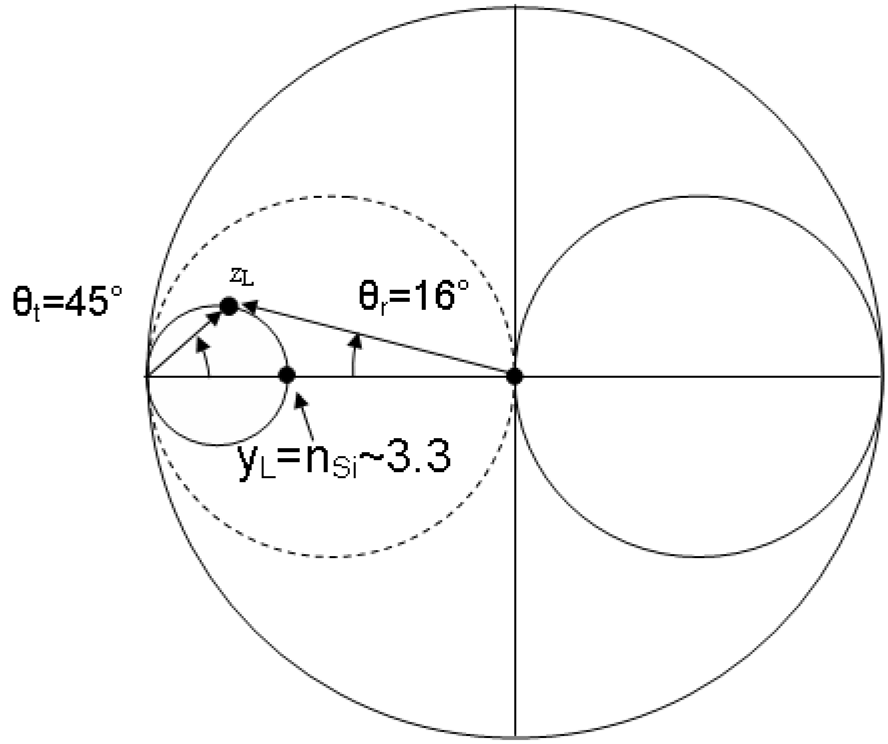

Figure 67 Smith chart representation for describing the reflected field of a single layer ideal meanderline on a silicon substrate

The expected phase delay in reflection for an ideal single layer meanderline retarder designed to transmit circular polarized radiation is 32° on a silicon substrate. The ideal power reflection amplitude would be 64%, assuming no backside dielectric reflection. When the backside dielectric reflection (29%) is accounted for, the total ideal transmission is 25.6%. Therefore the ideal reflected power should be 74.4%.

To measure the performance of the single-layer quarter-wave meanderline retarder, the IR-VASE was used in reflection mode. However, because of the design of the instrument, the smallest angle that can be measured in reflection is 26° from normal. This was not expected to affect the measurement too strongly since this meanderline design showed excellent transmissive angular stability in earlier measurements and no diffraction effects. The phase delay, for both orientations of the plane of incidence, of the meanderline is shown in Figure 68.

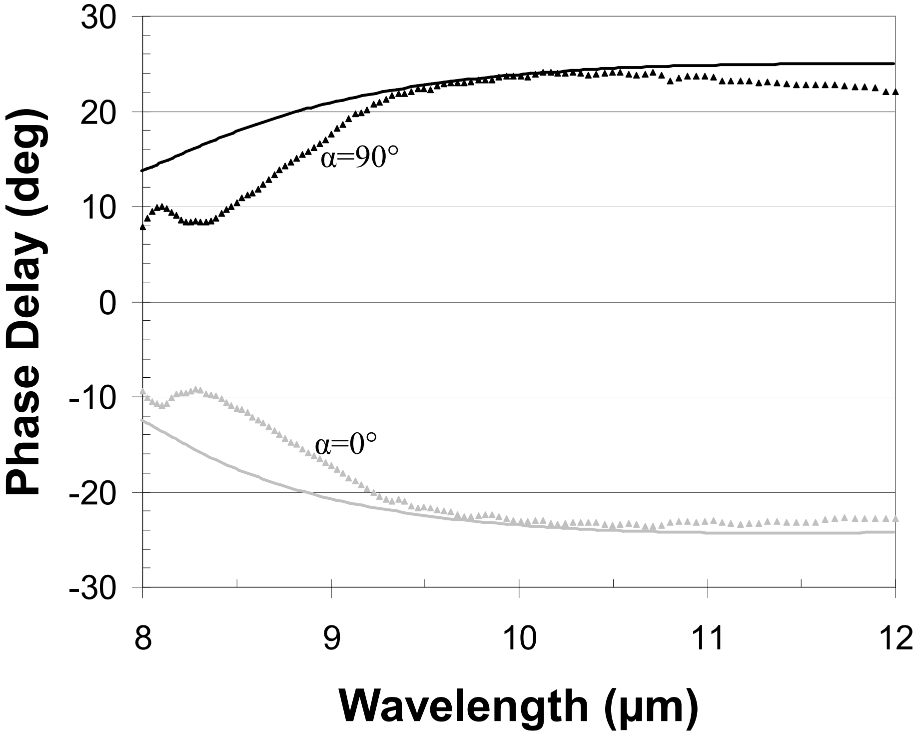

Figure 68 Measured (triangles) and modeled (solid) data for reflection of the single layer meanderline retarder for both α = 90° and 0°.

The measured phase delay at 10 μm is 24°, which is reasonably close to the expected 32° as determined from the Smith chart. The integrated power reflection was measured to be 74.5%. Therefore the total power budget analysis including the transmission measurements include an average transmission of 15%, an average reflection of 74.5%, and an average ohmic loss of 10.5%

The performance of the single-layer meanderline retarder operating in reflection showed good correlation to the expected results using the Smith chart and also with the modeled data in PMM. The potential for using the meanderlines as quarter-wave retarders in reflection mode show good feasibility if two reflections can be utilized. The maximum limit of the angle of the reflection coefficients is seen on the Smith chart to be the impedance mismatch between the substrate and air. The higher the substrate refractive index, the smaller the angle of the reflection coefficients will be for a given angle of transmission. However, it is also seen that the maximum value for the reflection angle is limited by the size of the circle of admittance. The maximum angle for the reflection coefficient as a function of the index of the substrate can be determined using the geometry of the Smith chart shown in Figure 69.

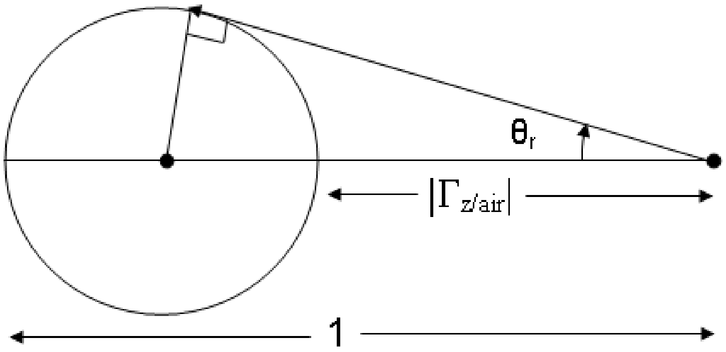

Figure 69 Geometry of the left region of the Smith chart, shown in Figure 67, used to determine the maximum angle of the reflection coefficient as a function of the substrate refractive index

Using Equation 17 to determine $|\Gamma_{z/air}|$, the magnitude of the reflection coefficient due to the impedance mismatch of the substrate and air, the relation for the maximum reflection angle and substrate index can be determined. The relation is given in Equation 52.

$$\theta_r = \arcsin\left[\frac{1-|\Gamma_{z/air}|}{1+|\Gamma_{z/air}|}\right] \qquad \text{Equation 52}$$

Using Equation 52, the maximum angle for the reflection coefficient on silicon is 17.9°, which is very close to the angle that was determined from the Smith chart. The maximum impedance that can be used to have a refection angle of 45°, for a total phase delay of 90°, can be determined and corresponds to an index of refraction of n_{max}=1.414 for the substrate. However, at this refractive index and reflection angle, the power reflection coefficient is only 19%.

The ideal reflecting meanderline device operating as two separate polarizing reflectors would maximize the power reflected and phase delay. Each reflector will induce a phase delay of 45°, corresponding to a field angle of 22.5°. From the Smith chart, the substrate for this ideal reflecting retarder will have to have a refractive index of n=2.47, and the power reflected from a single surface will be 47.3%. After reflecting from the second surface, the total phase delay will be 90° and the total power reflected will be 22.3%.

From the above two discussions, it can be determined that a reflecting meanderline polarizer will offer good polarization performance at the expense of having a low total power reflection for a quarter-wave retarder.

CHAPTER VI ANOTHER APPLICATION OF MEANDERLINE RETARDERS

The applications of the meanderline retarders can extend to any application where a crystal retarder would be required. Specifically ellipsometric measurements could be extended more easily to new bands of interest in the THz and millimeter waver regime with known retarders. In this way material optical properties can be measured at these frequencies to improve the material databases. The large field of view of these meanderline retarders offer the feasibility of adding a retarder within an imaging optical train with good performance over the imaging field, especially for astronomical polarimetry. These retarders can even be used as a replacement for crystal retarders since their fabrication can be commercialized and the eventual cost can be comparable or even less than a traditional crystal retarder.

Another application for the meanderline retarders is for the tagging of objects in the band of interest. The contrast for the tagging will be due to the polarization properties of the received radiation, and in the case of the meanderline retarders the polarization response is fairly constant for broad bands on interest. One area can be designated as left circularly polarized while another region can be designated as right circularly polarized, and using another filtering meanderline retarder at the receiver they can be easily distinguished with a very high contrast. These regions will also be indistinguishable from each other with a camera alone as circularly polarized light appears identical to unpolarized light to a camera with no polarization filter. This indistinguishability also exists if a linear polarizer is used in front of a receiving camera. This is because circularly polarized radiation is composed of equal magnitudes of vertical and horizontal polarization states.

6.1 Broadband Polarization Properties/Tagging

Another convenient aspect of the meanderline retarders is the fact that by merely rotating the retarders by 90° the handedness of the circular polarization can be switched. This could be potentially useful in a broadband IR optical modulator or for tagging purposes. The exceptional nature of the meanderline retarder doing this is that the meanderline retarder has a very broad bandwidth of operation with good angle of incidence stability. The meanderline can also be fabricated on large areas which crystal retarders can not.

A demonstration of the broadbanded nature of the retarding effect was set up to visualize the information and characterizations presented. In this demonstration a high emissivity source was warmed to approximately 40°C. Following the source a linear polarizer was set with a patterned fused silica MWIR meanderline double layer retarder. The lithographic nature for the fabrication allows for any geometry to be composed of meanderlines, rotated in any direction. The pattern that was fabricated onto the fused silica is depicted in Figure 70. The total dimension of the pattern is 15 mm x 15mm.

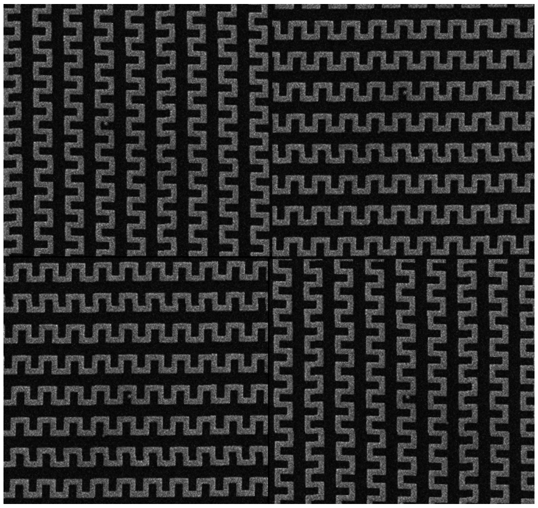

Figure 70 Schematic image of the pattern fabricated to demonstrate the broadbanded polarization properties

Following the patterned meanderline structure, a filtering meanderline structure was placed in front of a linear polarizer oriented at 45° with respect to the meanderline axis. The radiation was imaged in a MWIR FLIR camera. A picture of the setup is shown in Figure 71. The goal was for this experiment was to have the one orientation of the patterned meanderline structure emit left circularly polarized radiation while the other orientation emitted right circular polarized radiation. As each of these polarizations interact with the meanderline filter, that has only one orientation, the light that is transmitted will be linear polarized at either +45° or -45° depending upon the polarization state of the incident radiation. A linear polarizer was situated after the second meanderline structure in an orientation of +45°, or parallel with the first linear polarizer in the system. In this setup one circular polarization state will be fully passed into the MWIR camera while the other state will be fully attenuated by the second linear polarizer. The contrast between the two regions will be a demonstration of the broadband functionality of the meanderline structures, and the images of the patterned structure are shown in Figure 72. Figure 72A) shows the patterned region as viewed through the MWIR camera alone, Figure 72 B) shows the patterned region as viewed with a linear polarizer oriented parallel to the first linear polarizer at +45°. Figure 72 C) shows the patterned region as viewed with the unpatterned meanderline structure placed in front of the linear polarizer. The demonstration in Figure 72 B) shows that the radiation is nicely circularly polarized as the linear polarizer does not distinguish the regions in the image. The final image in Figure 72 C) shows excellent contrast between the two circular polarization states which represents excellent broadband performance.

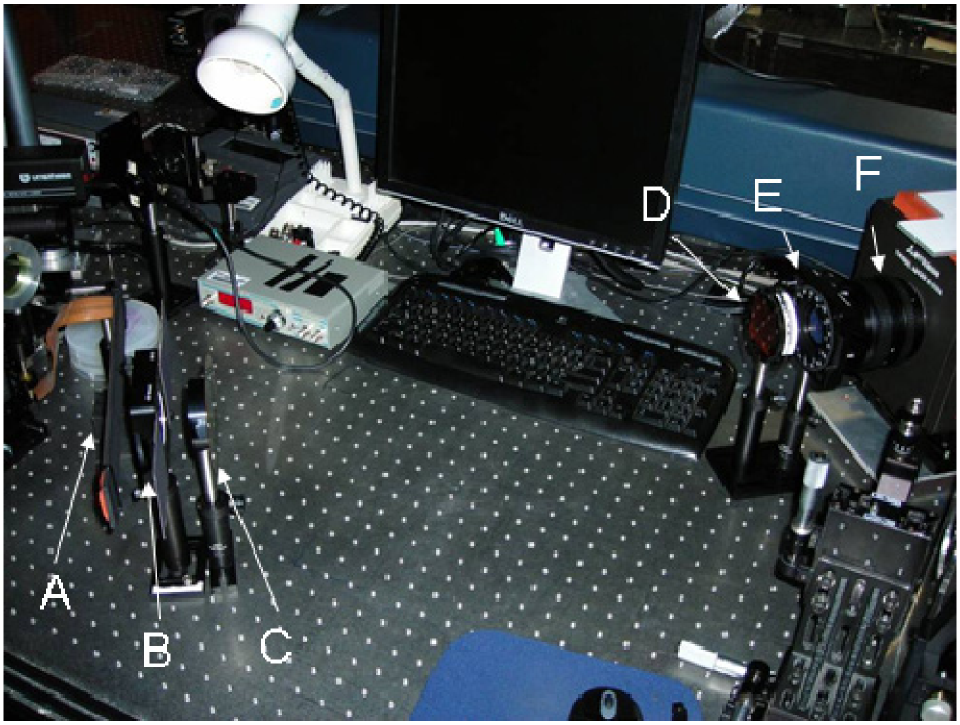

Figure 71 Picture of the lab setup used to demonstrate the broadbanded meanderline retader properties. The setup consists of (A) high emissivity heat source, (B) Linear Polarizer, (C) patterned demonstration meanderline retarder, (D) meanderline filter, (E) linear Polarizer set to 45° with respect to meander axis, and (F) MWIR infrared camera.

From Figure 72 it can be observed that by rotating the meanderline structure by 90° and including a meanderline filter before the camera that high visibility can be observed between the two circular polarization states. Figure 72 C) demonstrates this visibility and the ease with which it can be patterned. Because of the lithographic processing, all of the patterns are done via a computer program. This allows for the patterning of alphanumeric symbols that are only observable using a meanderline filter and linear polarizer in front of the camera. No other observers could interpret the information that is encoded into the polarization state of the tag.

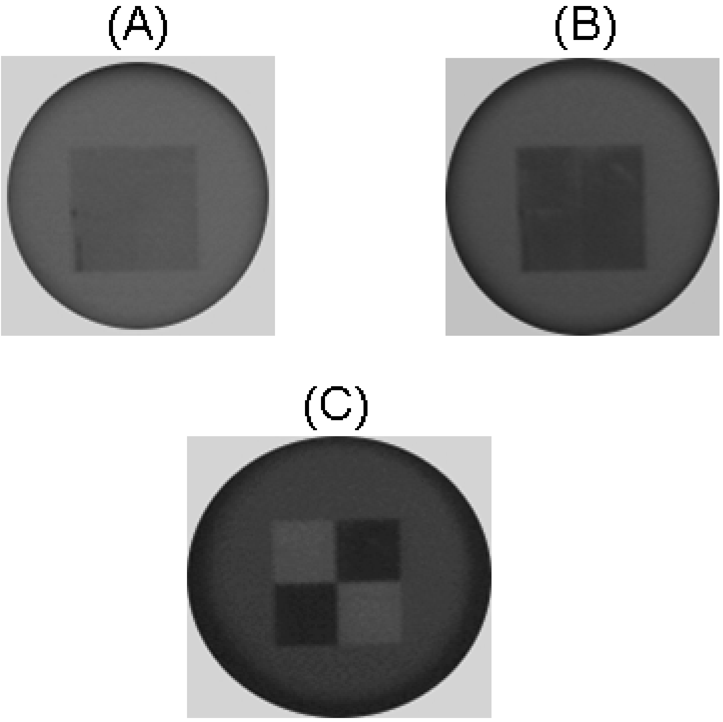

Figure 72 Images taken of the patterned structure A) through the MWIR camera alone, B) as viewed with a linear polarizer in front of the MWIR camera, and C) as viewed through the meanderline filter placed in front of the linear polarizer.

The contrast between the two polarization states depends upon the phase difference that is induced by the tag. For circular polarization the tag has been designed to induce a phase delay of 90°. When the radiation reaches the filter, the filters effect will depend upon the orientation of the tagging meanderline region with respect to the filter meanderline region. If the two meanderline axes are parallel, then the phase delay will be increased by another 90° to a total phase delay of 180°, or linear polarization oriented orthogonal to the initial linear polarization at the tag. If the two meanderline axes are perpendicular to one another, then the phase delay that was induced by the tag will be completely retracted by the filtering meanderline leaving a total phase delay of 0°, or linear polarization parallel to the input linear polarization of the tag. One advantage of this technique is that when the filter meanderline axis is perpendicular to the tag meanderline axis, the phase delay will always be zero. This implies that linear polarization will always be the output of a filter if the meanderline axes of the filter and tag are perpendicular. This effect is independent of the induced phase delay of the meanderline since any induced phase delay will always be retracted. When the meanderline axes of the tag and filter are parallel, the output of the filter will only be linearly polarized if the phase delay induced by the tag and filter is 90°, and the sum of the phase delays will cause an elliptical polarization state for phase delays larger or smaller. This elliptically polarized radiation will decrease the power that is passed by the linear polarizer and into the camera. Therefore the contrast between the bright and dark regions of a tag depends upon the phase delay induced.

The largest advantage of this technology is that since the polarization properties of the meanderline retarders are broadbanded, they are observed easily with cameras with large bandwidths. Also, these can be patterned over large areas of interest.

6.2 MWIR Circular Polarizer

The meanderline structure alone acts only as a phase retarder. To transmit circularly polarized radiation, linearly polarized light must be incident onto the meanderline retarder oriented at an angle of 45° to the meanderline axis. Therefore a linear polarizer is necessary. An advantage in the use of meanderline retarders is that their layered structure allows for an easy inclusion of a wire grid polarizer into the stack. This wire grid polarizer will serve to linearly polarize the incident radiation and orient the polarization to 45° with respect to the meanderline axis. The total device including the wire grid polarizer and meanderline stack would constitute a compact broadband circular polarizer.

The efforts to fabricate a MWIR circular polarizer began with a modeling study to determine a good design for the wire grid linear polarizer. Ansoft's HFSS electromagnetic modeling package was used for the study rather than PMM. The use of HFSS was due to the ability for HFSS to mesh the total three-dimensional wire grid structure and more closely predict the performance in the MWIR. The wire grid design was determined using a line width, *w*, and periodicity definition, *dx*. A schematic of the design parameters is depicted in Figure 73.

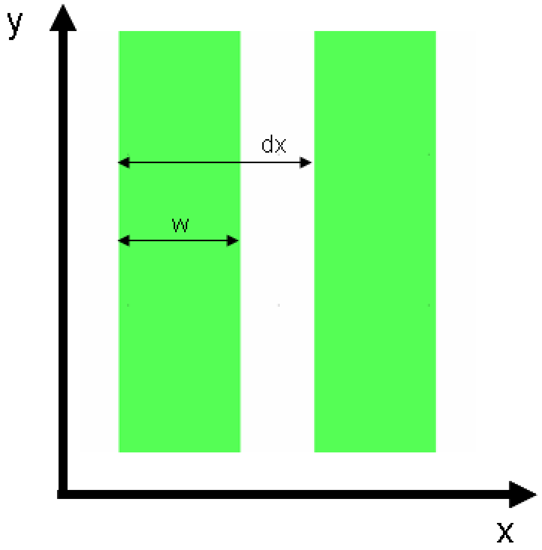

Figure 73 Schematic of the geometric variables and coordinate system used to model the performance of a wire grid linear polarizer to be fabricated for the MWIR circular polarizer.

The initial efforts in the design began with the general premise that the periody be less than a quarter-wavelength (effective) and the width to be much less than the wavelength. Since the design was for the MWIR, the shortest wavelength was used as the constraining value. With this, the initial design was also to be fabricated of aluminum since in has been described as having the highest conductivity in the IR as opposed to other popular metals including gold. The thickness of the aluminum was set to 75 nm which corresponded to over seven skin depths as described in [23]. The dimensions of the fabricated wire grid polarizer were: w = 0.3 µm and dx = 0.6 µm. The modeled and measured results for the wire grid polarizer are shown in Figure 74. The wire grid polarizer was modeled using the measured refractive index, n, for fused silica. However, to reduce the modeling time, the fused silica was modeled as a lossless substrate and the transmission results were multiplied by the measured transmission of the fused silica wafer so that the loss terms could be accounted for in the post processing. The modeled extinction ratio for this design at 3.5 µm was 26 and the measured extinction ratio was 15. This extinction ratio is not ideal, but it is sufficient to demonstrate the proof-of-concept for an integrated broadband MWIR circular polarizer.

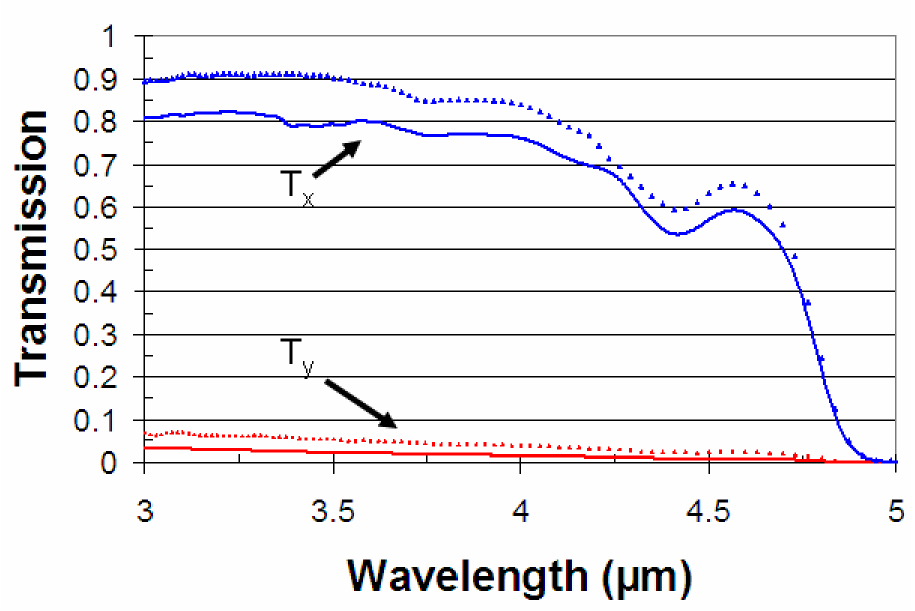

Figure 74 Modeled and measured transmission coefficients for the fabricated wire grid polarizer for the field component along the wire, T_y, and perpendicular to the wire, T_x.

To fabricate this structure, it was important that the wire grid polarizer did not experience any electromagnetic coupling to the meanderline structure. To ensure this, the wire grid polarizer was fabricated on the opposite side of the wafer from the meanderline retarders, and an image of the wire grid polarizer is seen in Figure 76. This placed the wire grid polarizer approximately 500 µm from the retarding meanderline elements. A schematic of the design is shown in Figure 75. The concept seems simple enough, but the fabrication is challenging since the meanderline structures have to be protected from scratches and damage as the fabrication proceeded on the bottom of the wafer.

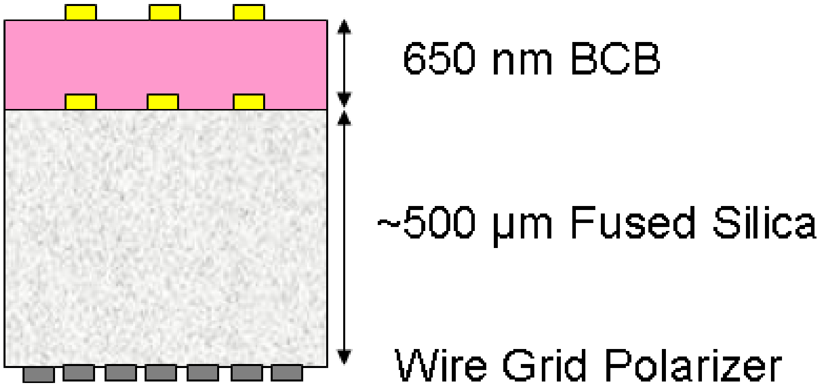

Figure 75 Cross-section of the design for the MWIR circular polarizer. This structure integrates the wire grid linear polarizer with the double layer meanderline for a compact circular polarizer.

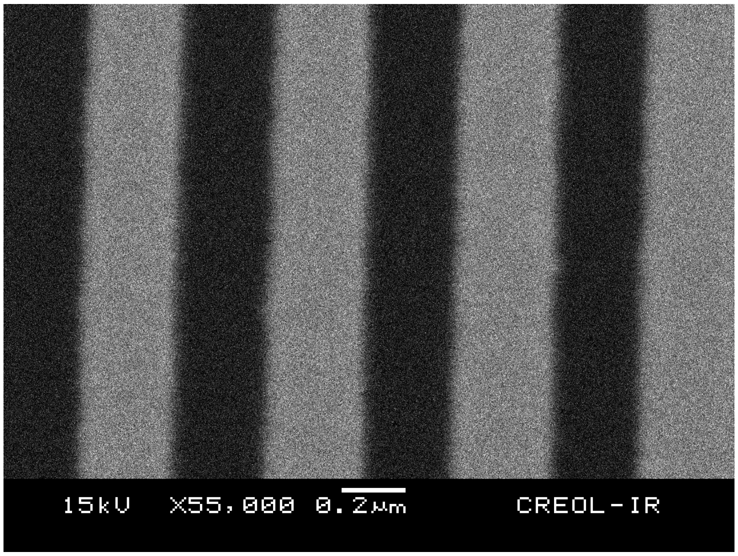

Figure 76 SEM image of the fabricated wire grid polarizer. Note this pattern used Au rather than Al for ideal imaging conditions

With the inclusion of the wire grid polarizer with the meanderline, the tagging concept can be extended. Now a film can be manufactured with the linear polarizer and meanderline retarder to act as a circular polarizer. This integrated circular polarizer can be affixed to a surface, and the radiation that is thermally radiated from the surface is converted to the circular polarization for decoding at an observing camera with a meanderline filter.

CHAPTER VII
CONCLUSIONS AND FUTURE WORK

Prior to the work of this dissertation, meanderline retarders had not been investigated for their feasibility of operation in the IR spectrum. Traditional methods of retarding the radiation in these bands have been limited to birefringent crystal retarders and narrow band reflection retarders. Meanderline retarders were modeled, fabricated, and characterized for operation in both the MWIR (3 - 5 µm) and LWIR (8 – 12 µm). A geometric tolerance study was modeled to determine how variations in the meanderline geometric parameters would affect the polarimetric performance of the structures. Using these trends, designs can be optimized. The characterizations of these fabricated structures showed good agreement to the expected modeled results, and measures were taken to optimize their performance. The addition of multiple layers of meanderlines and lower permittivity substrates were used to increase the transmission throughput of the structures via impedance matching while retaining the desired retarding functionality. Along with the transmission properties, the angle of incidence performance was modeled and measured. These measurements showed excellent performance of the meanderline retarders over angles of incidence up to the maximum angle measured of 60°. The final structure fabricated incorporated a double layer quarter-wave meanderline fabricated onto a cascaded wiregrid polarizer to act as an integrated circular polarizer over the MWIR.

7.1 Summary and Future Work

For the LWIR, the first structure fabricated was a single-layer meanderline on a silicon substrate. This structure was characterized in transmission and reflection. The transmission performance of this structure showed a measured normal incidence axial ratio that remained less than 2 for normal incidence for the entrire LWIR with a minimum AR of 1.13 at 10.25 μm. The integrated transmission was measured to be 15%. The angular performance of the meanderline showed a near constant phase delay with angle and shift in the minimum AR that is attributed to the projection effects of the transmission coefficient of the incident radiation that is oriented parallel to the plane of incidence. There were also no observed diffraction effects. The reflection polarization parameters correlated well to both the numerically modeled results and the results determined graphically from the Smith chart. In reflection, the phase delay measured flattened to 24° after a wavelength of 9 μm. The integrated power reflected was 74% which was used to calculate the 28% loss of power due to ohmic losses in the metal. Multiple layer meanderlines were fabricated and measured using a silicon and BCB standoff layer between the meanderline layers. They did not perform as well as the single-layer meanderline with respect to the magnitude of the phase delay; however it was observed that the phase delay was spectrally flatter than for the single layer meanderline. Another double-layered meanderline retarder was fabricated onto a BaF_2 substrate to increase the overall transmission of the structure. The measured integrated transmission was 60%. The integrated transmission for this structure showed much improvement over the use of silicon as a substrate, and was limited by the use of the lossy BCB as the standoff layer. The AR of the BaF_2 structure remained less than 2 for the entire band, and this performance can be improved by increasing the phase delay from the measured average of 70° to 90°. A variation in the geometry to a zig-zag pattern was also investigated. This structure had a measured AR that was less than 2 for wavelengths longer than 9 μm and an integrated transmission of 23% which is greater than the 15% measured for the single layer meanderline on silicon. This difference in transmission performance is because the single layered meanderline had more metal as it had the same line width as the zig-zag, but was packed in much more closely since its period was much smaller. The zig-zag structure also had a smaller impedance mismatch, as observed by the lower phase delay, as compared to the single layer meanderline which will cause less reflection. The reflection characterization of the single layer quarter-wave meanderline on silicon showed that the structure also changes the polarimetric properties upon reflection. The reflection characterization described the limitations in using the meanderline structure as a reflective quarter-wave retarder.

For the MWIR, a double layered meanderline retarder was fabricated and tested. The low permittivity substrate, fused silica, posed many fabrication issues that had to be overcome as compared to the use of silicon. The standoff layer used was BCB which demonstrates very low attenuation in this band. The AR of this structure was measured to be 1.8 at 3 μm and 1.3 at a wavelength of 4.6 μm. The ideal aspect was that the AR was less than 1.2 from 3.7 μm to 4.5 μm. This steady AR was because of the flatness of the phase delay which was measured to be between 90° and 100° for the entire band. The integrated transmission was measured to be 53% which was primarily limited by the integrated substrate transmission of 78%.

Conclusions that can be drawn include that the design of a meanderline retarder will depend upon the application for which it is needed. If broadband performance is desired with a high transmission, a multiple layered meanderline is desired. The multiple layers will allow for the impedance required for the phase delay to be distributed over more than one layer, and each layer will induce a fraction of the necessary phase delay. However, it was determined that the maximum number of layers to be used in the IR was two. The ohmic losses in the metal of a third layer counter the gain in transmission from the impedance matching. As the phase delay decreases, the period of the structures will most likely be increased which will cause the onset of diffractive effects as the angle of incidence increases as described in Section 1.4.3. Therefore, good polarimetric performance and high transmission can be at the expense of a higher sensitivity to large angles of incidence as was measured for the MWIR double layer design on fused silica. To keep this effect to a minimum the phase delay can be controlled by the keeping the periodicity as small as possible while reducing the width of the meanderline, *w*. If a structure is required to have excellent angle of incidence stability, it was found that a single layer meanderline will be ideal since it will keep a constant phase delay for large angles of incidence. The limitation of a single layer design is that it will have a narrower band of ideal polarimetric performance and the transmission will be reduced due to the high impedance mismatch necessary for the phase delay. The transmission can be increased by using a lower permittivity substrate, but it will be found that the meanderline structure will have to have a higher impedance to induce the necessary phase delay and the two will compete to keep the ideal transmission to a maximum of 50% in free-space.

The comparison of the two meanderline structures that operated as quarter-wave retarders, the single layer meanderline on silicon in the LWIR and the double layer meanderline on fused silica in the MWIR, showed that the measured axial ratio and phase delay of the structures could compare to the current crystal retarders. In particular, the bandwidth of both structures performed similarly to single-order crystal retarders in terms of spectral deviation of the axial ratio for normal incidence. Each structure also demonstrated less sensitivity to the angle of incidence as compared to the single-order crystal retarder. The comparison of the transmissions of the meanderline structures and crystal retarders was made. Crystal retarders generally have an antireflection coating which gives them a transmission upwards of 98% at the design wavelength. The spectral transmission will be limited by the bandwidth of the anti-reflection coating. The double layer meanderline in the MWIR had a measured transmission of 53%. The double layer meanderline retarder in the LWIR had an average transmission of 60%; however its average induced phase delay was just 65°. The mechanisms of loss were identified for each structure and the primary sources of loss was the ohmic losses and material attenuation in both the substrates and standoff layers.

The final MWIR meanderline retarder was modified to include a wire grid linear polarizer so that it would act as an integrated circular polarizer for the MWIR. A characterization including modeled and measured results for the wire grid polarizer was also done that demonstrated a measured extinction ratio of 15 at 3.5 μm.

Following the fabrication and characterization, a patterned MWIR meanderline was placed in front of an integrated MWIR camera to observe the broadband performance of the structure and show the possible application as a high visibility tagging technology.

A path for future work will include finding a modeling method that can incorporate the measured complex conductivities of the metals used into the impedance calculations of the meanderline structure. With this accomplishment, a sample structure will not have to be fabricated and measured to determine an empirical fit parameter, the equivalent sheet resistance, before other structures can be reliably modeled. Numerical variations to the general geometry would also then become feasible and an investigation can be done to find an ideal geometry that may have better overall performance than the meanderline geometry. Future work can also lie in the further optimization of the LWIR meanderline on BaF_2 and an inclusion of a MWIR design onto the BaF_2.

Further study can be done to optimize a design to be used as a tag for standoff observation using a meanderline filter. Such advancements to improve the application of these structures for tagging will include an investigation to fabricate the structures onto a flexible, contour fitting substrate.

7.2 NIR and Visible Meanderline Feasibility

The feasibility of using the meanderline structures in the near infrared (NIR) and visible is limited by a combination of issues both in fabrication and in the modeling. However, these obstacles can be overcome and the physics will not fundamentally change.

The issue of the modeling is primarily limited to the material properties of both the metals used and the dielectric substrates. The metals in these higher frequencies will have lower conductivities, and the metal choice will become very important. Another aspect of the metals that may become an issue is the roughness of the surface of the meanderline structures after the metal evaporation. If the surface of a meanderline is observed using atomic force microscopy as shown in Figure 77, it can be seen that the surface of the meanderline is not perfectly flat. There is a roughness that is due to the method and conditions of evaporation and this roughness may lead to a reduction in conductivity due to the surface scattering of the induced currents. The dielectric substrates in the NIR and visible become easier to work with as fused silica becomes very transparent and low permittivity. The low permittivity will lead to effective wavelengths that are closer to the free-space wavelengths which will make the structures as ideally large as possible. This will be beneficial in the fabrication.

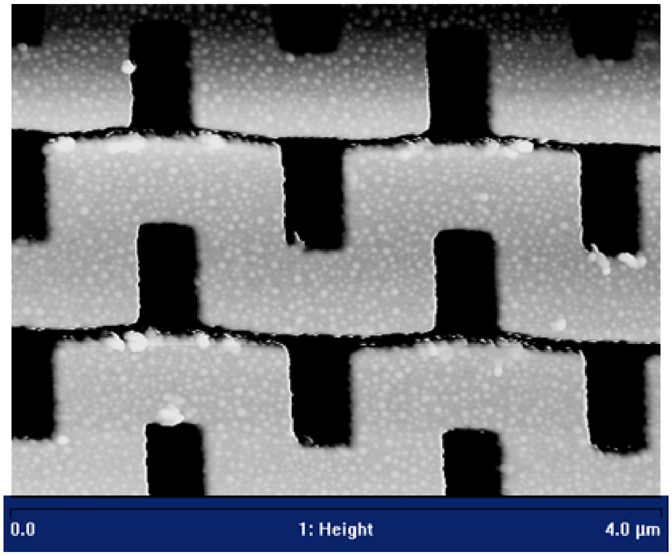

Figure 77 Atomic Force Microscope image of the single layer quarter-wave meanderline on silicon. AFM shows that there exist obvious roughness on the surface of the meanderline structures that may contribute to reducing the conductivity in the NIR and visible wavelengths due to scattering.

The limit of the resolution in our fabrication facility is limited to a line width of about 50 nm for reliable liftoff. The line width of the MWIR structure was 225 nm, so there is optimism that a structure can successfully be fabricated for the NIR. The visible band is possible, but with current technology could be very challenging as the line widths and structure geometry become smaller and smaller.

APPENDIX: FABRICATION PROCESSES

A.1 Single-Layer Meanderline Quarter-Wave Retarder for LWIR

The fabrication of the single layer meanderline quarter-wave retarder involved a single layer lithographic step and is the most easy to fabricate. The steps for fabrication will laid out below in a recipe format with enough detail so that anyone with comparable facilities will be able to reproduce the structures.

1. Make a *.gds file with the meanderline pattern and at the desired size for the array. For this pattern, the design parameters for the meanderline are: w=0.5 µm, pw=1.0 µm, ph=0.7 µm, and dx=1.45 µm. The width is intentionally undersized from the goal width in the modeling to accommodate for expected overdevelopment.
2. Once the pattern file is constructed, the file must be fractured into polygons that the JEOL EBPG e-beam writer will recognize. This is done using Synopsis CATS program.
3. Once fractured the file must be transferred to the JEOL EBPG computer via FTP. Note the pixel size after fracturing for use to determine approximate write time.
4. For the meanderline geometry, write time can be approximated by dividing the pixel size by the write frequency (determined from the write parameters and shown below) and then multiplying the time by a factor of 3 to accommodate the settling time for the beam over the pattern. The formula for the write frequency is shown below:

$$f[MHz] = \frac{0.1 \cdot I_{beam}[nA]}{dose\left[{}^{\mu C}\!/_{cm^2}\right] \cdot \left(stepsize[\mu m]\right)^2}$$

I_{beam} is the current setting of the beam (for this pattern, the beam current was set to 25 nA to allow for a ~25 nm beam spot size.) The dose for this write was 120 μC/cm^2 as determined from a dose matrix. The stepsize for this write was determined by the resolution set during the fracturing of the file, and in this write the stepsize was equal to the beam spot size, 25 nm. The corresponding write frequency was 33 MHz.

5. Select a double-side polished high-resistivity (5-10kΩ-cm) silicon wafer
6. Clean the wafer by rinsing sequentially with Acetone, Methanol, and IPA
7. Bake the cleaned wafer at 180°C for 5 minutes to bake out any remaining water in the wafer and promote ZEP adhesion.
8. Spin on ZEP 520A – 7 ebeam resist with the following recipe: 500 rpm (10 seconds) and then 6000rpm (60 seconds). No adhesion promoter is necessary. It is very important that a whole wafer be used and that the wafer is well centered on the chuck to ensure that the wafer does not fly off during the high speed spin. This high speed spin is used to achieve a resist thickness of ~214 ± 1 nm as measured using ellipsometry and averaging over the wafer.
9. Bake the wafer at 180°C for 4:00 minutes to bake off the solvent (anisole) from the ZEP resist.
10. When finished baking, remove the wafer and blow off with N_2 to cool it before placing it into the holder.
11. Write the file onto the wafer with a dose of 120 μC/cm^2 and a beam current of 25 nA.
12. After writing the file, the wafer is to be developed using ZEP RD developer for a time of 90 seconds. The way these wafers were developed is a bit different than other processes

in the group. First, a 3” petrie dish is set down, then a small beaker is placed up-side-down into the dish. The wafer is placed onto the inverted beaker exposed side up. A dropper was filled with the ZEP RD developer, and development time started when the developer hits the resist. A picture of the setup is shown below.

13. Once developed, the wafer is barrel etched for 2:00 minutes at a power of 200 W RF and a O_2 pressure of ~380 mTorr. This is to descum any remaining resist in the region to be metallized.
14. Next is to deposit the Ti/Au layer with thicknesses of 10 nm/130 nm, respectively. This is done via ebeam evaporation.
15. Following the evaporation, the wafer is placed into a Methylene Chloride bath to soak for 5:00 minutes.
16. After soaking the wafer is then placed into a ultrasonic agitator for 10:00 minutes to finish the liftoff process.
17. The wafer should now be imaged in the microscope to ensure successful liftoff, if metal still appears to have not been lifted off, then another 10:00 minutes in an ultrasonic agitation should be done.

A.2 Double-Layer Meanderline Quarter-Wave Retarder for MWIR on Fused Silica

The double-layer meanderline retarder designed for the MWIR performed very well as outlined earlier in the dissertation. The primary difficulty with the fabrication of the MWIR meanderline retarder is the multiple layer aspect and the substrate. The substrate, Fused Silica, is transparent in the visible and therefore a poor surface for the Leica EBPG to measure the height of the surface from reflections at the surface. The laser used for height determination in the Leica has a wavelength of 633 nm. The other aspect of the substrate that is difficult is the fact that the fused silica is a very good electrical insulator which can cause significant charging at the surface while writing. To remedy both problems, a thin nickel layer is sputter deposited onto the substrate. It is imperative that the method of deposition be either thermal evaporation or sputtering. If this Ni layer is deposited via electron beam evaporation, the quantity of backscattered electrons is sufficient to completely expose ZEP520A-7 resist. Both of these challenges were dealt with and a successful structure was fabricated using BCB as a standoff layer. The process for fabricating the double layer MWIR meanderline quarter-wave retarder is outlined below.

1. Make a *.gds file with the meanderline pattern and at the desired size for the array. For this pattern, the design parameters for the meanderline are: w=0.18 µm, pw=0.4 µm, ph=0.5 µm, and dx=1.35 µm. The width is intentionally undersized from the goal width in the modeling to accommodate for expected overdevelopment.
2. Once the pattern file is constructed, the file must be fractured into polygons that the Leica EBPG e-beam writer will recognize. This is done using Synopsis CATS program.
3. Once fractured the file must be transferred to the Leica EBPG computer via FTP. Note the pixel size after fracturing for use to determine approximate write time.
4. For the meanderline geometry, write time can be approximated by dividing the pixel size by the write frequency (determined from the write parameters and shown below) and then multiplying the time by a factor of 3 to accommodate the settling time for the beam over the pattern. The formula for the write frequency is shown below:

$$f[MHz] = \frac{0.1 \cdot I_{beam}[nA]}{dose\left[\mu C/cm^2\right] \cdot \left(stepsize[\mu m]\right)^2}$$

I_{beam} is the current setting of the beam (for this pattern, the beam current was set to 25 nA to allow for a ~25 nm beam spot size.) The dose for this write was 100 μC/cm^2 as determined from a dose matrix. The stepsize for this write was determined by the resolution set during the fracturing of the file, and in this write the stepsize was equal to the beam spot size, 25 nm. The corresponding write frequency was 40 MHz.

5. Select a double side polished fused silica wafer
6. Clean the wafer by rinsing sequentially with Acetone, Methanol, and IPA
7. Bake the cleaned wafer at 180°C for 5 minutes to bake out any remaining water in the wafer and promote ZEP adhesion.
8. Spin on ZEP 520A – 7 ebeam resist with the following recipe: 500rpm (10 seconds) and then 3000rpm (80 seconds). No adhesion promoter is necessary. This spin speed is used to achieve a resist thickness of ~285 ± 1 nm as measured using ellipsometry and averaging over the wafer.
9. Bake the wafer at 180°C for 4:00 minutes to bake off the solvent (anisole) from the ZEP resist.
10. When finished baking, remove the wafer and blow off with N_2 to cool it before placing it into the holder.
11. Place the wafer resist-side up into the sputterer for the Ni deposition
12. Pump down sputterer to a pressure corresponding to the low 10^{-5} Torr
13. When pressure is achieved, close shutter and begin Ar flow to 22 sccm

14. Adjust chamber pressure to 6.5 mTorr with the Ar flowing
15. Turn on cooling water, set DC power supply to 2kW, start up DC power supply
16. Set the turn table speed to '0' and once the DC power supply is ready, begin table rotation. Wafer should spin for 50 seconds, which corresponds to two full passes beneath the Ni target upon starting the time with the wafer positioned 180° from Ni target. Approximately 40 nm of Ni should be deposited.
17. After deposition, shut down power supply and vent
18. Remove wafer
19. Write the file onto the wafer. If this is the second layer write, it will be necessary to align the second layer onto the bottom layer. To do this, use the Leica microscope and first find the region to be written (to find this region image in the lowest magnification and look for the edge shadows since one cannot image through the Ni layer. The edges of the first layer will look slightly shadowed) It is very important that the rotation be aligned as best as possible, there is flexibility in the x-y register.
20. After writing the file, a large piece of cleanroom floor tape is used to evenly remove the Ni layer from the ZEP. The Ni adheres very poorly to the ZEP and the tape will not damage the ZEP in this process. The one precaution is to only use the tape once, if the tape comes into contact with the resist layer instead of the Ni layer, the adhesive will be left as a residue and the developer cannot develop through the adhesive residue. The wafer is to be developed using ZEP RD developer for a time of 45 seconds. The way these wafers were developed is a bit different than other processes in the group. First, a 3" petrie dish is set down, then a small beaker is placed up-side-down into the dish. The

wafer is placed onto the inverted beaker exposed side up. A dropper was filled with the ZEP RD developer, and development time started when the developer hits the resist. A picture of the setup is shown below.

21. Once developed, the wafer is barrel etched for 2:00 minutes at a power of 200W RF and a O_2 pressure of ~380 mTorr. This is to descum any remaining resist in the region to be metallized.
22. Next is to deposit the Ti/Au layer with thicknesses of 3 nm/60 nm, respectively. This is done via ebeam evaporation.
23. Following the evaporation, use scotch tape to remove the Au
24. Place the wafer into a Methylene Chloride bath to soak for 5:00 minutes.
25. After soaking the wafer is then placed into a ultrasonic agitator for 10:00 minutes to finish the liftoff process.
26. The wafer should now be imaged in the microscope to ensure successful liftoff, if metal still appears to have not been lifted off, then another 10:00 minutes in an ultrasonic agitation should be done.
27. With the first layer successfully fabricated, the standoff layer must now be deposited. The desired thickness of BCB is ~560 nm. To get this thickness, the factory BCB (CYCLOTENE 3022-35) is diluted using the solvent, Mesitylene to a ratio of 10::15, BCB::Mesitylene, by weight. At this thickness, the BCB is spun using a spin speed of 500 rpm (10 seconds) and 3000 rpm (60 seconds) to give a thickness of ~260 nm.
28. Spin on BCB adhesion promoter at a spin speed of 500 rpm (10 seconds) and 2000 rpm (20 seconds)

29. Following the adhesion promoter, spin on the 10::15: BCB::Mesitylene at a spin speed of 500 rpm (10 seconds) and 3000 rpm (80 seconds)
30. Bake the wafer on a hotplate at 120°C for 3:00 minutes to evaporate the solvent
31. Hard cure the BCB by baking on a hotplate at 250°C for 5:00 minutes
32. Following the hard cure, the next layer of BCB can be deposited using the same procedure outlined for the first layer with no intermixing between the two layers
33. Following the BCB layers, go to step 6 and repeat through step 22
34. Place the wafer into a Methylene Chloride bath to soak for 10:00 minutes. It is important not to use the tape for this layer for Au removal. The adherence of the BCB to the gold meanderlines on the first layer is not strong enough to survive the use of tape.
35. After soaking the wafer is then placed into an ultrasonic agitator for 10:00 minutes to finish the liftoff process.
36. The wafer should now be imaged in the microscope to ensure successful liftoff, if metal still appears to have not been lifted off, then another 10:00 minutes in an ultrasonic agitation should be done.
37. Structure is ready to characterize

REFERENCES

1. Young, L., L.A. Robinson, and C.A. Hacking, *Meander-Line Polarizer.* IEEE Transactions on Antennas and Propagation, 1973. **21**(3): p. 376-378.
2. Mazur, M. and W. Zieniutycz. *Multi-layer meander line polarizer for Ku band*. in *Microwaves, Radar and Wireless Communications. 2000. MIKON-2000. 13th International Conference on*. 2000.
3. Zurcher, J.F., *A meander-line polarizer covering the full E-band (60-90 GHz).* Microwave and Optical Technology Letters, 1998. **18**(5).
4. Munk, B., *Finite antenna arrays and FSS*. 2003, Hoboken, NJ: IEEE Press : Wiley-Interscience.
5. King, R.J., *Quarter-Wave Retardation Systems Based on Fresnel Rhomb Principle.* Journal of Scientific Instruments, 1966. **43**(9).
6. Goldstein, D., *Polarized Light*. 2nd ed. 2003, New York, NY: Marcel Dekker, Inc.
7. Hecht, E., *Optics*. 4th ed. 2002, Reading, Mass.: Addison-Wesley. vi, 698 p.
8. Born, M., E. Wolf, and A.B. Bhatia, *Principles of optics : electromagnetic theory of propagation, interference and diffraction of light*. 7th (expanded) ed. 1999, Cambridge [England] ; New York: Cambridge University Press.
9. G. R. Bird, M.P., *The wire grid as a near-infrared polarizer.* JOSA, 1960. **50**(9).
10. Meadowlark Optics, I. *Sources of error in retarders and waveplates*. 2005 [cited; http://www.meadowlarkoptics.com/].
11. G.W, H.P.D.a.D., *Stability of birefringent linear retarders (wavelplates).* Applied Optics, 1988. **27**.
12. Delihacioglu, K. and S. Uckun, *Power reflection and transmission coefficients for meander-line polarizers with a chiral slab.* Etri Journal, 2003. **25**(1): p. 41-48.
13. Goodman, J.W., *Statistical optics*. Wiley classics library ed. Wiley classics library. 2000, New York: Wiley.
14. Chu, R.S. and K.M. Lee, *Analytical Model of a Multilayered Meander-Line Polarizer Plate with Normal and Oblique Plane-Wave Incidence.* IEEE Transactions on Antennas and Propagation, 1987. **35**(6): p. 652-661.
15. Balanis, C.A., *Antenna theory : analysis and design*. 3rd ed. 2005, Hoboken, NJ: John Wiley.
16. Marino, R.A., *Accurate and efficient modeling of meander line polarizers.* Microwave Journal, 1998. **41**(11).
17. Pozar, D.M., *Microwave engineering*. 3rd ed. 2005, Hoboken, NJ: J. Wiley.
18. Wu, T.K., *Meander-Line Polarizer for Arbitrary Rotation of Linear-Polarization.* IEEE Microwave and Guided Wave Letters, 1994. **4**(6): p. 199-201.
19. Gonzalez, G., *Microwave transistor amplifiers : analysis and design*. 1984, Englewood Cliffs, N.J.: Prentice-Hall.
20. Munk, B., *Frequency selective surfaces : theory and design*. 2000, New York: John Wiley.
21. Smith, P.H., *Electronic applications of the Smith Chart; in waveguide, circuit, and component analysis*. 1969, New York,: McGraw-Hill. xxvii, 222.

22. Smith, P.H., *Electronic applications of the Smith Chart in waveguide, circuit, and component analysis*. 1995, Noble Pub. Corp.: Atlanta, Ga.
23. Ginn, J., et al., *Characterizing infrared frequency-selective surfaces on dispersive media.* Applied Computational Electromagnetics Society Journal, Mar 2007.
24. A.W. Rudge, K.M., A.D. Oliver, P. Knight, *The Handbook of Antenna Design*. IEEE Electromagnetic Waves Series. Vol. 2. 1986, London, UK.
25. Terret, C., J.R. Levrel, and K. Mahdjoubi, *Susceptance Computation of a Meander-Line Polarizer Layer.* Ieee Transactions on Antennas and Propagation, 1984. **32**(9): p. 1007-1011.
26. Lynch, J.J. and J.S. Colburn, *Modeling polarization mode coupling in frequency-selective surfaces.* Ieee Transactions on Microwave Theory and Techniques, 2004. **52**(4): p. 1328-1338.
27. Bhattacharyya, A.K. and T.J. Chwalek, *Analysis of multilayered meander line polarizer.* International Journal of Microwave and Millimeter-Wave Computer-Aided Engineering, 1997. **7**(6): p. 442-454.
28. Henderson, L.W., *Introduction to PMM, Version 4.0*. July 1993, The Ohio State University Electroscience Laboratory: Columbus, OH.
29. Wooten, F., *Optical properties of solids*. 1972, New York, London,: Academic Press. xii, 260 p.
30. Fox, M., *Optical properties of solids*. Oxford master series in condensed matter physics. 2001, Oxford ; New York: Oxford University Press.
31. Ohring, M., *The materials science of thin films*. 1992, Boston: Academic Press.
32. *Guide to the expression of uncertainty in measurement*. 2nd ed. International Organization for Standardization, 1995.
33. Tharp, J.S., et al., *Demonstration of a single-layer meanderline phase retarder at infrared.* Optics Letters, 2006. **31**(18): p. 2687-2689.
34. Palik, E., *Handbook of Optical Constants of Solids*. Vol. I. 1997, San Diego: Acedemic Press, 1997.
35. J. Ginn, D.S., J. Tharp, B. Lail, G. Boreman. *Distributed loading effect for infrared FSS.* in *IEEE Antennas and Propagation Society International Symposium*. 2007. Honolulu, HI.